Studying the Bosonic Phases in Granular Systems Undergoing the SIT

Yehudit (Judith) Fradel Stein
Department of Physics
Ph.D. Thesis

Submitted to the Senate of Bar-Ilan University

Ramat-Gan, Israel October, 2024

This work was carried out under the supervision of Prof. Aviad Frydman,
Department of Physics, Bar-Ilan University

Acknowledgments

This thesis was completed during the COVID-19 pandemic and times of war- circumstances that brought unexpected challenges to this demanding journey. As I conclude this chapter and look ahead, I am deeply aware of the privilege to continue and progress while the lives of others are held in suspension. My thoughts are with the hostages still held in captivity, hoping for their safe return home soon, and with our brave soldiers (including my lion), whose sacrifices make it possible for the rest of us to carry on.

Completing this thesis marks the conclusion of my academic journey and reflects a period of significant personal growth. It has been quite a journey— one marked by rewarding successes, profound challenges, and countless lessons learned along the way. It embodies the kindness and inspiration of the incredible individuals I was fortunate to be surrounded by, work with, and learn from.

I am grateful for the opportunity to contribute to the field and for the support of those who made this journey possible. To all who encouraged me, shared their wisdom, enriched my path, and brought depth and joy to my life: thank you.

First and foremost, I want to express my sincere gratitude to my supervisor, Aviad Frydman. Aviad, thank you for believing in my potential throughout this journey and for pushing me to achieve more. I am grateful for the opportunities you've given me to learn, grow and for the freedom to explore and discover. Your confidence in me has been invaluable. I deeply appreciate your genuine care for our well-being, as well as the thoughtful and encouraging way you celebrate our successes, which has fostered a positive and collaborative atmosphere in the lab. I am thankful for your guidance and constructive feedback as I discovered the beauty of scientific inquiry, the value of curiosity and developed both my skills and character along the way.

A big thanks to my lab members, whose shared frustrations and collaborative learning made this journey both productive and enjoyable. To my colleagues, thank you for the stimulating-insightful discussions and camaraderie. A special thanks to Ira- for your behind the scenes efforts to keep the lab running smoothly, and more than that, for your friendship. Whether sharing a laugh, talking through a problem, or simply venting when needed, I always knew I could turn to you.

I am fortunate to have worked with Olivier Bourgeois, who welcomed me into his lab during my first year of Ph.D. Olivier, thank you for teaching me not just the technical intricacies of sensitive thermodynamic measurements but also the value of perseverance, where I learned that when experiments give you lemon, you make *tarte au citron*! Beginning my Ph.D. under your mentorship, surrounded by the inspiring culture and beautiful nature of Grenoble, was a privilege I will always treasure.

I am grateful to the team at the Néel Institute, for welcoming me with such warmth, and making my time there both meaningful and fun— a combination which is rare and invaluable. The time I spent with you has left a lasting impact on my scientific approach. Working with such a group has been one of the highlights of my Ph.D. experience, and I am truly lucky to have gained friends for life.

Special thanks to the administrative team at Bar-Ilan University's Physics Department, especially Rita, who navigates the complexities of academic administration with incredible patience and efficiency, and always keeps an open door. To Yossi, Moshe, and Mark in the cleanroom, and the NanoFab team at Neel, thank you for sharing your expertise and guiding hands throughout the technical hurdles.

To the people in my life outside the academic world— who probably will never read these lines but have had an immeasurable impact on my success— thank you. To the Behar family, who adopted me with open hearts— your kindness has been a home away from home.

To my dear close friends, thank you for your patience and for being there through both the highs and lows. Your support, shared laughter, insights, tears, excitement, frustrations, and simple words of encouragement have meant more to me than words can express.

Finally, I owe my deepest gratitude to my beloved family for walking (and sometimes pushing) with me through this journey— Aba, Ema, Chenky, Miriam, Merav, and Savta. Your unwavering belief in me, and your love and your encouragement have been my foundation throughout this journey. Thank you for being my anchor, my cheerleaders, and my place of rest and renewal. I am also grateful to those in my family who may not have completed this journey with me but who nevertheless contributed to my early years and helped shape who I am today.

With a prayer for peaceful days, where each of us does our part to keep the wheel turning and make this world a better place.

Contents

List of Figures

List of Tables

Abstract

The Superconductor-Insulator Transition (SIT) is a pivotal quantum phenomenon in condensed matter physics, where systems transition from a superconducting state to an insulating state upon varying non-thermal parameters. At the heart of this transition are quantum fluctuations, offering insights into a quantum critical regime where neither full superconductivity nor full insulating behavior dominates. Despite extensive research, fundamental aspects such as the emergence and nature of exotic bosonic phases during the SIT, remain a topic of intense debate, with a number of unresolved questions, some of which this dissertation seeks to address.

This study aims to elucidate the underlying mechanisms of bosonic phases in disordered granular superconductor (SC) systems via two innovative methods: (1) Thermodynamic measurements, using a highly sensitive technique to study the specific heat of granular ultra-thin films of indium (In) as they are driven through the SIT, with a focus on the potential emergence of a Bose metal (BM) phase. These measurements were carried out in collaboration with Dr. Olivier Bourgeois' group at the Néel Institute, CNRS, Grenoble, utilizing their facilities; and (2) Transport measurements, examining the fundamental units of these phases—NS junctions—in engineered SC dot matrices of amorphous indium oxide (InO) on single-layer graphene (SLG). Both single dot rows (1D) and dot matrices (2D) arrays were studied to analyze their electrical properties by resistance and differential conductance measurements. Each chapter of this dissertation is organized around these two methods.

The findings include intriguing thermodynamic signatures in the specific heat of In films at intermediate layer thicknesses, where the $R(T)$ curves exhibited AM behavior with saturated resistance at low temperatures, observed during the transition from insulating to superconducting states as the material was driven through the SIT. A prominent secondary feature in the specific heat signal deviates from known behavior: the signal exhibits a sharp increase that remains relatively flat and constant at higher temperatures, rather than returning to the normal state signal. This is the first time such a secondary feature has been measured in specific heat of SC films. Consequently, anomalies in the entropy were derived. Additionally, a change in the dominant heat carriers was measured, indicating a unique characteristic specific to these intermediate layers.

Transport measurements provided novel insights into NS junction behavior, with unique oscillation and fluctuation patterns measured in both resistance versus gate voltage and conductance versus bias voltage at different gate voltages. These oscillations in conductance appeared inside

and outside the SC gap, with the most pronounced patterns observed in the 1D device. Our main analysis efforts focused on these conductance oscillation patterns, utilizing the 'singular value decomposition' (SVD) technique for the first time to analyze complex experimental data.

The nature of these new experimental observations is not yet fully understood. However, these findings shed new light on the intricate dynamics governing the SIT and the complexities of these fascinating Bose phases. They pave the way for future inquiries and advancements in quantum condensed matter physics, bringing us closer to a comprehensive understanding of these captivating quantum phases.

Chapter 1

Introduction

1.1 Superconductor to Insulator Transition (SIT)

Classic phase transitions are driven by thermal fluctuations and are characterized by a critical temperature, T_C. Below T_C, the system is at one phase, and above T_C, it transitions to a second phase. An example of a classic phase transition is the superconductor-normal state transition when a metallic system becomes superconducting at $T = T_C$. A different type of phase transitions are quantum phase transitions (QPTs), which occur at zero temperature, hence thermal fluctuations are not relevant. QPTs are driven by quantum fluctuations and are controlled by a non-thermal tuning parameter, g, such as magnetic field, thickness, or level of disorder. An example of a QPT is the superconductor-insulator transition (SIT), in which a superconductor transits to an insulator at zero temperature [1–15]. At $T = 0$, the QPT occurs at a quantum critical point (QCP), where $g = g_C$. For low but finite temperature, the transition is characterized by a quantum critical regime around g_C (see scheme 1.1), where quantum fluctuations dominate and the system is neither entirely a superconductor (SC) nor an insulator (I).

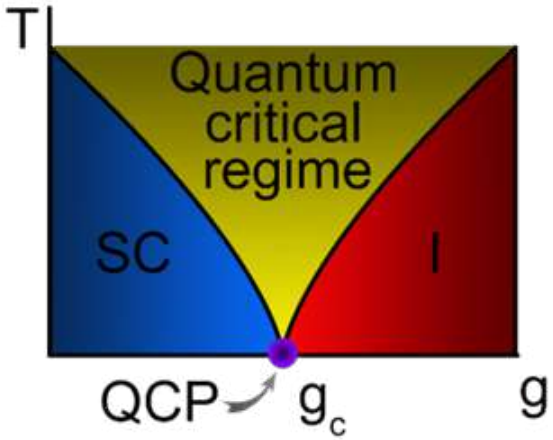

Figure 1.1: Scheme of the SIT as a function of the tuning parameter, g. g_C is the critical point where the phase transition occurs. At $g < g_C$, the system is in its superconducting phase, while for $g > g_C$, it is insulating. The 'fan' between the two phases denotes the quantum critical regime, with a width that depends on the temperature.

The SIT is a prototype QPT, which is experimentally accessible and, as such, holds special interest. Various experiments have been conducted to explore systems undergoing the SIT, with each experiment manipulated by a specific tuning parameters. These parameters include variations in film thickness [2–7], binary material composition [15], magnetic field [1, 8–11], electric field [12–14] etc. Notably, the vast majority of systems observed to undergo the SIT have been confined to the two-dimensional (2D) limit, where the sample thickness is smaller than the superconducting correlation length, ξ.
A plethora of exotic phenomena occurring across the different phases of the SIT and in the vicinity of the transition has been uncovered. This includes the emergence of exotic bosonic states, alongside the manifestation of quantum fluctuations. These phenomena beckon further exploration to unravel their underlying nature, a quest to which our research endeavors to contribute.

Several theoretical paradigms have been proposed to explain the SIT. This research specifically focuses on the "bosonic model" of the SIT, as it is most relevant to our experimental systems.

1.2 The bosonic model of the SIT

Fundamentally, the superconducting state can be described by a macroscopic wave function $\varphi = \varphi_0 e^{i\Theta}$, where φ_0 is the amplitude of the order parameter that is proportional to Cooper pairs (CP) density and Θ is the superconducting phase. Hence, macroscopic superconductivity requires phase coherence across the sample. The "bosonic model" of the SIT [16] is based on CP tunnelling from one superconducting region to another via Josephson coupling. When CPs can tunnel throughout the entire sample, phase coherence is achieved, enabling macroscopic superconductivity. Conversely, if CPs cannot tunnel, no coherence between the superconducting regions is achieved, and the system is in its insulating phase. A granular system serves as the prototype of the bosonic model. In such a system, the disorder is on a much larger scale than the system's atomic length. A typical example is a discontinuous superconducting film. The film contains superconducting "islands" (Fig.1.2), each being a superconductor. In such a system, the superconducting wave function is localized within each grain (island). In the absence of global phase coherence, there is no macroscopic superconductivity and the system is an electrical insulator. Global superconductivity fully appears when phase coherence percolates throughout the system. This is controlled by the tunneling ability of CP, which is related to two energies: (1) the Josephson energy, $E_J = \frac{\Phi_0 I_c}{2\pi}$, where Φ_0 is the inverse magnetic flux quantum and I_c is the critical Josephson current of the junction; and (2) the charging energy of the grain (associate with the Coulomb interaction) $E_C = (2e^2)/C$ where C is the capacitance of one grain. The ratio between these energies E_C/E_J determines whether a CP can tunnel between grains or not, and thus determines whether the system is a superconductor or an insulator [4].

(a) (b)

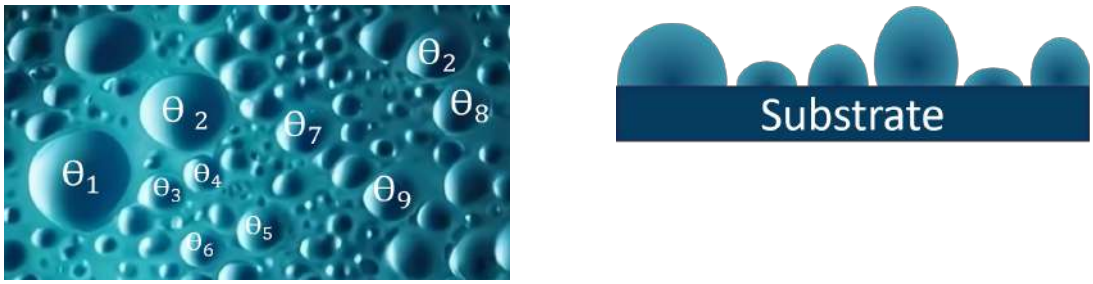

Figure 1.2: A sketch of a granular system. (a) Top view: Illustration of the superconducting islands, each with its distinct phase (b) Side view: Demonstration of the granular films' superconducting "islands" on a substrate.

The Bosonic model of the SIT is relevant not only to physically-morphologically granular systems but also to systems with the so called "emergent granularity". Variations in composition, density, disorder, or other properties within the system can lead to the formation of regions with distinct electronic characteristics, resembling individual grains or clusters within the material, akin to granular materials. The phase of these systems, similar to the case in granular materials, depends on the phase coherence of the CPs between the grains. Phase coherence allows for the collective flow of supercurrent, resulting in macroscopic superconductivity. In contrast, absence of coherence between the superconducting grains leads to an insulating phase.

This phenomenon of "emergent granularity" was proposed by Trivedi et al.[17], where calculations predict that, with increasing disorder, emergent electronic granularity occurs. SC domains, on the scale of the coherence length, are embedded in an insulating matrix and coherently coupled by Josephson tunneling. They show that at low levels of disorder, CP pairing amplitude is relatively homogeneous throughout the sample, leading to a SC phase of the system. As disorder levels increase, at $T < T_C$, the system self-organizes into superconducting blobs within an insulating matrix. The coherence between these grains is lost with increasing disorder, resulting in a system that is macroscopically insulating; however, it possesses non-coherent SC mesoscopic grains within it (see Fig. 1.3).

Their model successfully provides a unified paradigm for understanding the destruction of superconductivity in both initially grown granular films and homogeneously disordered films. This reinforces the similarity between the bosonic mechanisms underlying the SIT in these systems, which comprise superconducting grains and the coherence between them.

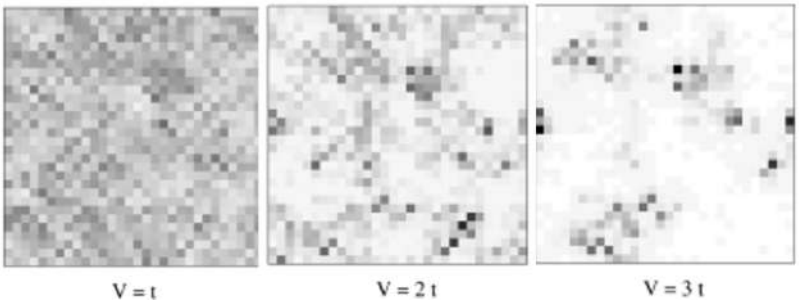

Figure 1.3: Pairing amplitude maps illustrating the evolution with increasing disorder strength, V. At V=t, the pairing amplitude is relatively homogeneous, while at higher values of V, self-organized superconducting "islands" emerge. Calculations were performed using the Bogoliubov-de Gennes method, see in source [17]).

An example for such an "emergent granular" system is a thin film of amorphous-InO (InO), which, although being morphologically uniform, has proven to possess emergent granularity in the form of superconducting "puddles" embedded within an insulating matrix [18].

1.3 Bosonic phases in the SIT

The SIT has been shown to possess exotic phases. These exotic phases are interpreted as bosonic phases, as they cannot be explained through a fermionic point of view, as detailed in this section. Their formation arises from the intricate interplay between Coulomb interactions and Josephson coupling, and they are characterized by collective electronic behavior.

1.3.1 Bose insulator

The term 'Bose insulator' (BI) refers to a phase of matter characterized by the **localization** of bosonic quasiparticles, leading to insulating behavior. In the SIT scenario, according to the bosonic model (Sec.1.2), this phase arises when the charging energy of CPs outweighs the Josephson coupling energy ($E_C > E_J$). As a result, the insulating phase comprises **localized** CPs, hindering coherent tunneling. This localization leads to the system exhibiting insulating behavior, despite the presence of CPs, which is somewhat counterintuitive. The formation of a BI is observed in granular or disordered superconducting systems near the QCP of the SIT, which are the systems under study in our research.

The transport properties of the SIT in granular systems are exemplified in Fig. 1.4, where the transport measurements of a granular lead film [3] driven through the SIT as a function of the thickness are presented. It is seen that the thinnest film (top curve) shows insulating behavior, with resistance increasing exponentially as temperature decreases, while the thickest film (bottom curve) demonstrates superconducting properties, with resistance dropping sharply at $T = T_C$.

Notably, T_C through the SIT is not well-defined, and the curves are characterized by broad

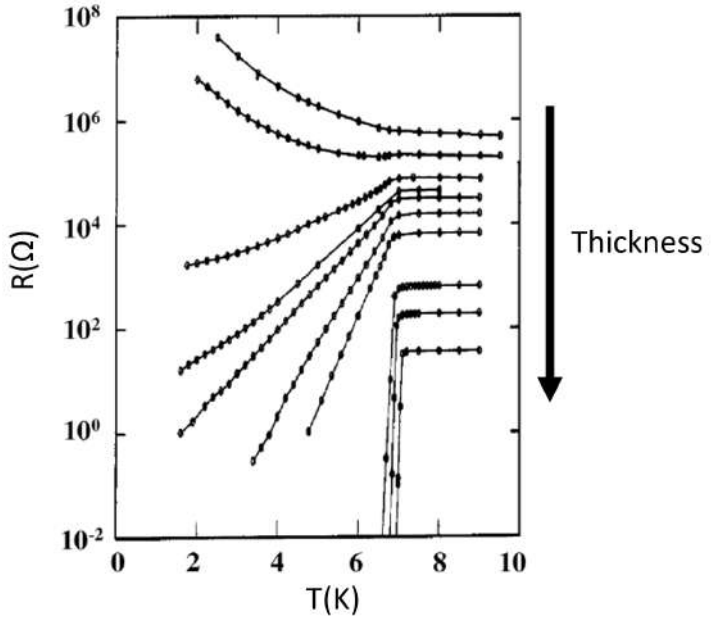

Figure 1.4: $R(T)$ curves of granular lead films, having different thickness exhibiting the SIT. The figure is reproduced from [3]

transitions with long "tails". Furthermore, an abrupt resistance change occurs at a temperature of $T \approx 7.2K$ even in the insulating film. The nature of this transition is interpreted by the bosonic model of the SIT. As the grains within the films are not coupled and $E_J < E_C$, the system exists in a 'bosonic insulator' state, characterized by resistance increasing exponentially as $e^{-\frac{\Delta}{T}}$. With increasing thickness, E_J surpasses E_C, facilitating phase coherence percolation throughout the sample and resulting in the transition to a superconducting state. The gradual nature of this transition leads to the broad transitions observed. With increasing thickness the transition become sharper, indicating the formation of increasingly larger continuous superconducting regions as grains become globally connected.

A strong manifestation of the BI is the experiment conducted by Sherman et al. [19, 20], where tunneling measurements were performed into two InO films close to the SIT, one on the SC side and the other on the insulating side. These measurements revealed the presence of a non-zero superconducting gap in both films, indicating the presence of CPs *within* the insulating phase of the SIT. These tunneling measurements and corresponding resistivity characterization of the two films are shown in Fig. 1.5.

This sustained gap, even in the insulating phase at the SIT, was predicted theoretically. Trivedi et al. [21] found that the superconducting DOS gap (in thin quench-condensed films) 'survives' throughout a disorder-driven SIT. They demonstrated that as the disorder level, V, evolves, the gap ω_{DOS} remains finite at both the superconducting and insulating states of the system. Although the gap was found to be inhomogeneous at different levels of disorder, it persists at every level. This behavior is illustrated in Fig. 1.6, where the DOS was calculated for various V values of the system at a fixed low temperature of $T = 0.1K$.

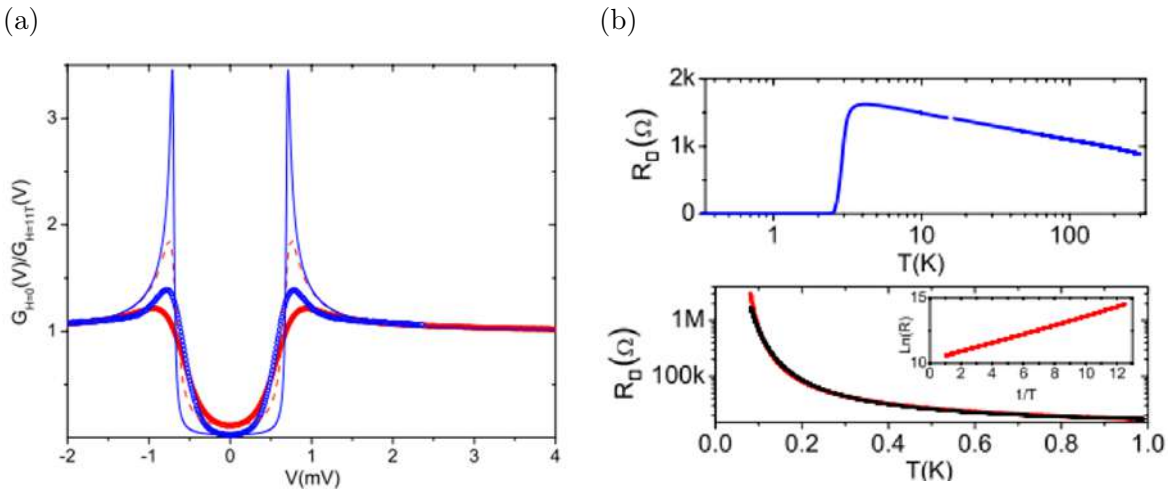

Figure 1.5: (a) Normalized tunneling DOS (dotted lines), at $1K$ (lines are fits to the BCS, see in origin) and (b) the corresponding transport measurements of two films of InO close to the SIT. Blue is a SC film and red is an insulating one. Both exhibits finite SC gap. Reproduced from [19]

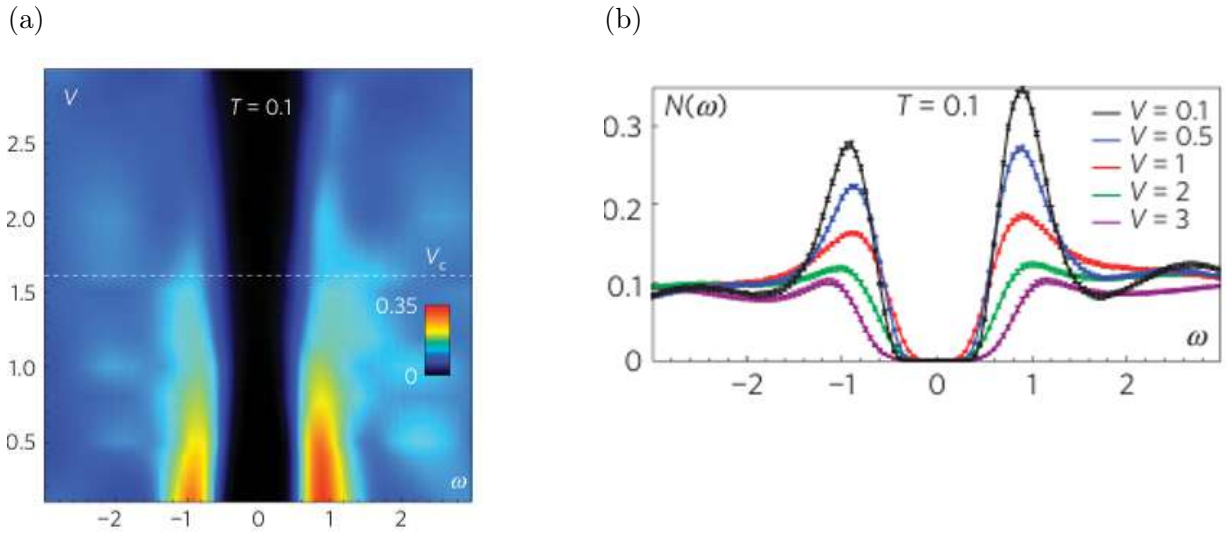

Figure 1.6: The DOS, ω_{dos}. (a) Disorder dependence of $N(\omega)$ at a fixed low temperature of $T = 0.1K$ and (b) representative spectra. A hard gap (black region) persists for all V above and below the SIT ($V_c \approx 1.6$). Reproduced from [21].

1.3.2 Anomalous metallic state

Experimentally, as a variety of systems were driven through the SIT using different tuning knobs and different materials, in many of them a metallic state was observed between the insulating phase and the SC phase of the system. One of the first experiments where the metallic phase was measured is in the work of Jaeger et al.[22], where thin films of various materials were studied as they were driven through the SIT with increasing thickness. $R(T)$ curves of thin films of Ga and Pb are presented in Fig. 1.7(a,b) respectively. It is evident that the films' resistance evolves

from "infinity" (insulating films) to approximately zero resistance (superconducting films) as their thickness increases, and in between, the resistance levels off and saturates at a finite value, indicating a metallic state.

Another early experiment was conducted by Hebard et al.[8], in which they used magnetic field to tune the SIT of five 100Å thick InO films, at different degrees of disorder. Fig. 1.7(c) depicts the $R(T)$ curves of an InO film, with $T_c = 0.29K$, as a function of magnetic field. It shows a clear regime where the resistance saturates at low temperatures, indicating metallic behavior.

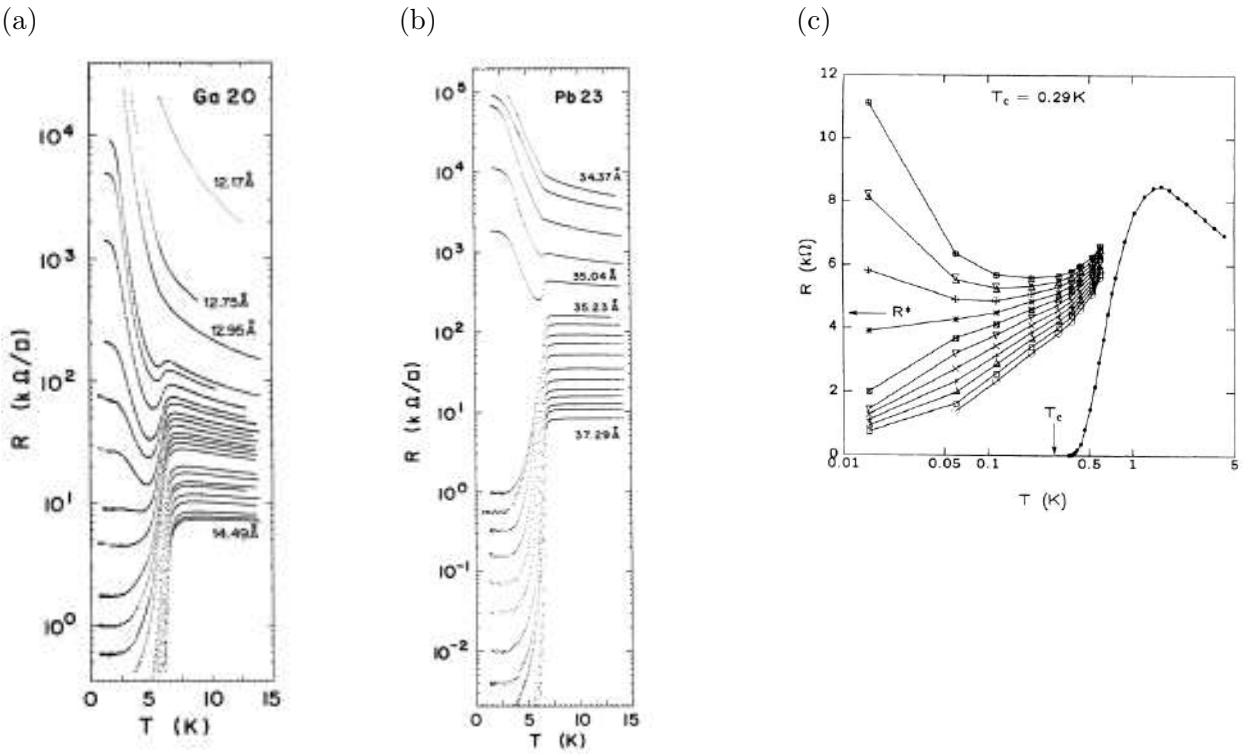

Figure 1.7: $R(T)$ curves of different materials driven through the SIT, using various tuning parameters: (a) Gallium and (b) Lead, with varying thicknesses. (c) Log plots of an InO film measured under different magnetic fields. The zero field is represented by the black dotted line, while non-zero fields are indicated by open symbols. Notably, near the quantum critical point (QCP), finite resistance was measured at low temperatures in all systems. (a, b) reproduced from [22], (c) from [8].

These two experiments represent just a small example of the many conducted to explore the SIT, where a metallic state was observed (for review, see [23]). Despite the diversity in experimental setups and materials, the properties of the metallic state observed are quite similar. As the temperature decreases, the resistivity exhibits anomalous behavior: it saturates at low temperatures to values significantly different from those predicted by the Drude model (σ_D). Specifically, in some stages, the resistivity initially drops, as if the system were approaching a SC state. However, it then saturates at a low temperature to a value much smaller than σ_D. In other stages, the resistivity increases as if the system were approaching an insulating phase, but

then it saturates at low temperatures to a higher value than expected from the Drude model. According to Drude theory, the conductivity of (3D, pure) metals is given by: $\sigma_D = e^2 D\nu$, where the diffusion coefficient D is defined as $D = \frac{v_F l}{3}$, with v_F being the Fermi velocity, l the mean free path and ν the electron density of states (DOS) at the Fermi energy. In both the studies by Jaeger et al. and Hebard et al. presented above, considering the stages where the resistance drops and then saturates as examples, the measured resistivity at the plateau is significantly lower than the expected σ_D, violating the Wiedemann-Frantz law ([24]). This metallic behaviour which cannot be explained by the Drude or Fermi liquid theories, has led to its designation as the "anomalous Bose metal" (BM) state.

The metallic behavior observed in variety of experiments on 2D systems has been the subject of ongoing principled debate regarding its classification as a true ground phase or merely an experimental artifact (see [23]).

For instance, Tamir et al.[25] demonstrated that an observed metallic behavior in two different 2D systems is an experimental artifact. By measuring two different 2D SCs, they showed that the metallic behavior can be eliminated by filtering external radiation, indicating the high sensitivity of these films to external radiation perturbations, which suppress the superconducting state. Other experimentalists argue that sufficient precautions were taken to ensure the quality of the experiments.

The emergence of this anomalous metallic state reopens fundamental questions about the nature of this phase transition and present theoretical challenges. It raises the debate on whether the SIT is a direct transition or a combination of two distinct QPTs: the quantum transition from a superconducting to metallic state (QSMT), followed by another QPT where the metal transitions to an insulator (QMIT). Moreover, this phenomenon has been observed in various **2D** systems, which poses theoretical problem, as it sparks renewed discussions on the possibility of a metallic state in two dimensions. Since 1979, when Abrahams et al. proposed the scaling theory of localization [26], also supported by experiments, it has been widely accepted that a metallic state cannot exist in 2D, since (at the thermodynamic limit) all 2D systems are strongly localized. Therefore, as the temperature is decreased, the resistance should increase exponentially, approaching infinity at zero temperature in the thermodynamic limit. This topic is extensively reviewed and analyzed, with arguments and theories presented (for a comprehensive review, see [23, 27]).

Several new theories have been proposed to address the BM [24, 28, 29]. Most of these theories suggest that this metallic state results from a suppressed or 'failing' superconducting state rather than being a genuine ground state.

One theory, proposed by Spivak et al. [24, 29], attributes the metallic state to quantum fluctuations in the amplitude of the superconducting order parameter near the transition, which dominate the physical characteristics of the system. According to this model, as the transition is approached, the electron wave functions become strongly nonuniform, leading to nonuniformity in the order parameter at the transition point. The formation of BMs is attributed to the fluctuations in E_C and E_J near the QCP of the SIT, reflecting the interplay between phase and number fluctuations of the CPs. E_C between electrons in the grains suppresses the fluctuations

of the number of electrons, and due to the uncertainty principle, it increases the fluctuations in the amplitude of the phase fluctuations. In the insulator phase, fluctuations in the number of CPs cease, resulting in an infinite uncertainty in the phase. Conversely, in the superconducting phase, phase coherence is established, resulting in an infinite uncertainty in the number of CPs.

The works of Shimshoni et al. [30] and Kapitulnik et al. [31] suggest that dissipation may be key to understanding the BM phase. However, this dissipation, which results in a metallic state, arises not from an external source, which is unlikely to persist at $T = 0K$, but rather from a self-generated mechanism within new phases. One such phase is described by Dalidovich et al. [27, 32], in the quantum phase glass model.

In this model, disorder in the distribution of tunneling amplitudes causes SCs to lose global phase coherence while retaining local phase coherence, becoming glassy. Within this glassy phase, the phase on each lattice site remains fixed, but the directions vary from site to site, creating a phase or rotor glass where phases are frozen along noncollinear directions. The slow phase relaxation (the effective order parameter) in the glassy phase, indicating a high density of low-lying excitations, prevents bosons from localizing. Bosonic excitations moving in a dissipative environment with numerous 'false minima' metastable states take an exponentially long time to find the ground state, thus remaining delocalized. Consequently, a metallic state emerges at zero temperature, characterized by a critical resistivity that scales with a universal value, consistent with experimental observations. Thus, glasses, with their sluggish phase dynamics and intrinsic low-lying excitations, offer a pathway for delocalized bosonic excitations to ultimately create a metallic state.

Currently, there is no unified theory that comprehensively accounts for all observed metallic states across various systems and tuning parameters. In our research, we aim to address the unresolved core question of whether the metallic phase observed during the SIT is indeed a genuine phase, utilizing specific heat measurements. Specific heat measurements are a powerful experimental approach for identifying both the bosonic insulator and bosonic metal exotic states at the SIT, as they are true thermodynamic measurements that provide insights into the energy scales and collective excitations associated with bosonic phases. Given their pivotal role in our research, a detailed explanation of this measurement is provided in the subsequent section.

1.4 Heat capacity measurements through the SIT

Heat capacity (C) is a fundamental thermodynamic property that quantifies the amount of heat energy (Q) needed to raise the temperature of a material by a certain ΔT, given by the equation: $\Delta Q = C\Delta T$. As heat is absorbed in a solid lattice, it is transported both by phonons and by conductance electrons. At the limit of low temperatures ($T < \theta_D$, the Debye temperature), the contribution of the phonons is derived according to Debye's model [33] to be proportional to T^3, while the electrons' contribution is linear with T. Therefore, the heat capacity can be written as a sum of these two contributions:

$$C = \gamma T + \beta T^3 \tag{1.1}$$

Here $\gamma = \frac{1}{3}K_B^2 T D_F \pi^2$ and $\beta = \frac{12\pi^4}{5} * \frac{nK_B}{{\theta_D}^3}$, where K_B is the Boltzman constant, D_F is the density of states at the Fermi level and θ_D is the Debye temperature. Hence, at low temperatures the electronic contribution is expected to be the dominant term in C. Using the thermodynamic relation $C(T) \sim T\frac{\partial S}{\partial T}$, one can see that as the entropy, S, of a system is changed, the heat capacity is affected accordingly. This occurs when a system undergoes a phase transition, where it transverses from a disordered phase (high entropy) to an ordered one (lower entropy). For a first-order phase transition, (e.g the transition from liquid water to ice), the entropy shows a discontinuity, resulting in a delta function in C. In the case of a second order phase transition, such as the transition from a normal (resistive) state to a superconducting state, there is a change in the entropy of the electrons which are unpaired above T_C and paired below it (at the superconducting phase), resulting in a heat capacity jump at the transition temperature. When the system is cooled below T_C the electronic component of the heat capacity in the SC (C_{es}) rapidly declines as the temperature decreases (see Fig. 1.8) and it reduces exponentially ($C_{es} \sim \frac{-\Delta}{K_B T_C}$) reaching zero as T approaches 0.

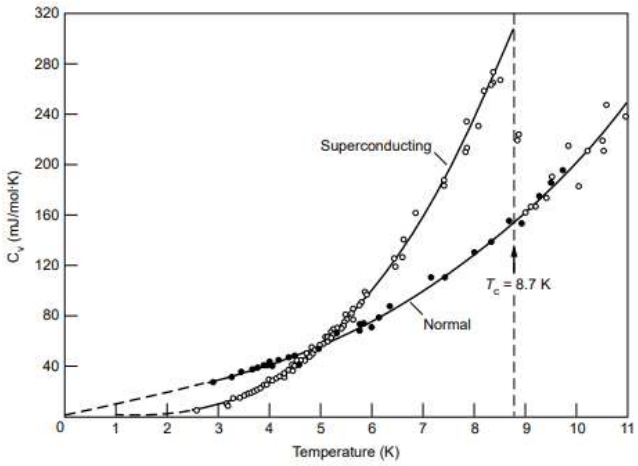

Figure 1.8: The molar heat capacity signature vs temperature of niobium (hollowed dots) and of a normal metal (black dots). For the niobium- a jump is seen at the superconducting transition, at its $T_C = 8.7K$. Taken from [34].

The heat capacity is an extrinsic property of a material, while the intrinsic property is the *specific heat capacity*. The specific heat, C_p, is the amount of heat required to raise the temperature of one unit mass of a substance by 1 Kelvin, defined as: $C_p = \frac{Q}{m \cdot \Delta T}$ where m denotes the mass of the substance.

The thermodynamic properties of a system holds a lot of information, as they are sensitive to all the degrees of freedom on the system. As such, measurements of C_p are a great tool to gain information on the different phases of a system, and, in particularly, on the bosonic phases of disordered systems as they are driven through the SIT. In the past, our group was involved in pioneering work of specific heat measurements of thin-films of lead (Pb) undergoing a SIT as a function of thickness. Poran et al. [35] used an innovative measurement setup allowing the specific heat measurements of ultra-thin films simultaneously with their transport properties as

they were tuned through the SIT. The main results of this work are depicted in Fig. 1.9(b), showing the superconducting electronic specific heat (C_{se}) as a function of thickness, alongside the corresponding $R(T)$ curves (Fig.1.9(a)).

The $R(T)$ curves reveal the distinct phases observed as the system was driven through the SIT, transitioning from an insulating state (thin films, top) to a superconducting state (thicker films, bottom). Notably, these transport measurements are consistent with the bosonic model for the SIT, reflecting the granular nature of the lead system, similarly to those shown in Fig. 1.4 discussed in Sec.1.3.1. Importantly, there exists a range of thicknesses where the system exhibits metallic behavior, adding to the ongoing debate surrounding the possibility of an intermediate metallic state.

The critical temperature, T_C, of the films as measured by specific heat (Fig.1.9(b)) occurs close to $T = 7.2K$, corresponding to the Pb bulk T_C, throughout the *entire* SIT, evident in both insulating and superconducting films. This observation is also consistent with the bosonic model, as specific heat measurements are insensitive to the coherence between grains but rather reflect their internal properties. Hence, as each Pb grain transitions to its superconducting state, C_p exhibits a discontinuity, both in the insulator (which is, in fact, a bosonic insulator) and in the superconducting films.

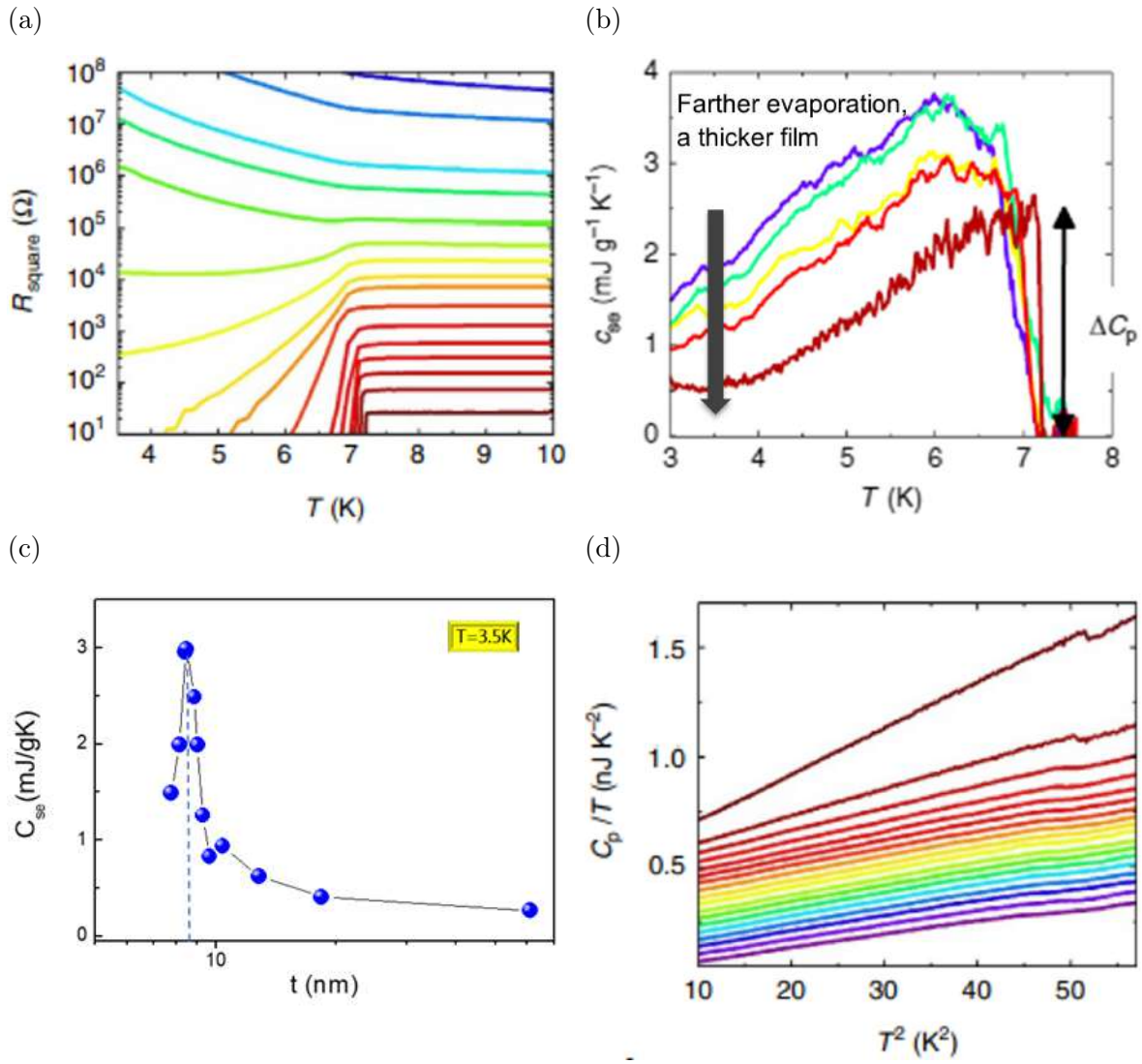

Figure 1.9: Main results of Pb thin-films, reproduced from [35].(a) R(T) measurements as a function of the films' thickness (b) Cse measurements of number of thin Pb layer as they are driven through the SIT. The jump in Cse is at the transition temperature, $T \sim 7.2K$, and grows as the sample is thinned (c) The Cse jump (at 3.5K) as a function of the films thickness. The jump exhibits higher values for thinner films and peaks near the transition (d) The reduced C_p vs T^2 of the different Pb films.

Fig.1.9(c) reveals an additional surprising feature: the thinner the SC film, the higher the jump of the specific heat ΔC_p and the excess specific heat below T_C and it peaks close to the QPT. This is indicative of the system's increasing entropy as it approaches the transition and is interpreted as evidence of strong quantum fluctuations in the vicinity of the QCP. Such findings highlight the importance of specific heat measurements in investigating phase transitions, particularly at a QPT.

When examining the reduced specific heat ($\frac{C_p}{T}$) plotted against T^2 for the measured films (see Fig. 1.9(d)), linear curves were observed. Conventionally, one would expect constant lines in such a representation, indicating the dominance of heat transport by electronic carriers at low temperatures, as described by equation 3.4. The observed behavior of the reduced C_p contradicts

this expectation and suggests a very significant contribution from phonons. In our research, we aim to understand the behavior of electronic heat carriers. Therefore, we endeavor to minimize the contribution of phonons to C_p, as it may potentially surpass that of electrons, thereby enabling the observation and analysis of the latter's behavior.

1.5 Gate induced SIT

Apart from characterizing the bosonic phases from a thermodynamic perspective, we also endeavor to comprehend the microscopic electronic phenomena within them. To achieve this, we intend to measure the differential conductance of granular systems in the proximity of these bosonic phases. Our approach involves utilizing graphene as a substrate for these devices, as described below.

In recent years, new avenues for tuning parameters of the SIT have emerged with the discovery of graphene and advancements in the field of two-dimensional electron gas (2DEG) materials [36–38]. Graphene, in particular, has arisen as an excellent substrate for tuning the SIT due to its unique band structure, which allows easy control of carrier density (n) by applying a gate voltage. Consequently, when decorating graphene with a granular SC system, the coupling between the grains can be controlled by gating the graphene, allowing the tuning of E_J and E_C. The carrier density of graphene (electrons) increases with higher applied voltage, generating stronger coupling between the grains (applying a high negative voltage hole-couples the grains). This enables the control of the coupling between the grains (due to Josephson tunneling through the graphene), and thus generates a gate-induced SIT. In the work of Bouchiat et al. [36] discontinues Sn was evaporated on a graphene substrate, creating a self-assembling granular system (Fig.1.10(a)). This random-granular system was driven through the entire SIT, by applying different gate voltages (V_g) on the graphene substrate. At low V_gs the system was in its insulating phase, and at higher V_g values, the system turned to a SC. The corresponding R(T) curves for the different V_gs values are displayed in Fig. 1.10(b). Implementing the same methodologies, this research group conducted a subsequent study [37], where the system was engineered to create an ordered array of Sn discs on top of the graphene substrate (see Fig. 1.10(c)). Once again, the system exhibited an SIT, as can be seen in Fig. 1.10(d). It is noteworthy that in both systems, a BM state was observed over a wide range of V_g values, as evidenced by saturated resistance at low temperatures. This observations contribute to the ongoing debate regarding the feasibility of a genuine metallic ground state during the SIT.

In these works, tin was utilized to induce superconductivity in graphene. The carrier density of tin is much higher than the maximum achievable n of graphene. This difference caused a significant shift in the energy level of electrons within the proximized regions of graphene, pushing them way above the carriers densities achieved in graphene. In our study, we coupled graphene to amorphous indium oxide (InO). Unlike tin, InO possesses a lower carrier density (further details in Section 3.2.2). Therefore, when combined with graphene, this choice of SC can lead to a scenario where the Fermi levels of both the proximitized and normal regions of graphene are similar. This alignment of energy levels reveals new phenomena and observations. In a

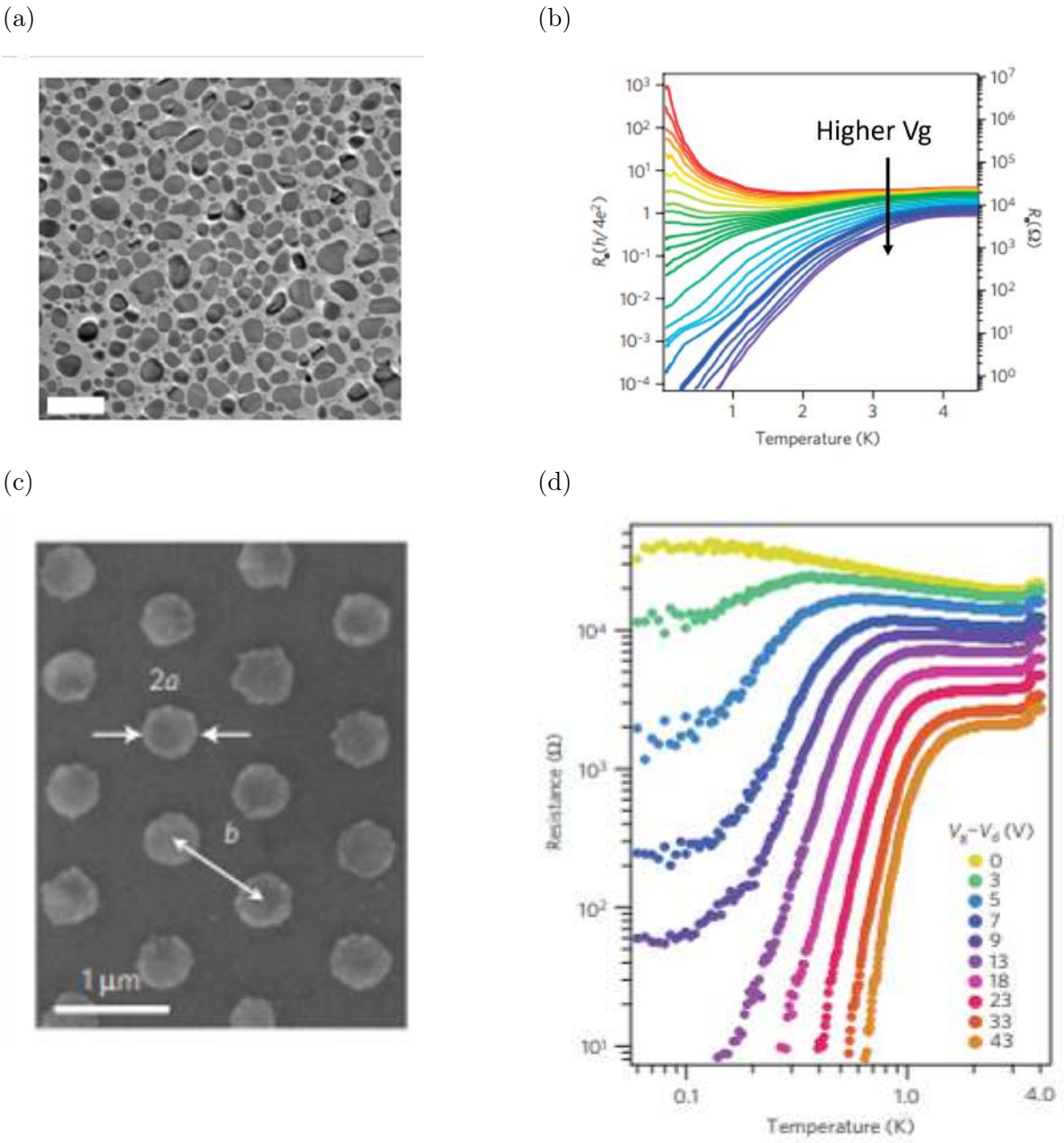

Figure 1.10: Granular tin systems ontop of CVD graphene. Top row: self assemble tin (a) 10nm thick tin islands (b) R(T) measurements at different V_gs. Addapted from [36]. Bottom row: Ordered tin discs arrays (d) 50nm thick tin discs, with dimensions of $b = 1\mu m$, and $2a = 400nm$ (d) R(T) curves at different V_gs. Taken from [37]. Both systems undergo the SIT, traversing from an insulating state at low V_gs to a superconducting state at high V_g.

recent study by our research group, conducted by Daptary et al. [39], graphene was coupled to a $30nm$ thick layer of InO. As explained in section 1.2, InO possesses emergent granularity, and consequently, when coupled with graphene, it induces proximity-based SC regions in the graphene layer, imbedded in the normal state background. Conspicuously these areas are characterized by a difference in Fermi energy. A schematic sketch of the $a : InO/SLG$ device used in the study of Daptary et al. is illustrated in Fig. 1.11(a). The superconducting InO grains (in red), embedded within the insulating layer (light red), induce superconducting regions in the

underlying graphene (light blue "mirroring" islands in the graphene layer).

The study showed that when graphene is coupled with a low n SC, the system exhibits two distinct charge neutrality points. One corresponds to the normal regions of graphene, known as the Dirac point (DP), while the other emerges in the proximitized superconducting graphene, termed the "superconducting Dirac point" (SDP). The latter can be reached thanks to the low n of the InO.

The resistance peaks observed in an $a : InO/SLG$ device, where the InO was deposited at an O_2 partial pressure of 4×10^{-5}, are illustrated in the top panel of Fig. 1.11(b). To distinguish between the two neutrality points and determine which corresponds to the DP and which to the SDP, Hall measurements of the device were conducted under various magnetic fields. The results are presented in the lower panel of Fig. 1.11(b). The DP is at $V_g = -80V$, where $R_{XY} = 0$, while the R_{xx} peak, at $V_g = \approx -10V$, corresponds to the SDP.

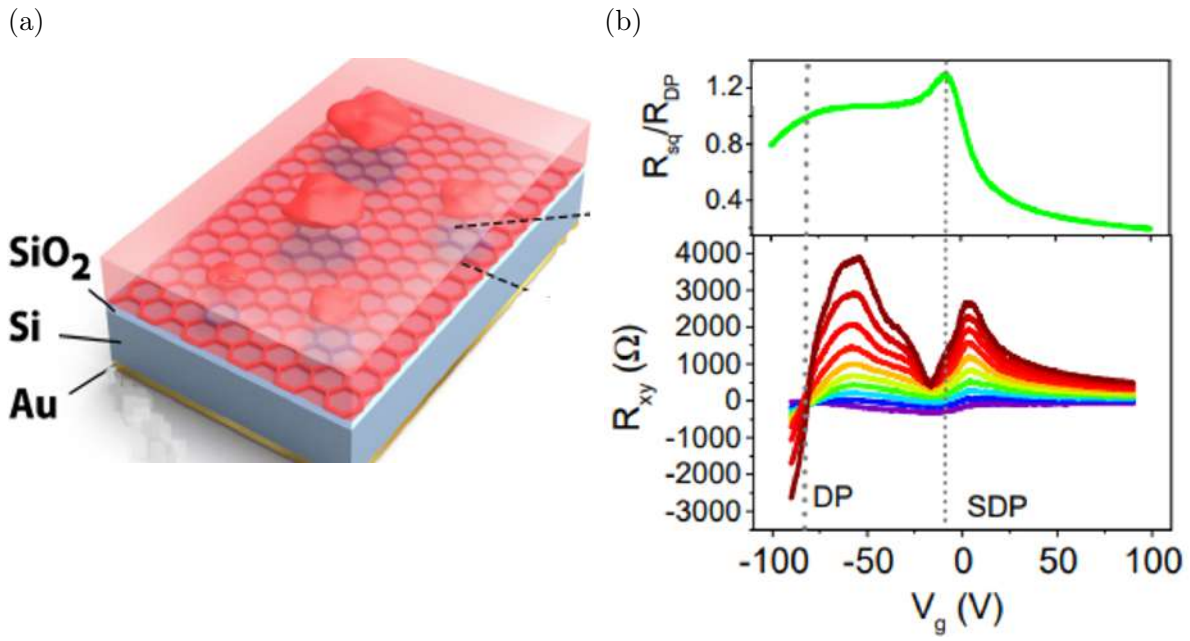

Figure 1.11: (a) Schematic sketch of the $a - InO/SLG$ device, showing superconducting InO grains (red) embedded within the InO insulating layer (light red) and the resultant proximity-induced regions in the graphene underlayer (light blue). (b) Resistance behavior of the device as a function of V_g at $T = 1.7K$. The upper panel displays R_{sq} at $B = 0T$, showing two distinct peaks. The lower panel shows Hall resistance, R_{xy}, under varying magnetic fields (up to $B = 9T$). The DP is identified at $V_d = -80V$, corresponding to $R_{xy} = 0$. Taken from [39].

In this experiment, a **layer** of InO was uniformly deposited onto graphene [39, 40], covering the entire surface of the graphene substrate. This led to proximized disordered superconductivity throughout the graphene layer, with randomly distributed normal-superconductor (NS) interfaces interspersed within it. In our research, we aimed to model different geometries dominated by NS junctions, where the N is a low n material.

Two distinct properties of graphene/SC interfaces play a central role in our study: Andreev reflection and Klein tunneling.

1.6 Andreev reflection and Klein tunneling in graphene

Graphene itself does not exhibit superconducting properties. However, when it is coupled to a SC, superconductivity is induced in the graphene due to the proximity effect. In this effect, which occurs when a normal metal (N) is coupled with a SC, the superconducting properties such as the SC wave function extend into the adjacent non-superconducting material inducing superconductivity within it. Andreev reflection (AR) processes offer a microscopic view on how this proximity effect operates; at the interface between the normal-metal and the SC (NS), incident electrons are retro-reflected as holes, resulting in the transmission of Cooper pairs— each carrying a charge of $2e$— and the flow of a dissipationless supercurrent in the SC. This conversion process, known as AR [41], is illustrated in Fig. 1.12(a). The current-voltage characteristics of N-S junctions were studied in detail in the BTK theory [42]. The BTK theory demonstrates that the transmission coefficient across such interface, is strongly influenced by the energy barrier, specifically the V_F difference between the N and S regions. As this difference in V_Fs increases, the transmission probability decreases, ranging from 1 for perfect transmission (when the V_Fs match) to 0.

When the N region is confined by two SCs, forming an SNS junction, Andreev retro-reflection (ArR) induces localized states within the normal region (schematically depicted in Fig. 1.12(b)). These confined states are referred to as Andreev bound states (ABS), which result in the formation of quasi-particles with discrete energy levels within Δ of the SC. These states play a crucial role in various phenomena and devices, including Josephson junction.

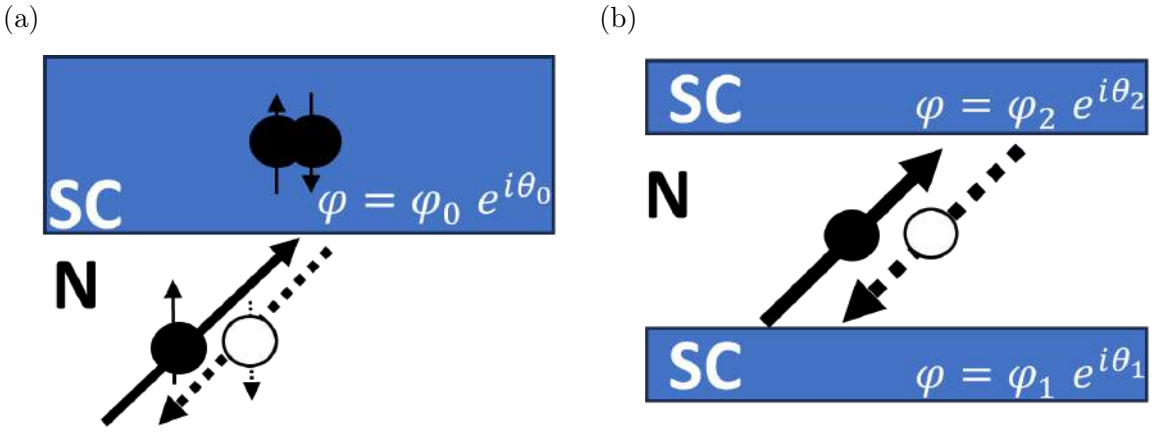

Figure 1.12: Schematic representation of Andreev retro-reflection (ArR). Incident electron (black full circle and arrow) undergo retro-reflection as hole (hollow circle, dashed line), while Cooper pair with a charge of $2e$ is transmitted into the superconducting region. (a) ArR at the interface between a normal metal (N) and a superconductor (SC). (b) ABS in a metal, created as electron is ArR in between *two* SC.

When graphene serves as the coupling medium between two SC, an additional process known as Klein tunneling occurs. The electrons in graphene can be characterized as Dirac fermions (with the holes being the positrons). These fermions move at **constant velocity** V_F, approximately $V_F \cong \frac{C}{300} \cong 10^6[m/s]$ (where C is the speed of light), regardless of their energy. This is due

to the unique Dirac cone band structure of the graphene, resulting in a linear energy dispersion given by $E = \hbar V_F K$.

As a consequence of this constant velocity, Dirac fermions cannot backscatter when encountering a potential barrier (as their velocity cannot be zero). Thus, even when the energy of an electron in graphene is smaller than the height of the barrier, it has a finite probability of tunneling through it with minimal attenuation ([43, 44]). This intriguing behavior is known as the Klein paradox for massless Dirac fermions. It dictates that when an electron in the graphene moves to the right (for example) and encounters a potential barrier, it can only be scattered into a state of either right-moving electron or left-moving hole.

Therefore, unique behavior occur at the NS interface in graphene; even in the case of a V_F mismatch, AR will always take place. At normal incidence ($\alpha = 0$), the electron-hole conversion happens with unit probability, even if there is a large mismatch between the Fermi levels (Λ_F) at the two sides of the interface.

These phenomena are combined in our experiment, where we investigate *graphene* devices coupled to superconducting ordered dot matrices of InO. As a result, distinct regions are formed within the graphene: low n superconducting regions induced by the InO, and normal state areas. These different regions within the graphene form NSN junctions, where Andreev retro-reflection (ArR) induces localized states [41, 45, 46]. Given graphene's tunability, one can control the strength of the barrier between these regions and the resulting current in these junctions.

This tunability of the graphene gives rise to a special reflection scenario. In ultra-clean (weakly doped, low-disordered) graphene devices, specular reflection can be achieved. For low E_F, ($|E_F| < \Delta$), **interband** Andreev specular reflection occurs, where the hole undergoes an interband transition, from the CB to the valance band (VB), changing its effective mass sign and resulting in specular reflections. In this case, the incident angle, α, becomes a non-trivial function of E_F to conserve momentum and energy. Moreover, in such clean graphene devices, since E_F can be continuously tuned, the crossover between the two AR processes can be measured and characterized [46, 47]. For $|\epsilon| < |E_F|$, intraband retro-reflection occurs, and for $|\epsilon| > |E_F|$, interband Andreev specular reflection occurs, with a clear difference signature between the two reflections in the subgap conductance [45, 47].

However, in our experiment the regime of $E_F \leq \Delta$ isn't accessed. Our devices are fabricated on top of a 285 nm SiO layer, and our $\Delta_{InO} = 0.7meV$. This places us in an energy regime where we experience strong potential variation (up to $\delta E_F \approx 50meV$) due to charge impurities, which is much larger than our SC Δ. Moreover, the SC InO contains inhomogeneities. Thus, both phenomena of ArR and the Klein paradox play integral roles and contribute to our experimental results. However, we do not consider Andreev specular reflection processes at our interface.

Chapter 2

Motivation

Investigating the SIT is of great interest as it provides a fascinating opportunity to delve into the quantum realm of disordered SCs and uncover fundamental properties that defy conventional understanding. The SIT is a quantum phase transition driven by quantum fluctuations and controlled by a non-thermal tuning parameter, offering insights into the quantum critical regime where quantum fluctuations dominate, and the system is neither a superconductor nor an insulator. What unfolds in this critical regime, where the system straddles the boundary between insulator and superconductor? Can we understand the exotic phenomena that emerge, shaping our understanding of the quantum landscape? What is the source and effects of the strong quantum fluctuations measured at the vicinity of the transition? Particularly intriguing are the exotic bosonic phases; the presence of a superconducting gap within the insulating phase (Bose insulator), and the anomalous intermediate metallic state (Bose metal) observed during the transition. Is it a true anomalous metallic ground state, or does the system undergo a direct quantum phase transition? These captivating questions, and more, are yet to be fully answered. The objective of this research is to contribute to our understanding of the complex phenomena underlying the SIT, particularly focusing on the emergence of the bosonic phases. While the full resolution of these mysteries remains a challenge, our work aims to provide new insights and take a step forward in unraveling the intricate dynamics at play. Using new approaches and innovative techniques, we aim to address two primary questions regarding the bosonic phases: (1) identification of the existence of a true metallic ground state during the SIT, explored through thermodynamic measurements, and (2) characterization of the bosonic phases by transport investigation of its building blocks- NS junctions.

In this research we studied the impact of disorder on the SIT, specifically focusing on the influence of disorder on the properties of *granular* superconductors undergoing this QPT. To achieve this, we studied two systems using different experimental approaches: thermodynamic measurements for one and transport measurements for the other. These methods allowed us to explore granular systems across various phases of the SIT and within the quantum critical regime. To investigate the feasibility of a BM phase during the SIT, we employed a highly sensitive thermodynamic approach, while to facilitate the study of the fundamental building blocks of the bosonic phases— Josephson junctions— we engineered a granular system in the

form of ordered dot matrices, which were characterized using transport measurements.

Thermodynamic measurements

To gain further insights into the SIT and the bosonic phases that may occur, we study the thermodynamic property of specific heat (C_p) in ultra-thin films of granular indium with varying thicknesses as they transition from an insulator to a superconductor. As C_p has proven to be a powerful tool for probing QPTs, our research aims to search for indications of a secondary C_p peak, which could be a signature of the presence of an additional transition to an intermediate metallic state, as well as the presence of strong quantum fluctuations near the QCP. Such signatures can clarify whether the SIT is a direct transition or involves an intermediate second quantum-metallic-superconductor transition. Moreover, C_p measurements provide a thermodynamic approach that allows to analyze the behavior of the insulating side of the transition. Unlike transport measurements, it is not limited by the percolation effects of electrons throughout the entire sample.

In order to do so, we opt to study a granular *indium* (In) film as it undergoes the SIT. We specifically choose to study ultra-thin layers of (In) due to the combination of three key properties:

1. Its critical temperature of $T_c = 3.4K$, which falls within the middle of our experimental temperature range.

2. Its higher Debye temperature ($\theta_D^{In} = 129K$) compared to Pb, previously studied ($\theta_D^{In} = 129K > \theta_D^{Pb} = 88K$), results in a ratio of approximately 3 in their phononic contributions. This decision aims to reduce the phononic contribution to C_p at low T, thus enabling the focus on electronic effects. The significant phononic contribution in Pb obscures the electronic effects, as was discussed in Section 1.4. Moreover, this substantial phononic contribution in Pb may lead to the excess C_p and entropy that were measured before.

3. Its latent heat of vaporization, $\Delta H_{Vaporization} = 231.5KJ/Mol$, which enables to quench-condensed it.

This combination of properties makes In a suitable material for our experiment, offering a temperature window that captures the system behavior above and below T_c, while enhancing the electronic contribution to C_p due to its lower β (phonon contribution).

By measuring C_p, we suggest to obtain valuable insights into the system's behavior during the transition, at and around the quantum critical point, as well as on the nature of quantum fluctuations near criticality.

Microscopic electronic characterization of building blocks of the Bosonic phases- dI/dV measurements

As our research aims to enhance the understanding of the processes underlying bosonic phases characterized by NS junctions, we fabricated an **ordered array** of InO islands on graphene. By doing so, we can control where superconductivity is induced within the graphene, leading

to the formation of SNS junctions within it. This control allows us to isolate and characterize individual SNS junctions, enabling a detailed study of their properties.

These ordered arrays of low n superconducting islands offer a unique opportunity to investigate the fundamental building blocks of bosonic insulator- NS junctions. The periodic low n system provide access to real granular system and facilitates the study of Andreev reflection processes in low-density S-N junctions, where the carrier density in the superconducting regions is possibly lower than in the normal ones. In order to gain a more thorough comprehension of these building blocks, we expand our investigation to include periodic **1D** systems. Smaller systems are more easily modulated and comprehended, facilitating a deeper exploration of their properties. Transport measurements, being global measurements, depend on the percolation of electrons throughout the entire sample, and therefore are influenced by the number of available electron trajectories and impurities present in the sample. By studying the transport properties of these different ordered dot systems, we can explore the influence of dimensionality and provide valuable insights into the interplay between disorder and superconductivity. Furthermore, our analysis focuses on **differential conductance** ($\frac{dI}{dV}$) measurements, as we systematically tuned the gate voltage on the graphene substrate. This approach allows us to detect different Andreev reflection patterns between the SNS junctions and signs of superconductivity at various phases of the system, particularly in its non-superconducting phase. By studying the differential conductance, we seek to uncover the microscopic electronic conduction processes in disordered granular systems. Ultimately, our goal is to enhance the understanding of bosonic phases by gaining insights into these fundamental aspects.

Chapter 3

Experimental Methods

3.1 Heat Capacity Measurements

3.1.1 Calorimetric Cell Preparations

Measuring the heat capacity (C) of thin films is a challenging task, primarily due to the significant substrate contribution. This is particularly true for thin films with ultra-small masses (few tens of nanograms), as their contribution to the C is much smaller than that of the substrate, and therefore can be overshadowed by it. Hence, a preparation of a special nano-sensor is necessary to accurately measure the C of such thin films. Utilizing a unique fabrication method [48], we can effectively mitigate the substrate's contribution and successfully measure the C of these ultra-thin films. The following subsections detail the fabrication steps of the nano-sensor.

Silicon Membrane Thinning

The fabrication process begins with a silicon nitride/silicon/silicon nitride sandwich chip ($SiN/Si/SiN$). To reduce the substrate's C contribution, the backside of the chip is thinned using a wet etching process with potassium hydroxide (KOH). The SiN layer is unaffected by KOH, so it remains intact except where it is selectively removed using reactive ion etching (RIE) with SF_6 gas, creating a $4 \times 4mm$ window. Dipping the chip in KOH results in a thinned square $4 \times 4mm$ window on the backside of the chip (see Fig. 3.1). This thinned window, the 'membrane,' serves as the active part of the calorimeter cell (CC).

During the KOH etching, the membrane's thickness is estimated by its color, aiming for a yellow-orange hue, corresponding to $15 - 25\mu m$ thick membrane.

Leads

The SiN on the front side of the sensor is removed and covered with a $100nm$ thick superconducting niobium-titanium ($NbTi$) layer, topped by a $30nm$ gold (Au) layer that protects it from oxidation. Eight thin wires (can be seen in Fig. 3.2(a)) are defined from the Au layer using a photolithography process followed by wet etching to remove the residues (KI for the Au

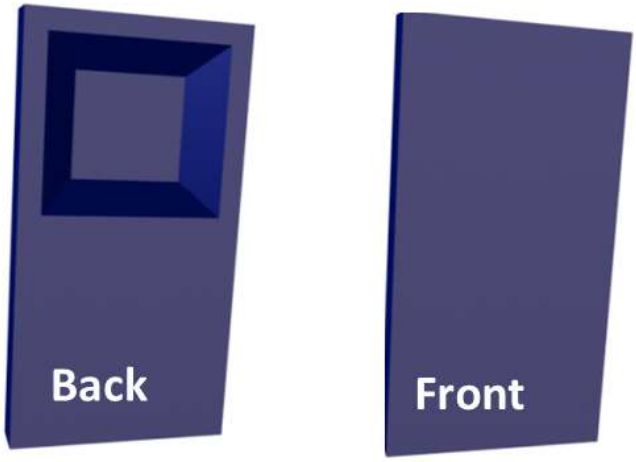

Figure 3.1: Back and front side of the CC. The back side of the sensor is thinned to reduce the substrate's contribution.

layer, $HNO_3 + HF$ for the $NbTi$). These eight wires serve as electrical leads for the different components of the sensor as well as mechanical support for the membrane.

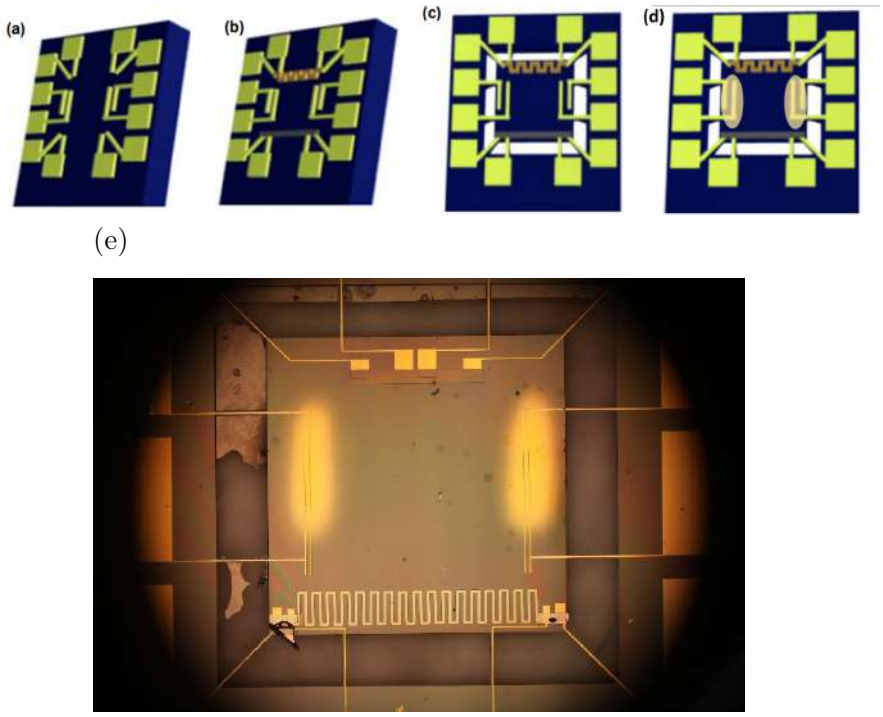

Figure 3.2: The CC. *Top*: The different fabrication steps (a) The thinned part with Au leads (b) After Cu heater and NbN thermometer fabrication (c) The thinned part of the CC separated from the bulk, after the additional etching step (d) Ready CC, after Ti/Au deposition on the sample's leads, using a mechanical mask. *Bottom*: Optical-microscope image of the complete CC.

Heater and Thermometer

To measure C, one needs to supply heat to the system and measure the change in its temperature. A heater and a thermometer are defined on the thinned membrane using photolithography and lift-off processes. Heat is supplied by a $200nm$ thick copper (Cu) meander (the heater), and the temperature change is measured through the resistance of a $80nm$ thick niobium-nitride (NbN) slab (the thermometer). Both components are shown in Fig. 3.2(b).

The thermometer is plasma deposited, with deposition parameters chosen to ensure its resistance is highly sensitive to small temperature changes at low temperatures, specifically within the superconductor T_c range. This sensitivity determines the thermometer quality, defined as α: $\alpha = \frac{-1}{R_{Thermometer}} \cdot \frac{dR_{Thermometer}}{dT}$. A higher α allows for the detection of smaller changes in δT, enabling a higher signal for the C_P measurement. α at low T is estimated by the resistivity ratio (RR) between the thermometer resistance at room temperature and at liquid nitrogen temperature: $RR = \frac{R_{77K}}{R_{300K}}$. To achieve the optimal α, the target RR is approximately 4. Repeated experimentation suggests that this RR value can be achieved by using a $\frac{4}{14}$ nitrogen to argon gas mixture ratio and a power source frequency of $275KHz(\pm 5Hz)$ during the NbN deposition. To ensure a sensitive thermometer, the RR is checked at least four times on demi-sapphires before the thermometer is deposited on the actual CC. This results in a sensitive thermometer

operating within the desired temperature range of a few kelvins. A characteristic $R(T)$ curve of the thermometer used in our experiment is presented in Fig. 3.3.

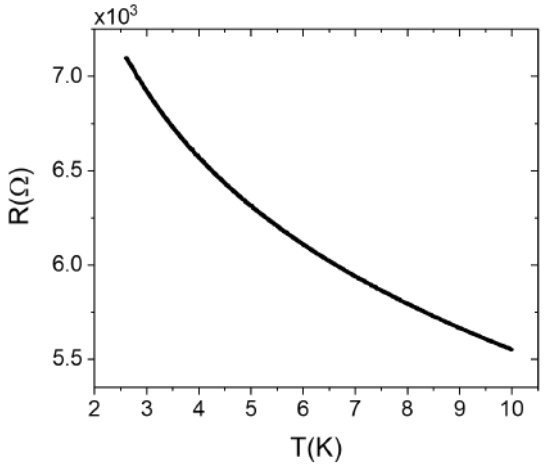

Figure 3.3: $R(T)$ curve of a NbN thermometer used in our experiment, with $\alpha = 0.0715$ at $T = 2.7K$.

Thermal Separation of the CC

With the leads, heater, and thermometer already fabricated in the CC, another photolithography step is performed to isolate the active part of the CC from the thermal bath of the bulk. $1240\mu m$ thin bridges are defined, that will support the active CC and carry the $NbTi$ wires. An RIE process with SF_6 gas is used to etch all the silicon around the thinned part, leaving it suspended on these 12 thin bridges, and thermally disconnected from the bulk (Fig.3.2(c)).

To allow transport measurements of the nano sample, a bilayer of $5nm$ titanium (Ti) and $200nm$ Au is deposited using a mechanical mask on the sample's transport leads, located on both sides of the CC (Fig.3.2(d)).

Mounting and Connecting the CC

Once a workable CC is achieved, it is mounted on a Cu sample holder. The sample holder has a heater and a calibrated thermometer on its backside, used to control the sample's temperature during the experiment. The sensor's contacts are connected to the holder pads using a micro-bonder, as shown in Fig. 3.4(b). After placing and connecting the sensor to the holder, we ensure that the sensor and its different components (heater, thermometer, sample leads) are not shorted to ground nor between themselves.

A mechanical mask is placed over the sensor, covering the entire CC and its holder, except for a single window that exposes a rectangle between the sample's transport leads (Fig.3.4(b)). This allows the deposition of our desired ultra-thin layers on-top of the suspended membrane, using the "quench condensation" technique as described in the following paragraph.

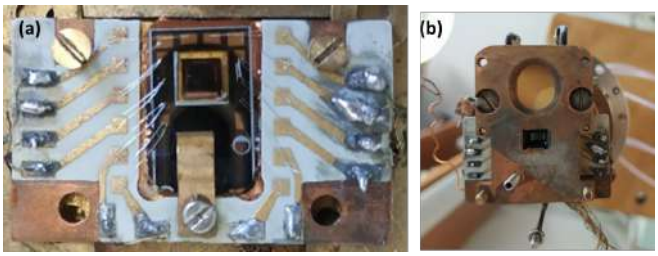

Figure 3.4: Mounting the sensor (a) The CC on a Cu holder with micro-bonded contacts (b) The sensor under the mechanical mask. Only the quartz-crystal and the window between the samples' leads can be seen through it.

3.1.2 Quench Condensation

In this method, a thin layer is thermally evaporated *in situ* under UHV conditions and at liquid helium temperature. The significant advantage of the technique is that a single sample can be studied throughout the entire SIT, without the need to open the system, breaking the UHV conditions and exposing the sample to the air, which can harm it. We used the quench condensation (QC) technique to create the ultra thin layers that were studied in our C experiments.

For each experiment, three thermal evaporation boats with desired material grains were used. The boats were connected to the probe after they were pre-melted (see Fig. 3.5(a)). The prob was designed so that the evaporation boats were located directly under the sample (and the thickness monitor quartz crystal) area, to allow direct evaporation.

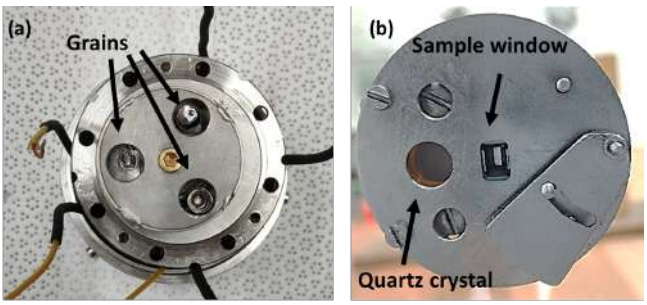

Figure 3.5: Quench condensation setup (a) Three evaporation boats loaded with pre-melted grains (b) The quartz crystal and CC behind the mechanical mask. When the shutter is open, only the sample area is exposed to the evaporation.

As the sample was mounted to the probe, a second mechanical mask was placed to assure that only the desired area on the cc and the quartz crystal were exposed to evaporation (Fig.3.5(b)). A shutter and the quartz crystal were used to control the evaporation rate. When the required thickness was achieved (as measured by the quartz crystal and by the sample's resistance), the deposition was terminated and $R(T)$ and $C(T)$ measurements were taken. Sequential evaporations and measurements were then performed, while maintaining the sample at cryogenic temperatures and under UHV conditions.

3.1.3 Measurement Protocol

The heat capacity is measured using the second harmonic '2ω' ac calorimetric technique [48–51]. In this technique, an alternative current at frequency ω is generated to the heater using a Lock-in amplifier (LIA) as a source: $I = I_0 cos(\omega t)$. This results in a heating power at frequency of 2ω:

$$P_{\text{Heating}} = I^2 R_{\text{Heater}} = P_0 \left(1 + \cos(2\omega t)\right). \tag{3.1}$$

Where $P_0 = \frac{I_0^2 * R_{Heater}}{2}$. Consequently, the temperature change, δT_{ac}, in the thermometer oscillates at 2ω and is measured by applying a small dc current (I_{dc}) to the thermometer and measuring the ac voltage (V_{ac}) drop on it using a LIA at the second harmonic (thus, V_{ac} is referred to as V_{2f} in some contexts):

$$\delta T_{ac}(T) = \frac{V_{ac}(T)}{\alpha R_{th}(T) I_{dc}} \tag{3.2}$$

Choosing the right working frequency (f) is extremely important. It is selected by scanning the frequencies range and identifying the *"adiabatic plateau"*, where the f is smaller than the thermalization time of the heat-bath (to prevent heat 'leak', loss, to the surroundings, which would result in signal loss), but larger than the diffusion time in the membrane. This is done at three different temperatures (see Fig. 3.6) to ensure that the chosen working frequency falls within the *plateau* across the entire temperature range of the experiment. At this limit, the term for the C can be written as:

$$C = \frac{P_{Heating}}{2\pi f \delta T_{ac}} \tag{3.3}$$

Where $P_{Heating}$ is calculated from Eq.3.1, as R_{Heater} and I_0 are both known. f is the chosen working frequency, and δT_{ac} is the temperature oscillation of the thermometer measured by the LIA.

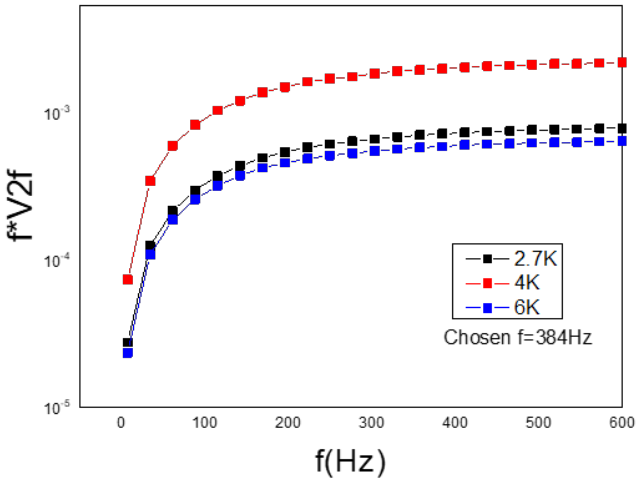

Figure 3.6: Frequency scan at three different temperatures to find the adiabatic plateau and choose the working frequency. The plateau is where $f_d << f << f_b$ where f_d is the frequency matches the diffusion time in the membrane, and f_b is the frequency matches to the bath thermalization time. Between these two values the V_{2f} signal is maximal.

As the system reaches based temperature, each experiment begins with a few calibration steps: (1) Calibration of the thermometer, where its resistance ($R(T)$) is measured and the temperature coefficient (α) is calculated. (2) Determining the working frequency, as previously explained. (3) Maximizing the V_{2f} signal. This is achieved by measuring the signal at three different temperatures and adjusting the heating power and I_{dc} on the thermometer to ensure the V_{2f} signal is at its maximal value without overheating the heater or the thermometer. After these calibration steps, the heat capacity of the bare sensor, C_{sensor}, which includes its heater, thermometer, and contacts, is measured. This measurement has a dual purpose. First, to validate that we indeed measure the heat capacity. This is confirmed by the behavior of the reduced heat capacity of the sensor ($C_{sensor}T$), that should match this linear behavior when plotted against T^2, given by:

$$\frac{C}{T} = \gamma + \beta T^2 \tag{3.4}$$

Secondly, the $C_{sensor}(T)$ measurement serves as a baseline to be subtracted from subsequent measurements of the thin films. This allows us to isolate the heat capacity of the thin films *solely*. Measurement of the $C_{sensor}(T)$ curve for a bare CC sensor is shown in Fig. 3.7.

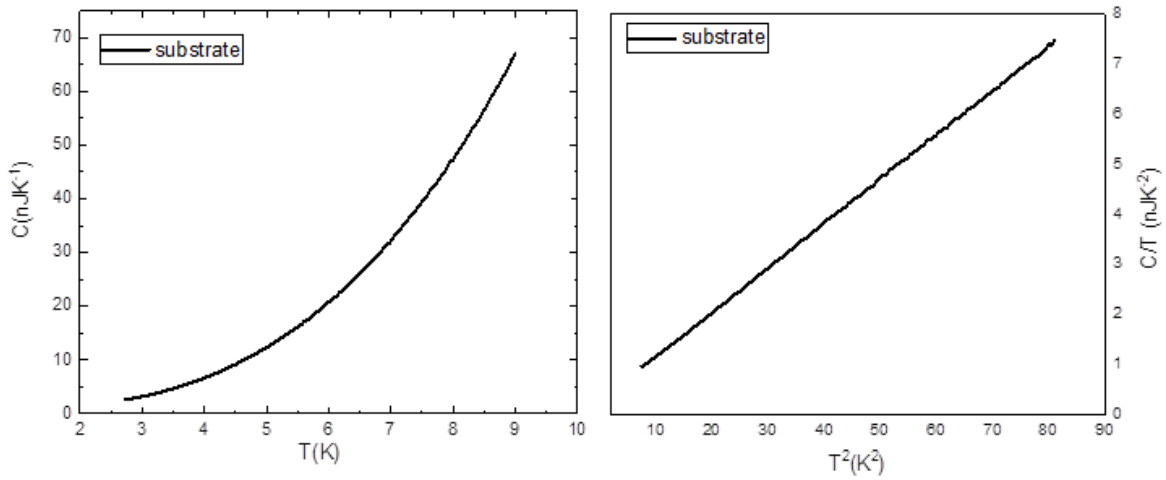

Figure 3.7: Left: Measurement of C_{sensor} that was used for the Indium experiment. Right: $C_{sensor}T(T^2)$ of the same sensor. The linear behaviour of the curve follows Eq.3.4, confirming the sensor's suitability for heat capacity measurements. This linear curve serves as a baseline and will be subtracted from subsequent measurements of the thin films.

Subsequently, we incrementally quench condensed thin layers of the desired material onto the CC. Measurements of $C(T)$ and $R(T)$ are taken at each deposition step. To convert from C to the intrinsic property of C_p, each C measurement is divided by the deposited layer mass, extracted from the frequency change at the quartz crystal.

Fig. 3.8 shows a picture of a measured device after the completion of the experiment. The suspended membrane displays the various components: the heater meander at the bottom of the picture, the thermometer at the top, and a stack of 21 In layers in the center.

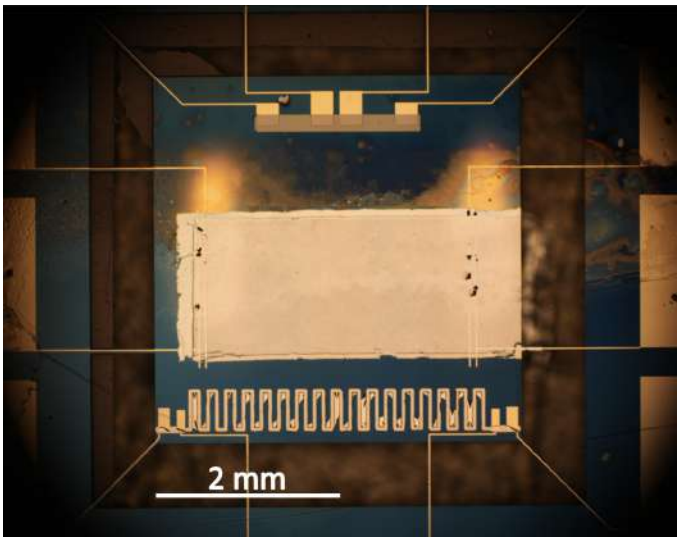

Figure 3.8: The sensor utilized for the In experiment, at the end of the experiment. The 21 In layers can be seen in the middle of the sensor, positioned between the heater at the bottom and the thermometer at the top.

3.2 Transport Measurements of SLG/SC-Dots Bilayer Devices

3.2.1 Sample Fabrication

In this section, the fabrication of ordered InO nano-dots arrays fabricated on top of a monolayer graphene substrate will be described. Before detailing the fabrication process of the SC dots, we first describe the fabrication of the SLG substrate. In our study, we employed both exfoliated SLG flakes and CVD films. Exfoliated SLG flakes are preferable due to their uniformity and single-crystal nature. In contrast, while CVD-grown SLG films can cover large areas, they potentially include polycrystalline domains that may introduce disorder, leading to smearing of the Dirac point (DP). However, using CVD SLG offers significant advantages in terms of scalability and saves valuable time in the fabrication process by eliminating the need for in-house exfoliation.

SLG Flakes

To achieve **SLG flakes**, we start from graphite that is thinned into graphene through exfoliation. Typically, after multiple exfoliation steps, monolayers are achieved and deposited on a Si/SiO_2 substrate with pre-prepared gold alignment marks. The alignment marks are essential for ensuring precision throughout the fabrication process. We use blue scotch tape to thin the graphite until an SLG flake is obtained (see scheme 3.9). Such tape is commonly used for this purpose.

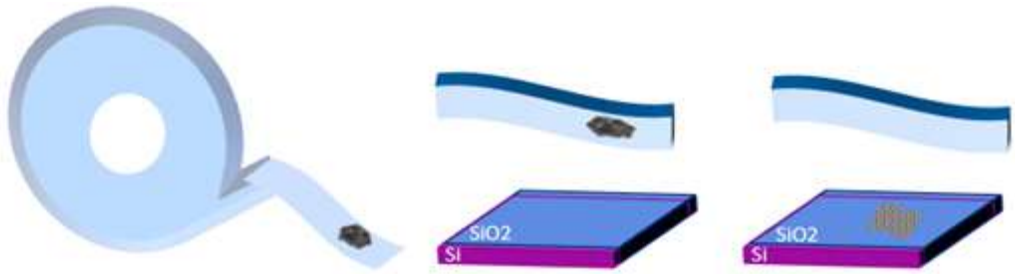

Figure 3.9: Scheme of the exfoliation steps. The graphite is exfoliated using adhesive blue tape. After several exfoliations, when an SLG flake appears to be obtained, it is deposited on the Si/SiO_2 wafer.

After transferring the flakes on the wafer, the sample is examined visually under an optical microscope to identify SLG flakes. Once potential SLG flakes are identified, their 'identity' is confirmed using RAMAN spectroscopy. The RAMAN signal of SLG flakes exhibits (mainly) two peaks (a $2D$ and a G bands peaks) [52]. By analyzing the shapes and relative intensity ratio of these peaks, one can determine the quality of the graphene and confirm that it is indeed a single layer. High-quality SLG exhibits a sharp $2D$ peak with an amplitude twice that of the G band. A RAMAN scan of one of our measured SLG samples is shown in Fig. 3.10.

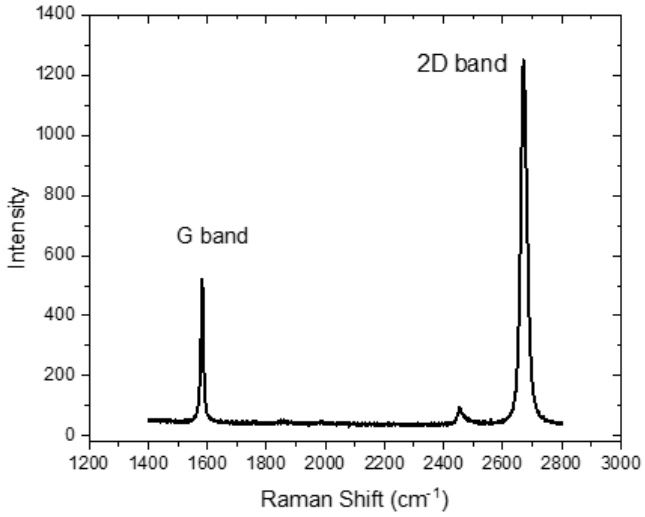

Figure 3.10: Raman spectra of one of the measured SLG samples. The 2D band peak is sharp, and the ratio between the peaks is ~ 2, confirming that it is indeed a high-quality SLG flake.

For **CVD-grown SLG**, we used commercially purchased SLG that was grown and transferred onto a doped $Si/300nm\ SiO_2$ wafer by *Graphenea* company. The subsequent fabrication steps are similar for both exfoliated single-layer graphene and CVD-grown SLG.

Annealing and Etching

The SLG chip undergoes annealing in a furnace to remove impurities and defects, enhancing its purity and uniformity. The annealing process lasts for 4 hours at $350°C$ under an argon atmosphere. Subsequently, the SLG is shaped into the desired geometry using photolithography

followed by SF_6 plasma etching. In this work, we investigate SC/SLG bilayer devices in both 1D (single SC dot row) and 2D (SC dot matrix) geometries. Accordingly, the SLGs are etched into rectangular shapes with dimensions of $1\mu m$ width and $18\mu m$ length for 1D devices. For 2D devices, the geometries vary, with the largest matrix being $60 \times 20\mu m$. Examples of these devices, after the etching step, are shown in Fig. 3.11 panels a_1 and b_1.

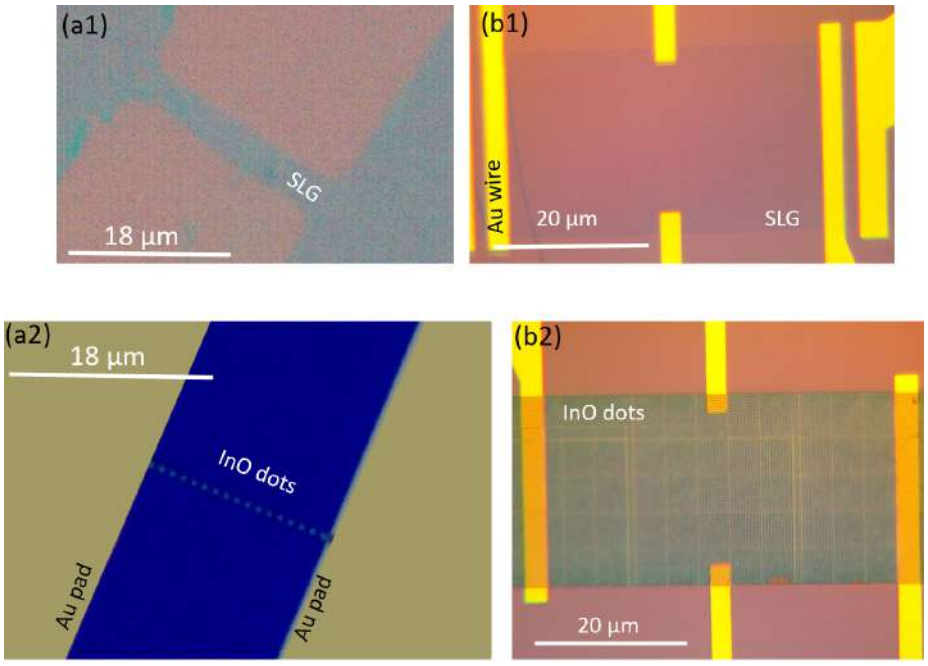

Figure 3.11: Fabrication steps of 1D dot row (a1,a2) and 2D dot matrix (b1,b2). The bare SLG after it was etched to the desired dimensions of $1\mu m$ narrow line (a1) and rectangle of $60 \times 20\mu m$ with gold Hall-probe configuration (b2). (a2,b2) With SC InO dots arrays. The dots are $1\mu m$ in diameter with $1.2\mu m$ center-to-center distance.

Contacts Fabrication

Four-terminal gold contacts are defined on the SLG using e-beam lithography. The leads are custom-designed using an $AutoCAD$ program tailored to each SLG's surroundings and geometry. The gold alignment marks on the wafer aid in precisely aligning the contacts on the SLG. Contacts consist of $4/50nm$ Cr/Au layers, deposited by e-beam and thermal sputtering, respectively. An additional electrode is defined on the backside of the devices to facilitate gating.

Dots Fabrication

Similar processes of lithography followed by deposition are used to create the SC dot patterns on the samples. The dots were designed with a diameter of $1\mu m$ and an inter-dot distance of $200nm$. These parameters were consistently used in all our devices, both 1D and 2D dot arrays, to ensure comparability.

The main challenge during the e-beam lithography step is achieving precise alignment of the design on the SLG, especially for the 1D devices since both have a width of $1\mu m$. This

alignment is accomplished using pre-prepared Au alignment marks on the wafer. Examples of SC dot devices are shown in Fig. 3.11(b_1, b_2).

After e-beam lithography, the sample is placed in the deposition chamber for evaporation of the desired superconducting material, amorphous indium oxide (InO) in our case.

3.2.2 InO

InO was chosen for our graphene-based devices experiments for two primary reasons. Firstly, it is a weak SC characterized by a low carrier density (n), which can be controlled by adjusting the partial pressure of O_2 during deposition, resulting in a range of carrier densities between 10^{19} and 10^{21}cm^{-3}. By adjusting n, both insulating and superconducting InO films can be fabricated [19, 53–56]. In our experiment, InO was evaporated at O_2 partial pressure environments of 8×10^{-6} and $1 \times 10^{-5} mbar$. $O_2^{Pressure} < 8 \times 10^{-6} mbar$ resulted in superconducting samples, while $8 \times 10^{-6} < O_2^{Pressure}$ resulted in insulating samples. An $O_2^{Pressure}$ of $1 \times 10^{-5} mbar$ resulted in samples that are close to the SIT.

Secondly, InO was chosen since its level of disorder can be tuned through thermal annealing. Annealing the sample on a hot plate up to $80 \circ c$ releases oxygen impurities without affecting its amorphous structure [54, 56]. This process lowers the sample's resistance, pushing it towards the superconducting phase. By starting with an insulating InO sample and annealing it, the entire SIT can be observed using the very same sample. The SIT driven disorder of InO samples was shown before, as in the work of Roy et al. [56] and can be seen in Fig. 3.12.

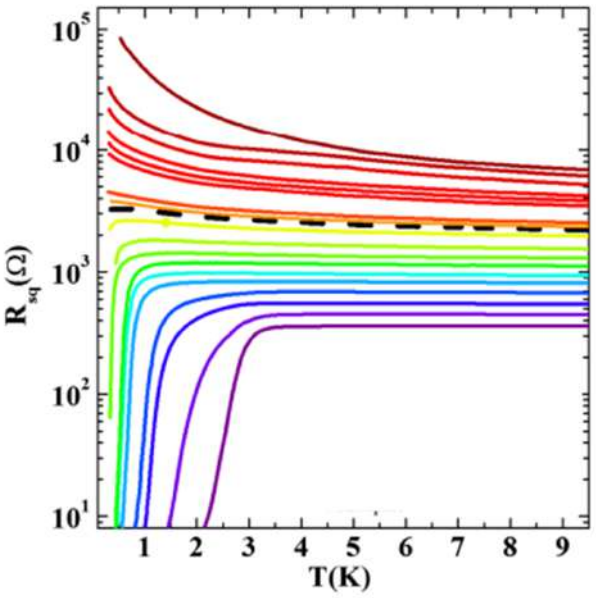

Figure 3.12: Adjusted from [56]. $R(T)$ curves of the same sample at different annealing stages. The sample transitions from being an insulator (high R at low Ts) to a SC (low R at low Ts) as it was thermally annealed.

InO was e-beam evaporated, using 99.999% pure ($N5$) In_2O_3 pieces. The base pressure in

the vacuum chamber was no more than $1.5e-6$ mbar. The deposition was carried out at $8e-6$ or $1e-5$ mbar oxygen partial pressure, with pure O_2 gas was introduced into the vacuum chamber controlled by a needle valve. $50nm$ of InO were deposited, at rate of $0.5-1\frac{\text{Å}}{S}$.

3.2.3 Set up and Measurement Protocol

The device is fixed to a PVC sample holder, with a gold plate at its center (see Fig. 3.13), using silver-paint. Cu wires are attached from the device to different gold pads on the holder.

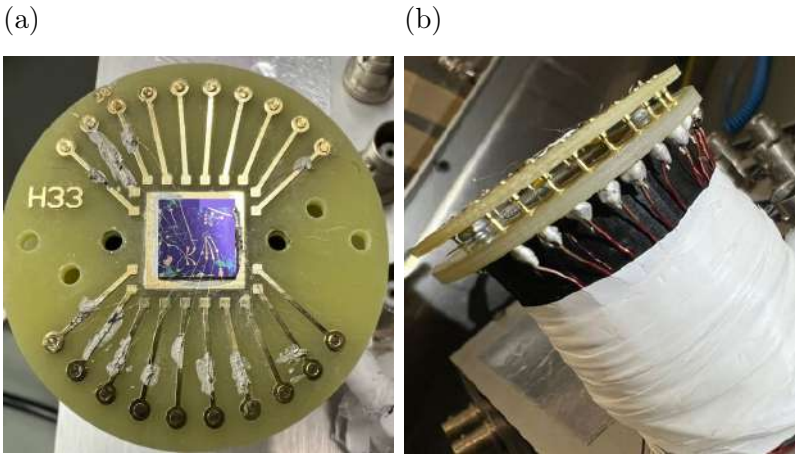

Figure 3.13: The sample holder from (a) top view and (b) side view. The holder includes a centered gold plate used as a back plate, along with Au pads and pins for electric feed-through from the sample. A sample with three devices is attached at the center using silver paint, which is visible in the image.

The carrier density of the graphene is controlled by applying a gate voltage to the back side of the Si wafer; the gold layer on the holder acts as one metallic plate of the capacitor, the graphene acts as the second metallic plate, and the SiO_2 serves as the dielectric material between them. One of the contacts on the device is used as a second gate electrode. The resistance of the device is measured while varying the gate voltage, obtaining $R(V_g)$ curves. A schematic of the measurement setup is shown in Fig. 3.14. It is important to note that the voltage source used to gate the graphene also monitors the leakage current. We carefully watch the leakage current to ensure it is not too high. Applying a voltage that is too high will break the gate, which manifests as a jump in the leakage current. Typically, our $285nm$ SiO_2 layer can hold up to $120V$.

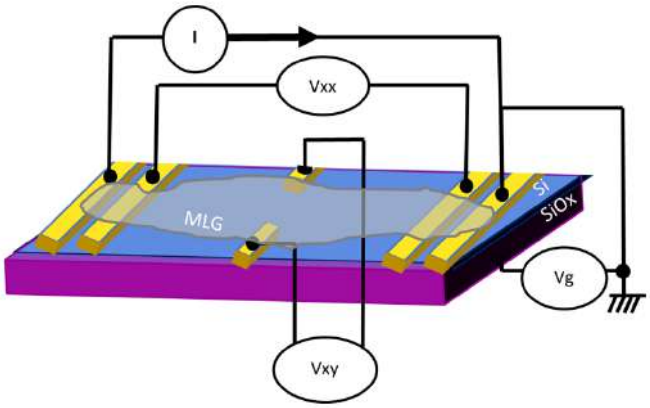

Figure 3.14: Sketch of the measurement setup.

We measured $R_{xx}(V_g)$ (SLG carrier density) and the differential conductance ($\frac{dI}{dV}$) as a function of the source-drain voltage. These measurements were carried out for different temperatures ($300mK - 20K$) and magnetic fields ($0 - 9T$) in two different He^3 cryostats.

Chapter 4

Results and Discussion

In this chapter, we present a comprehensive summary of our results, emphasizing the key observations that have arisen from our work. Following this, we engage in analysis and discussion. This chapter is divided into two sections, each focusing on the different measurement used to tackle the research goals. The first section delves into thermodynamic measurements of C_p, and the second section examines the findings of transport measurements on arrays of NS junctions.

4.1 Specific heat measurements of Ultra-thin layers of indium

Our C_p experiments were designed to address a key question related to the SIT. We aimed to elucidate the nature of the bosonic phases emerging during the SIT, with a particular focus on the potential existence of the BM phase. If this phase exists, its presence should be detected by C_p measurements.

A complementary C_p study on a normal metal, Ag, undergoing an insulator-to-metal transition (MIT) is presented in the Appendix (A). This study provides additional context and comparative baseline data, enhancing our understanding of the thermodynamic behavior of disordered systems.

Ultra-thin layers of In were quench condensed onto the membrane, and simultaneous measurements of resistance and heat capacity were preformed at each evaporation step to detect the BM state during the SIT. A total of 21 steps were measured, with layer thicknesses starting from sub-nanometer and gradually increasing to $230nm$, as detailed in Table 4.1.

Step number	Mass (gr)	Thickness (nm)	β (JK^{-4})
1	2.67143E-8	0.71429	NA
2	6.50048E-8	1.7381	3.57008E-5
3	9.17191E-8	2.45238	3.91862E-6
4	1.45148E-7	3.88095	5.33863E-6
5	2.07481E-7	5.54762	6.32858E-6
6	2.71595E-7	7.26191	4.78089E-6
7	3.21907E-7	8.60714	3.92895E-6
8	4.30545E-7	11.5119	6.76804E-6
9	5.10688E-7	13.65476	NA
10	5.5076E-7	14.72619	NA
11	5.8905E-7	15.75	NA
12	6.36245E-7	17.0119	NA
13	6.8166E-7	18.22619	NA
14	7.35088E-7	19.65476	4.61599E-6
15	8.20574E-7	21.94048	5.42887E-6
16	1.88647E-6	50.44048	9.33696E-6
17	2.88647E-6	77.17844	1.09542E-5
18	4.97018E-6	132.89261	1.14472E-5
19	5.80278E-6	155.15451	1.31258E-5
20	7.58373E-6	202.7735	1.1821E-5
21	8.57127E-6	229.17826	1.38598E-5

Table 4.1: Table of the mass, thickness and β values of the varied In layers.

The $R(T)$ measurements indicate that the system undergoes the SIT, transitioning from an insulating phase (thinner layers, Fig. 4.1(a)) to a superconducting phase (thicker layers, Fig. 4.1(e)). In the intermediate layers, the $R(T)$ measurements show resistance saturation at low temperatures (Fig.4.1(c)), indicating the presence of an anomalous metallic state. To provide a clearer understanding of the behavior of the specific heat, we present the plot of $\frac{C_p}{T}$ vs T^2 (Eq.3.4), referred to as the **reduced** C_p, in the right column of Fig. 4.1. The reduced C_p measurements are divided into three panels based on the observed characteristics of their $R(T)$.

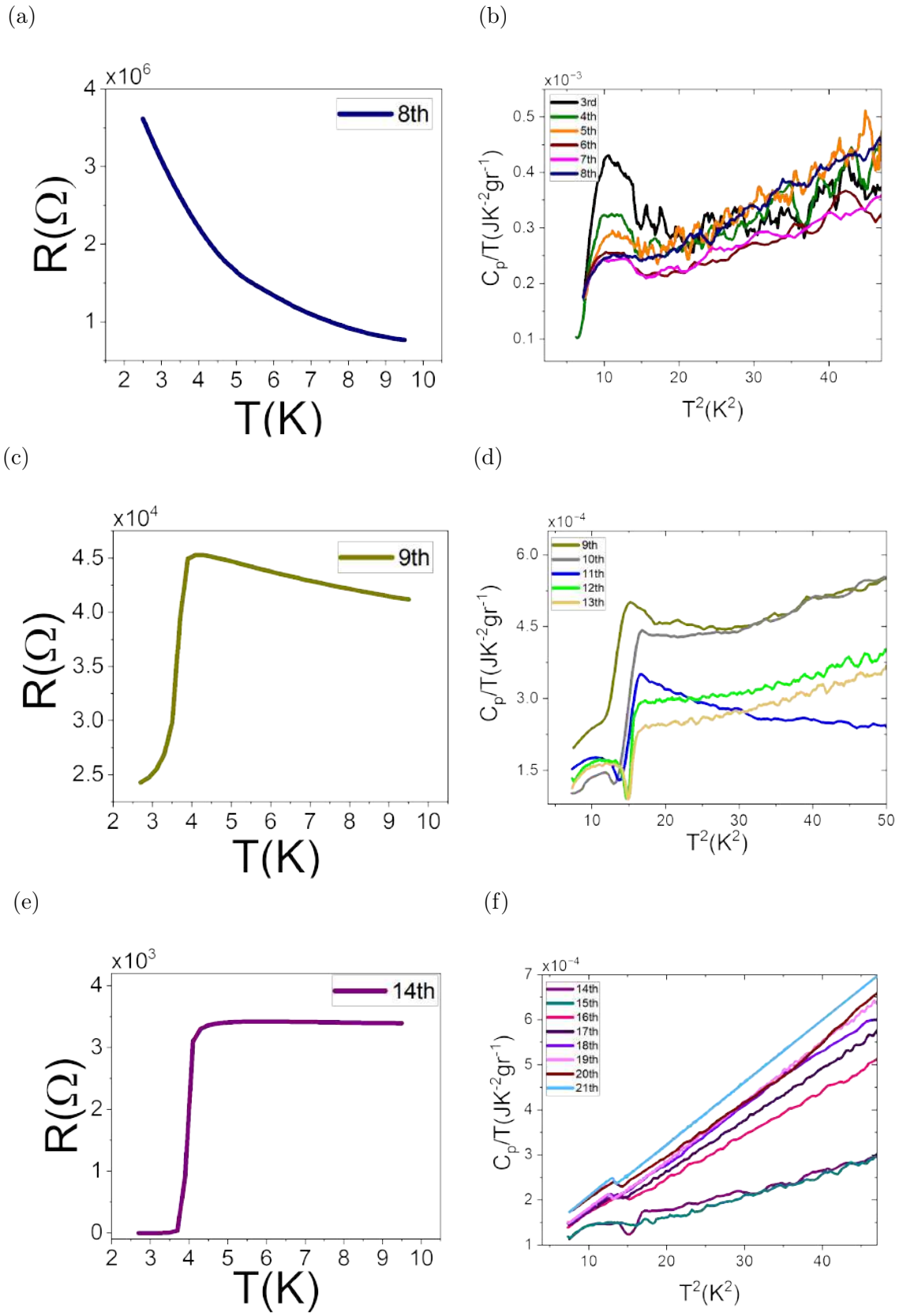

Figure 4.1: Representative $R(T)$ curves of films in each phase category (left column) and the reduced specific heat, $\frac{C_p}{T}$ vs T^2 of the various steps (right column), categorized into three regions according to their $R(T)$ curves. Different C_p structures are observed in each category: (a) $R(T)$ and (b) $\frac{C_p}{T}$ vs T^2 for thinner layers (2-8), (c) $R(T)$ and (d) $\frac{C_p}{T}$ vs T^2 for intermediate layers (9-13), and (e) $R(T)$ and (f) $\frac{C_p}{T}$ vs T^2 for thicker layers (14-21).

The C_p data reveal three distinct structures at various layer thicknesses, which we associate with the different phases of the system during the SIT, accordingly:

1. Thinner layers (2-8, insulating $R(T)$s): These layers showed a smeared peak around a temperature of $T = 3.8K$ (Fig. 4.1(a,b)), with the peak amplitude decreasing as the layer thickness increases

2. Intermediate layers (9-13, BM region in the $R(T)$s): These layers exhibited a smeared peak, followed by a subsequent *second* feature (Fig. 4.1(c,d)) around the same temperature of $T \approx 3.8K$.

3. Thicker layers (14-21, SC $R(T)$s): Layers 16-21 displayed a sharp jump at a well-defined temperature of $T \approx 3.6K$. Stages 14 and 15, while showing superconducting behavior in $R(T)$, had C_p signatures resembling those of intermediate (stage 14) or thinner (stage 15) layers (Fig. 4.1(e,f)).

We defined T_c from the C_p measurements as the temperature at which the reduced C_p curves return to the linear curve of the normal state C_p/T versus T^2 in both insulating and superconducting films. For the insulating films, this temperature is $T \approx 3.8K$, while for the SC films, it is slightly lower at $T \approx 3.6K$. These T_c values are somewhat higher than the bulk T_c in In ($3.4K$), and it seems that as the layer thickness increases, T_c gradually approaches the bulk T_c value. Previous studies on thin quench-condensed superconducting layers [35, 57] have reported similar findings, indicating that the T_c of thin layers may exceed that of the bulk material. Regardless of the layer's phase— whether insulating or superconducting— a distinct feature in C_p was observed, at the layer's T_c, indicating the transition of In nanograins to a superconducting state. The deposited In forms a granular film (since there was no adhesion layer deposited). Consequently, as each In nanograin transitions to a superconducting state, a discontinuity in C_p occurs. These findings are consistent with the bosonic model of the SIT, where the C_p jump in the insulating phase serves as a distinctive marker for the existence of a Bose insulator phase, as discussed earlier in the Introduction (1.4).

According to BCS theory, the ratio $\frac{\Delta C_p}{C_n} = 1.43$ [58], where ΔC_p is the C_p signal at T_c and C_n is the normal phase C_p at the same temperature.

For bulk In, $C_n = 0.821\frac{mJ}{Kgr}$ at $T \approx 3.8K$ and $C_n = 0.7\frac{mJ}{Kgr}$ at $T \approx 3.6K$ [59]. The ratio $\frac{\Delta C_p}{C_n}$ for the different layers, at their respective T_c values, is shown in Fig. 4.2. The ratio is higher for thinner layers and initially decreases as the thickness increases. For thicker layers, the ratio begins to rise with increasing thickness, getting closer to the theoretical value of 1.43, indicated by the red line in the figure. Our thickest film (21st step), which is closest to bulk behavior, exhibiting a ratio of ≈ 1.3, which is in good agreement with the theoretical prediction. The gray area in the figure represents intermediate layer thicknesses, where this ratio analysis does not apply due to fundamentally different behavior occurring in this region. This trend, where thinner films exhibit higher peak amplitudes, is consistent with previous findings in quench-condensed Pb [35] (see Fig. 1.9(c)).

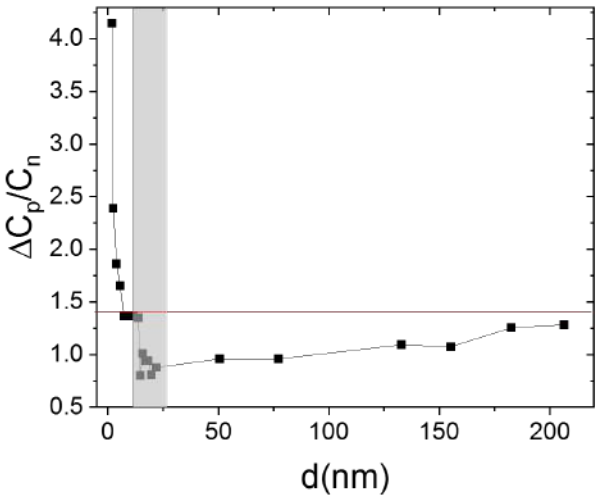

Figure 4.2: $\frac{\Delta C_p}{C_n}$ at T_c as a function of layer thickness. Thinner layers exhibit the highest ratios, which initially decrease as the thickness increases. For the thicker layers, the ratio begins to increase again, with the thickest film (21st step) reaching approximately 1.3, approaching the theoretical BCS value of 1.43 (indicated by the red line). The gray-shaded region covers the intermediate layer thicknesses, where the ratio analysis is not applicable due to a fundamentally different behavior occurring in this region.

While the behavior of the T_c signature in the thinner and thicker layers is consistent with previous experiments [35], the occurrence of a prominent secondary C_p feature observed in the intermediate thicknesses is a novel discovery. To the best of our knowledge, this phenomenon has not been documented in previous experiments or addressed theoretically.

In the intermediate-metallic stages, after exhibiting a smeared peak similar to those observed in the thinner layers, the reduced C_p signal does not return to the normal state $\frac{C_p}{T}$ behavior, which is linear with respect to T^2. Instead, at T_c, it exhibits a sharp increase to a value higher than the expected phononic contribution. Moreover, after this sharp jump the C_p/T signal remain relatively flat and constant at higher temperatures. Based on equation 3.4, the slope represents β, the phonon coefficient. The nearly flat and constant signal relative to T^2 is misleading and suggests minimal phonon contribution at these stages, implying that other effects are dominating the behavior. This includes the existence and persistence of additional states or fluctuations introduced into the system during these stages.

Examining the *amplitudes* of the two features in the intermediate layers reveals an interesting pattern: the amplitudes of the two features exhibit opposite trends. Specifically, as the amplitude of the first peak increases with layer thickness, the amplitude of the second sharp jump decreases (and vice versa between the 9th and 10th steps). This trend is illustrated in Fig. 4.3, where the amplitudes were calculated after subtracting the phononic contribution from each curve using linear fits. In the figure, the first peak amplitude is shown in black, while the second feature amplitude is shown in red. The opposite trends might indicate a potential interplay between the two features.

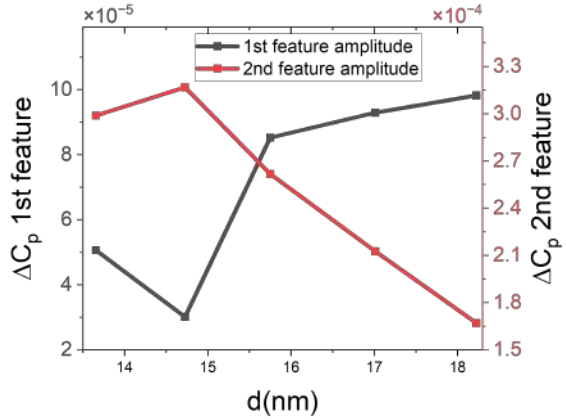

Figure 4.3: Amplitudes of the two features observed in intermediate layers, exhibiting opposites trends. As the amplitude of the first feature (black) increases with layer thickness, the amplitude of the second feature decreases.

For further understanding of this unique C_p signature, we calculated the entropy, S, of the system for each of the 21 steps by integrating $\frac{C_p}{T}$ vs. T in small temperature intervals of $1mK$ from base temperature up to $5K$. The resulting S is plotted against the film thickness in Fig. 4.4(a). It is evident that the entropy initially decreases, but then peaks before decreasing again. Intriguingly, the entropy peaks at the 9th step with a "critical thickness" of $13.65nm$, which is the first layer to exhibit metallic behavior at low temperatures (its $R(T)$ curve is shown in Fig. 4.1(c)) and to display a second feature in C_p, presumably resulting in this excess entropy.

(a) (b)

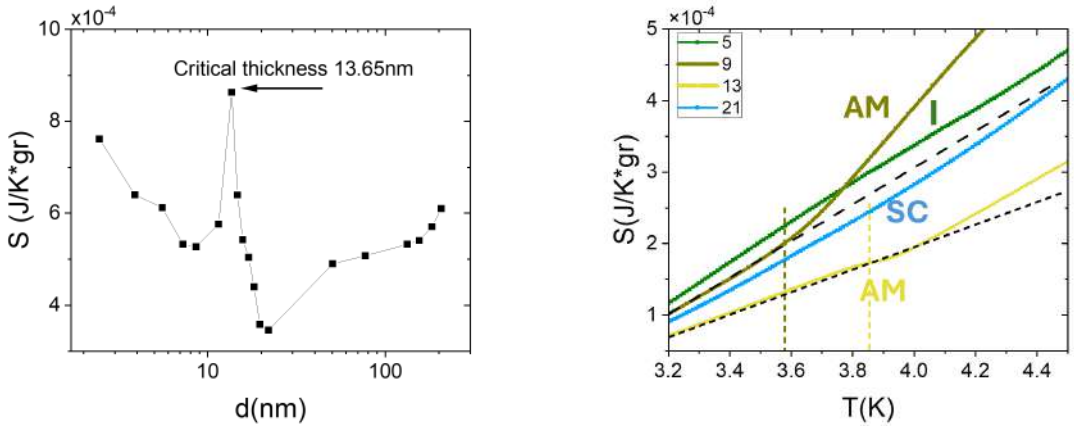

Figure 4.4: The entropy, S, of the system at different stages. (a) S vs. the film's thickness, d, calculated up to $5K$. A sharp peak can be observed at the 9th step, marked as the "critical thickness". (b) Detailed plot of S in temperature intervals of $1mK$ for selected layers: a thin layer (5th) exhibiting a "normal" S behavior, layers of intermediate thicknesses (9, 13) showing anomalies in the S behavior, and S of the thickest layer (21) exhibiting "normal" S behavior again. The black dashed linear lines serve as guides to the eye, aiding in identifying the temperature at which the slope deviates.

Figure.4.4(b) presents the entropy as a function of temperature for selected experimental stages. Notably, there is a change in the slope of the $S(T)$ curve between the 9th and 13th steps. This change in slope isn't observed for the 5th (thinner layer) or the 21st layer (thickest one), but only for the intermediate layers, at temperatures ranging between $3.56K$ and $3.85K$. Consequently, this change in slope leads to the generation of excess entropy (Fig.4.4(a)).

In addition to the second dominant feature in C_p, which directly impacts the entropy signature at these intermediate layers, we observed another unique characteristic at these thicknesses: a shift in the dominant heat carrier type, which will be discussed next.

Information about the dominant heat carriers can be obtained from Eq.3.4, where β is the coefficient associated with the phononic contribution to heat transport in the system. Therefore, the value of β reflects the extent to which phonons are dominate as heat carriers. β values were extracted from the data (Fig.4.1) and plotted against the layer thickness (d) in Fig. 4.5(a). The plot shows a generally linear trend, consistent with previous experimental observations [35]. However, at intermediate thicknesses, where the C_p/T signal is particularly high and remains relatively constant with T^2, the true β values become obscured. At these stages, the high signal effectively buries β, resulting in calculated values that appear extremely small.

Equation 1.1 offers additional insights into the predominant heat carriers of C_p through the analysis of the slopes (m) of the C_p curves on a log-log scale ($\log(C_p)$ versus $\log(T)$ curves), $m = \frac{dlog(C_p)}{dlog(T)}$. A slope of 1 would suggest dominance by electrons, while a slope of 3 would indicate dominance by phonons. In Fig. 4.5(b), the extracted m values are shown vs. the thickness, d. Initially, m is approximately 3, indicating phonon dominance. However, for thinner to intermediate layers, it decreases to a value between $\sim 1.5 - 2.3$, indicating that electrons also become significant heat carriers. While both electrons and phonons always contribute to heat transport, the dominant carrier type shifts. This slope of approximately 3 is restored for the thicker layers, where phonons once again predominantly govern heat transport.

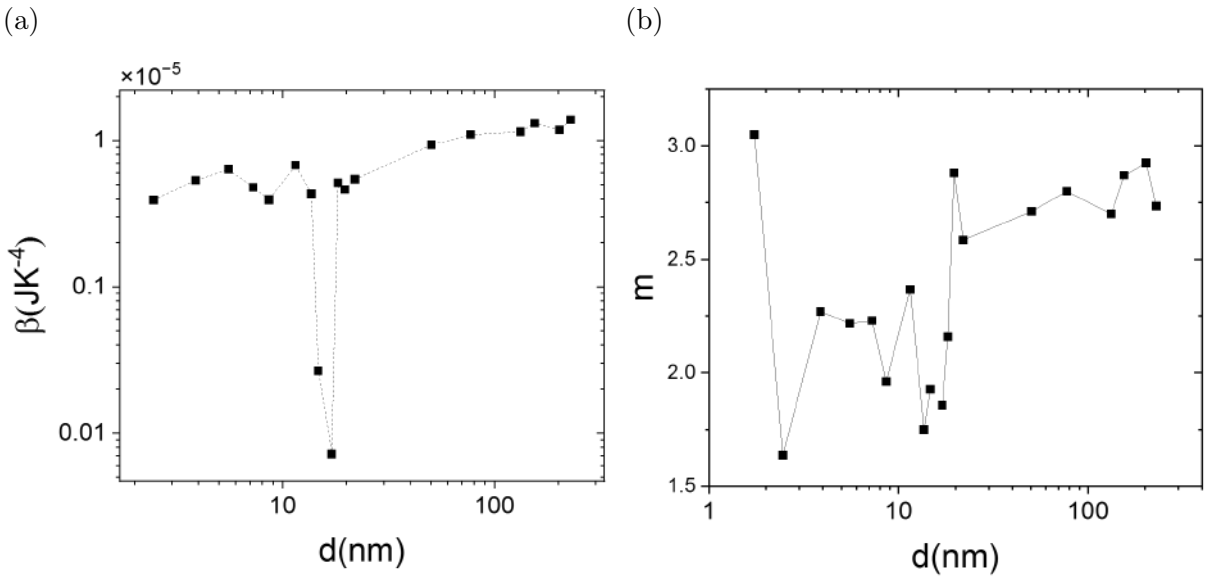

Figure 4.5: Analysis of the dominant heat carriers. (a) Plot of β vs. the film thickness (d), for different evaporation steps (2nd and 11th steps excluded for clarity). Noticeable drop in β value is observed at the intermediate layers. (b) Slope of log-log scale of the C_p (m) plotted vs. d. The slope is approximately 3 at the start and for thicker layers, but decreases and varies in between.

The values of β and m reveals the predominant heat carrier during the SIT, whether they are electrons or phonons. High β values, along with m of 3, indicate the prevalence of phonon heat carriers. This is evident in both the thinnest and thicker layers. A dramatic decrease in β values, reflects how the electronic contribution dominates, effectively burying the β signal. This, along with a drop in m, this indicates a shift towards electron dominance as heat carriers. The change in m values observed in the thinner to intermediate layers, with a m between 1.5 and 2.3, reflects variations in the dominant heat carriers. While phonons are the dominant heat carriers in the thicker and thinnest layers, at the intermediate layers, electrons also contribute significantly to heat transport. The subsequent restoration of a slope of $\approx$ 3 for the thicker layers implies a return to phonon dominance. This trend is also reflected in the gradual increase in β values within these thickness regimes. These findings provide evidence for unique behavior in the intermediate thickness layers, suggesting a fundamental difference in their properties and necessitating further discussion.

The discovery of a second pronounced feature in C_p for these layers is particularly significant, as it strongly suggests an additional, different, phase transition characterized by notable electronic modes. These pronounced electronic modes are evident by the change in heat carriers, as previously discussed, and can be clearly observed in the flat curves of the data (Fig.1.4(d)). Given that C_p measurements are highly sensitive thermodynamic measurements involving thorough equipment filtration, explanations involving artifacts are less plausible. Thus, the presence of an additional phase with increased electronic modes is suggested.

It should be noted that a similar experiment on granular Pb [35] did not show additional C_p structure at intermediate d. This discrepancy can be attributed to the substantial phononic contribution of the studied material, Pb [35, 57], which may have overshadowed this second

feature. In our experiment, the choice of a material with a higher Θ_D, i.e. In, as discussed in the Motivation chapter (2, enabled us to observe this phenomenon.

The key question is whether this second prominent feature indicates an additional phase transition, potentially pointing to the existence of an intermediate metallic state during the SIT, or does it represent a highly fluctuative zone with strong quantum fluctuations correlated with the emergence of electronic modes, such as vortices or superconducting fluctuations.

Ascribing the second C_p feature as an indicator of a genuine metallic ground state poses several challenges. The feature is characterized by a sharp increase, suggesting the sudden appearance of additional degrees of freedom within the system that persist to high T. The signal does not revert to the normal state signal but remains relatively flat and constant with T^2, implying that fluctuations in this state persist up to temperature well above T_c.

The nature of this sudden jump, along with the persistence of fluctuations at temperatures significantly above T_c, remains unexplained and requires further investigation and discussion. Future research involving the characterization of disordered materials with higher Θ_D values holds promise for shedding light on the nature of this second feature. However, despite the lack of full understanding, this behavior bears a strong resemblance to the heat capacity signature observed during *glass* transitions, where two specific heat peaks were identified [60, 61], with measurements typically showing a peak followed by an anomaly jump, after which the signal remains high and constant. This behavior is attributed to glasses being out-of-equilibrium systems with long relaxation times. The heat capacity measurement of a classic polymeric glass, polyvinyl acetate (PVAc) [62], shown in Fig. 4.6(a) alongside one of our intermediate stages (9th), highlights the similarity between their thermodynamic signatures. This resemblance may suggest the existence of a true BM ground state and supports the 'glassy model' for this phase, as the thermodynamic signatures exhibit characteristics typical of glassy phases.

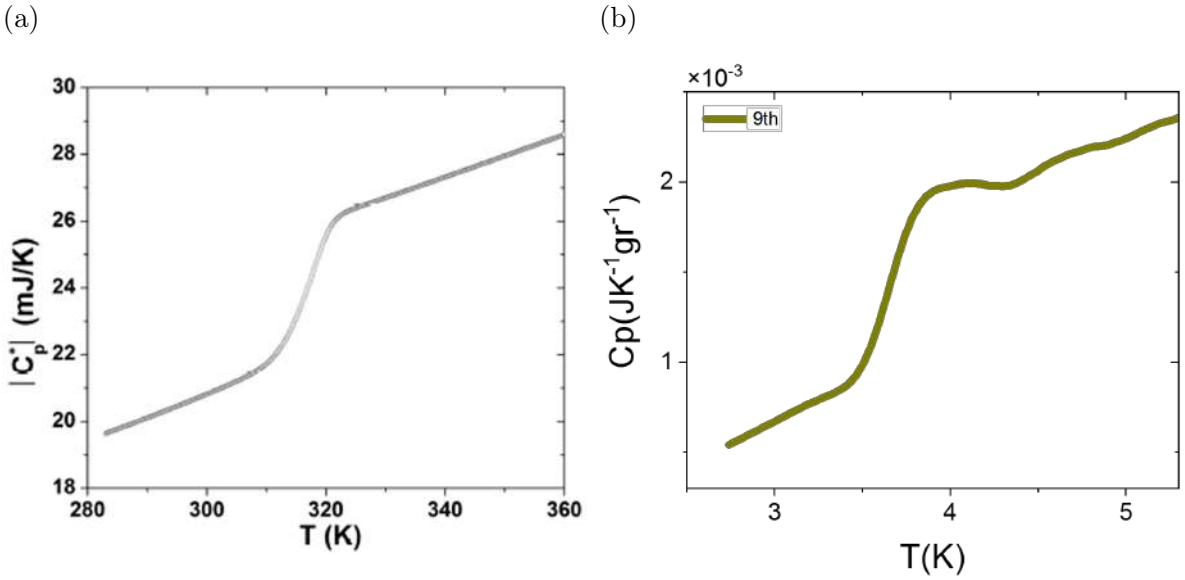

Figure 4.6: The resemble between the thermodynamic signature of (a) the heat capacity of glass polymer (reproduced from [62]) and (b) the intermediate In stages measured. Both exhibits a sharp jump and signal that persists high and constant at higher Ts.

While it remains uncertain whether this observation provides definitive evidence of a real metallic ground state, the presence of an additional phase with a unique thermodynamic signature is plausible. Clearly, this work requires additional theoretical support.

In summary, our investigation of the specific heat of ultra-thin layers of In has yielded new results, particularly within the intermediate thickness layers. The key findings can be summarized as follows:

1. Three different types of C_p curves are observed, representing different transport behaviors (see Fig. 4.7(a)). These variations in C_p behavior indicate distinct thermodynamic regimes. The different features observed in the films, along with the associated phenomena and transitions, occur at the same temperature range, underscoring that the system's behavior is closely tied to this T_c. For example, the features of the 4th and 9th steps (insulating and metallic films, respectively) coincide at exactly the same temperature, as highlighted by the green dashed line in the figure.

2. Two features in C_p are observed at the intermediate layers (see Fig. 4.7(b)), which lead to excess entropy at these stages (Fig.4.4). This phenomenon suggests complex thermodynamic behavior near the SIT, including the presence of strong quantum fluctuations, additional thermodynamic states, or degrees of freedom that contribute to the overall entropy of the system and may indicate a second phase transition occurring within the material.

3. A change in β and $\frac{C_p}{T}(T^2)$ slope (m) is observed, indicating variations in the dominant heat carriers across different film thicknesses (see Fig. 4.5). In the thinnest layers, where β values are high and m is 3, phonons appear to be the dominant heat carriers, a dominance that is also restored in the thicker layers. However, in the intermediate layers, a shift in dominant heat carriers is observed, with β values becoming obscured and m values ranging between 1.5 and 2.3. This suggests that the underlying physics governing heat transport in the material undergoes significant changes near the SIT, probably due to alterations in the electronic and phononic contributions.

These findings provide significant revelations into the thermodynamic properties of ultra-thin granular In layers and shed light on the complex behavior of systems near the SIT. Further research and development of theory are needed to explore and explain these phenomena in greater detail.

(a) (b)

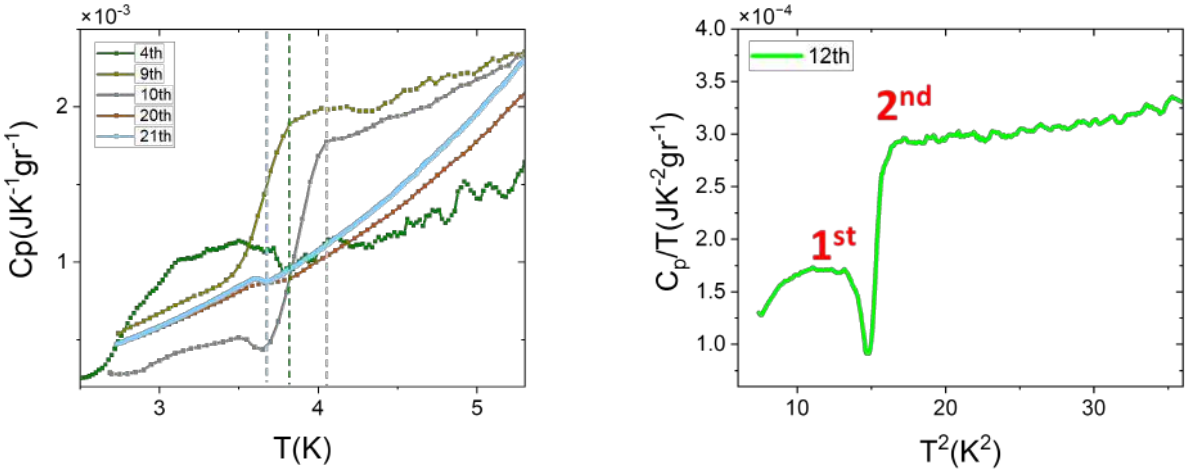

Figure 4.7: (a) C_p vs. T curves of selected representative films: insulating (4th), metallic (9th and 10th), and superconducting (20th and 21st) films. All curves display features around the same temperature, $T \approx 3.8K$, within the range of $\approx 3.6K$ to $4.05K$, as indicated by the light blue and gray dashed lines. Interestingly, the features of the 4th and 9th steps coincide at the same temperature, highlighted by the green dashed line. (b) The reduced C_p curve of the 12th layer, with a thickness of 17 nm, represents the intermediate layers that exhibit a secondary feature in C_p and weak phonon dependence. The weak phonon dependence is reflected in the curve's nearly constant behavior at higher temperatures.

4.2 Transport measurements of SNS junction- SLG/SC-dots bilayer devices

In the previous section we described the study of bosonic phases using a thermodynamic approach. Moving forward, we will delve into transport measurements to better understand the bosonic mechanism based on NS junctions, the building blocks of these bosonic phases. To achieve this, we engineered SC Josephson array devices consisting of a single layer of graphene (SLG) covered with an ordered array of SC InO dots, forming arrays of NS junctions. As illustrates in Fig. 4.8, we envision that our devices are composed of superconducting InO dots that exhibit electronic granularity (depicted as gray 'clouds' in the sketch). Each dot comprises several electronic grains that are Josephson-coupled. These electronically-granular dots form an array, with inter-dot connections dominated by Andreev Reflection (AR) processes.

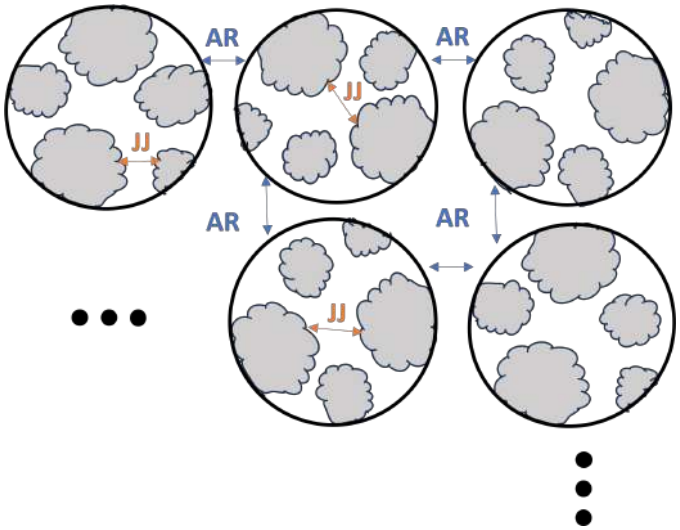

Figure 4.8: Sketch illustrating the structure of our SNS/SLG devices with superconducting InO dots. Each dot is electronically granular, consisting of multiple grains (represented by gray 'clouds') that are Josephson-coupled via Josephson junctions (JJ). Inter-dot connections are facilitated by Andreev Reflection (AR) processes occurring in the SLG regions between the dots.

We specifically designed the dots to be $1\mu m$ in diameter- large enough to maintain superconductivity, and spaced at an inter-dot distance of $200nm$, that results in devices exhibiting BM behavior. A characteristic transport measurement of a typical device is shown in Fig. 4.9, where the $R(T)$ measurements display saturated resistance at low temperatures for *various* V_g values.

A continuous InO film (without a SLG underneath) does not exhibit BM state during the SIT, as shown in the $R(T)$ measurements in Fig. 3.12. Thus, fabricating dots with specific parameters on top of SLG creates a unique situation where we access the BM state within a device comprising arrays of NS junctions. This method uniquely positions us to investigate the building blocks of the bosonic phase within the BM regime.

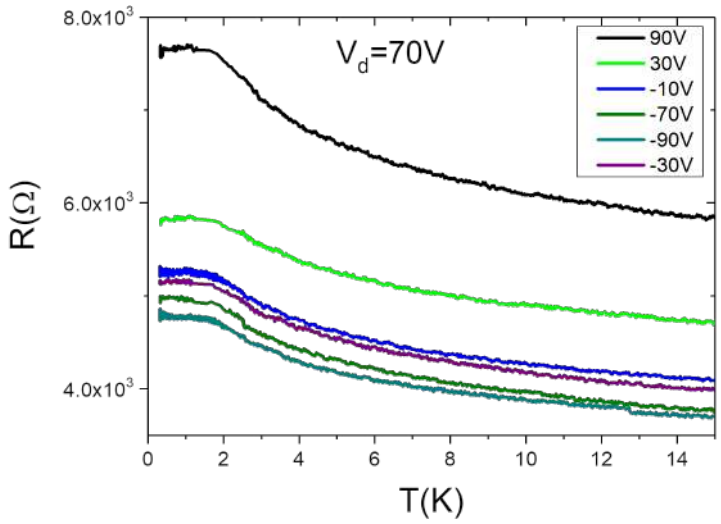

Figure 4.9: $R(T)$ measurements at different V_g values for a SLG/InO dot array device, with the Dirac point at $V_d = 70V$. The device exhibits BM behavior across the various V_g values.

Using both CVD graphene and exfoliated flakes for the SLG layer, we studied two distinct geometries: a two dimension matrix of dots (2D) and a single row of dots (1D). In total, we measured 6 large 2D devices ($200\mu m \times 115\mu m$, containing 167×95 junctions), 6 smaller 2D devices (with varying numbers of junctions), and 5 devices with 1D geometry, each containing 17 junctions. All devices from the same geometry exhibited similar results, ensuring the reliability of our findings. Here, we will present representative examples along with the main conclusions drawn from this study.

Our investigation uncovered a range of intriguing phenomena and features in these devices, offering insights into the underlying physics of the system. Through $R(V_g)$ measurements, we observed effects related to the internal distances within each dot, highlighting the significance of the dot's internal structure. Additionally, $\frac{dI}{dV}(V_{dc})$ measurements revealed the distinct behavior of the varied AR processes within this macro-metallic structure, emphasizing the complexity of electron transport in such a system.

Some of the results presented are not yet fully understood, but they offer valuable insights into how electronic granularity and AR processes influence the device's overall behavior. These findings contribute to a broader understanding of the system's properties and suggest potential future research directions.

While some additional results do not directly align with the primary focus of this research, their insights remain valuable. Therefore, these supplementary findings are included in the Appendix (B,C). This material covers extra measurements conducted at temperatures ranging from $300mK$ to $20K$ and under varying magnetic fields up to $9T$, along with their analysis.

4.2.1 Resistance versus V_g measurements

$R(V_g)$ curves were measured at base temperatures of $0.33K$ or $1.6K$ (depending on the cryogenic system used), with the primary objective of assessing the controllability of carrier density and

identifying the Dirac point (DP). The $R(V_g)$ measurements exhibited indications of superconductivity within the graphene, arising from its proximity to the SC InO dots. These signs of superconductivity manifested as a second peak- the 'superconducting Dirac point' (SDP) and fluctuations in $R(V_g)$.

Superconducting Dirac point

The $R(V_g)$ curve for large 2D arrays, such as the one shown in Fig. 4.10(a), revealed the presence of a second charge neutrality point. This is illustrated in Fig. 4.10(b), where the DP is observed at $V_g \approx -47V$, along with an additional peak at $V_g = -9V$. This second Dirac point bears resemblance to the SDP recently observed in our group [39], which was suggested to be related to the Andreev reflection (AR) processes in proximitized low n superconductivity regions within the graphene. The appearance of a SDP in the $R(V_g)$ curve serves as an indication of induced superconductivity in regions of the graphene, underneath the SC dots.

(a) (b)

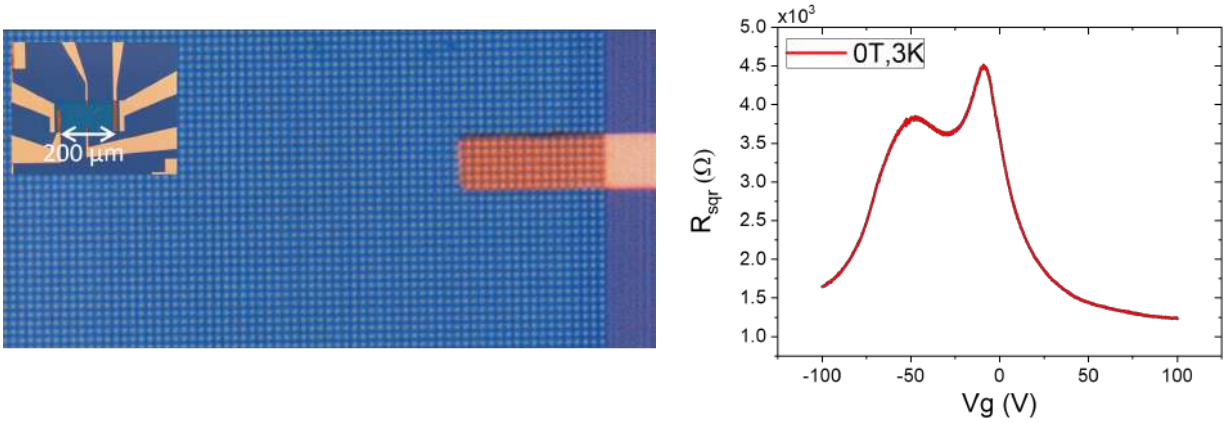

Figure 4.10: (a) Large 2D InO dot matrix with dimensions of $200\mu m \times 115\mu m$, containing 167×95 junctions, and (b) its $R(V_g)$ curve, showing two charge neutrality points at $V_g = -9.2V$ and $V_g \approx -48V$. Measurements were conducted at $B = 0T$ and $T = 3K$.

Such a well-defined SDP was observed in devices constructed from **large** dot matrices, such as those containing 18×31 junctions or more. However, when the matrix size was reduced and the number of junctions decreased, the SDP did not distinctly appear separate from the DP. In some cases, it seemed that the DP widened and 'contained' the SDP without a clear boundary between them. Additional effects on the SDP are discussed in Appendix C.0.1.

Another phenomenon observed in devices with fewer junctions was resistance fluctuations, which we describe next.

Resistance fluctuations

As mentioned, during the measurement of devices with fewer junctions, both CVD and exfoliated-based SLG, the SDP was not distinctly separated from the DP, and resistance fluctuations were observed as a function of $R(V_g)$, even though one would expect these fluctuations to average out given the presence of a few junctions. These fluctuations were most pronounced (with the highest amplitude) near the DP and persisted well above T_c ($T \gg 3.5K$). As the temperature increased, the amplitude of these fluctuations gradually decreased, eventually flattening out, resulting in a smooth $R(V_g)$ curve. Figure 4.11(a) shows an example from a 2D dot device, where resistance fluctuations are presented across the entire V_g range at different temperatures. The fluctuations are most pronounced at $1.66K$ and around the DP, measured at approximately $V_d = -14V$. At $T = 12K$, the fluctuations are significantly reduced but still persist, and by $20K$— well above T_c— the $R(V_g)$ curve becomes practically smooth.

In Fig. 4.11(b), the resistances at $1.66K$ (black curve) and $8K$ (blue curve) are shown after subtracting the resistance background from each, highlighting the fluctuation amplitudes. Although the fluctuations are reduced at higher temperatures, they persist above T_c and retain their overall structure. While the faster fluctuation features are 'erased,' the larger structural features remain. This underscores that these fluctuations are not noise but rather inherent to the dot array and its periodicity. The fluctuations are most pronounced in the DP regime (around $V_d = -14V$). The disappearance of fluctuations with increasing temperature is expected, primarily indicating the loss of mesoscopic electronic coherence. Additionally, this phenomenon can be attributed to the destruction of superconductivity as the temperature rises. Notably, these fluctuations persist at temperatures well above the T_c of InO, which is consistent with previous studies [39] that have shown superconductivity in InO can exist above its transport critical temperature.

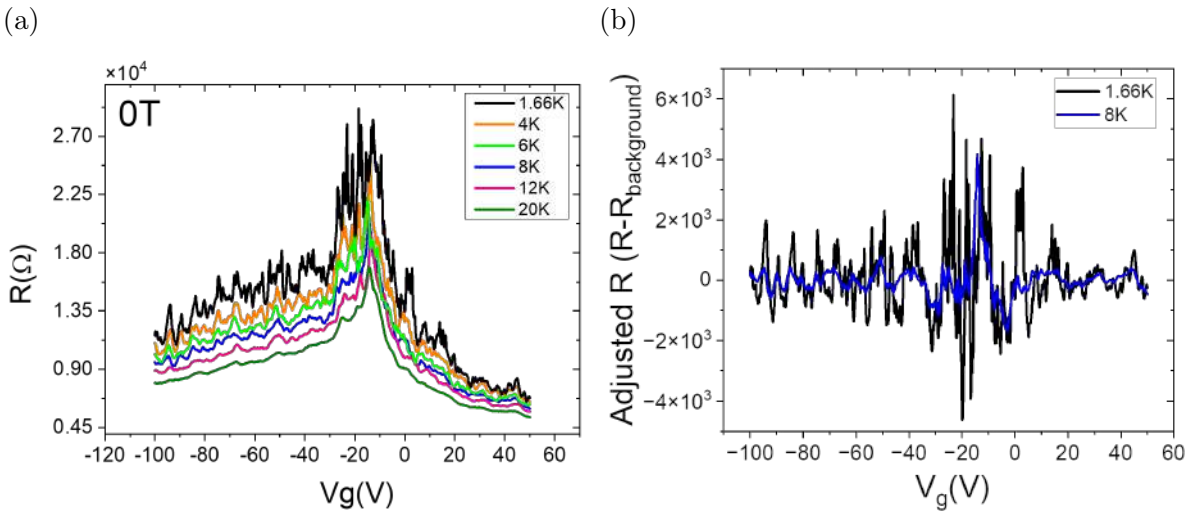

Figure 4.11: $R(V_g)$ at different T for a 2D dot array device with 4×5 junctions. Resistance fluctuations are clearly seen, with the most pronounced occurring at $1.66K$ and near the DP. (a) Raw $R(V_g)$s at varied Ts. As the temperature increases, the fluctuations are suppressed, resulting in a smooth $R(V_g)$ curve at $20K$. (b) Resistance fluctuations at $1.66K$ (black curve) and $8K$ (blue curve) after background subtraction, highlighting the persistence of fluctuations at higher temperatures, particularly in the DP regime.

Figure 4.12 shows an additional set of $R(V_g)$ measurements of device with 11×4 junctions. Measurements were taken at $B = 0$ and various temperatures, ranging from a base temperature of $0.33K$ to $20K$ (panel (a)), and at $T = 0.33K$ under different magnetic fields (panel (b)). The $R(V_g)$ fluctuations are influenced by temperature, but are not significantly affected by applied magnetic fields. The amplitude of the fluctuations remains relatively consistent up to a field of $5.5T$. This is illustrated in panel (b), where ΔR, the $R(V_g)$ curves normalized to their resistance value at the DP ($V_d \approx 75V$), are shown with slight offsets for clarity.

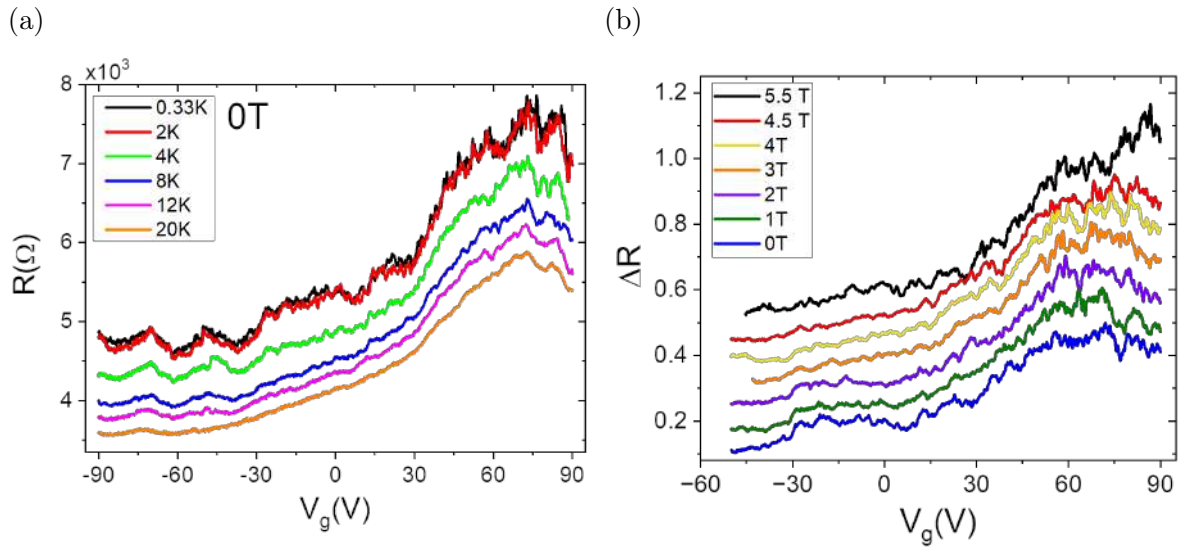

Figure 4.12: Oscillatory $R(V_g)$ measurements (a) At $0T$ and different temperatures, and (b) ΔR, the $R(V_g)$ curves normalized to their resistance value at the DP ($V_d \approx 75V$), with a slight shift from each other for clarity. Measurements in (b) were taken at a base temperature of $0.33K$ under varied magnetic fields.

Interestingly, the applied magnetic field did not influence the amplitude of these fluctuations, despite expectations that it would suppress superconductivity. However, it is worth noting that the $5.5T$ field is below the critical magnetic field (H_c) of our superconducting InO, which is approximately $8T$ at $T = 1.66K$ [63]. Moreover, interestingly, the structure of these fluctuation remains unaffected by the magnetic field.

Oscillations of an order parameter, such as the observed resistance fluctuations, at varying magnetic fields would typically suggest orbital effects like the Aharonov-Bohm effect [64]. If this were the case, we would expect these fluctuations to vanish under a magnetic field. Furthermore, if these fluctuations were caused by magnetic flux circulating within the sample, the magnetic field would alter the electron wave interference patterns. Additionally, the magnetoresistance of these devices did not exhibit periodic variation with the field. The lack of changes in fluctuations despite the applied magnetic field suggests that other mechanisms are likely responsible for the observed phase fluctuations. One possibility is specific AR scattering patterns within the graphene, occurring between its N and S regions, induced by the superconducting InO dots. We propose that these fluctuations may correspond to standing waves, described by multiples of $K_F \cdot l = N$ (where K_F is the Fermi wave vector, l is a constant distance, and N is an integer), which are independent of the magnetic field and potentially influenced by the dots. This scenario aligns with previous theoretical work by Prof. Shimshoni's group and ours (see supplementary materials of [40]), which demonstrated that the critical current (I_c) of a single InO/SLG Josephson junction oscillates with gate voltage, considering the formation of Andreev bound states (ABS) within the junction, as shown in Fig.4.13. Additionally, these oscillations were most pronounced near the overall maximum at the CNP. These features were expected to be observable only in very clean devices comprising a *single Josephson junction*, as in larger

devices composed of many N-S junctions, they would average out. Interestingly, in our devices with a few N-S junctions, resistance fluctuations persist and do not fully average out, contrary to initial expectations.

(a)

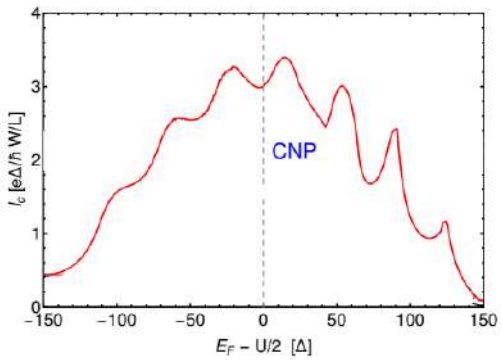

Figure 4.13: I_C evaluation in a single InO/SLG SNS Josephson junction as a function of E_F (in units of Δ). I_C shows an overall maximum near the CNP, along with several oscillations arising from Andreev bound states. U represents the energy shift due to the difference in electrostatic potential induced by the superconducting InO. Reproduced from the supplementary materials of [40].

To further investigate the fluctuations in $R(V_g)$ and uncover their underlying mechanisms, we conducted a Fast Fourier Transform (FFT) analysis. Here, we present one analysis of the $R(V_g)$ curve at $1.66K$, depicted in Fig. 4.11. Since the fast fluctuations are superimposed on an overall common background in $R(V_g)$, the first step in the analysis was to normalize the R curves to the smooth background— specifically, the resistance measured at $12K$. The resultant normalized $R(V_g)$ curve is shown in Fig. 4.14(a).

Fluctuations in $R(V_g)$ reflect changes in the carrier density, n, which directly affect the Fermi wave vector, k_F. In a 2D system, this is described by the relation $k_F = \sqrt{2\pi n(V_g - V_{Dirac})}$. Here, V_{Dirac} is measured at $-14V$, and $n = 6.56 \times 10^{14}$ accounts for the $285nm$ thick SiO layer on the chip (following the equation: $q = ne$). The representation of $R(k_F)$ is shown in Fig. 4.14(b). Transforming $R(V_g)$ to $R(k_F)$ helps link fluctuations to a physical length scale. In our setup, we propose that the current between the SNS junctions in graphene forms a 'standing wave', described by $k_F \times \lambda_F = 2\pi n$, where λ_F is the Fermi wavelength. This allows us to convert between $R(V_g)$ and $R(k_F)$. Applying FFT on $R(k_F)$ reveals the main length scale L (the Fermi wavelength λ_F) of these fluctuations. The results, with the X-axis converted to real L values, are shown in Fig. 4.14(c).

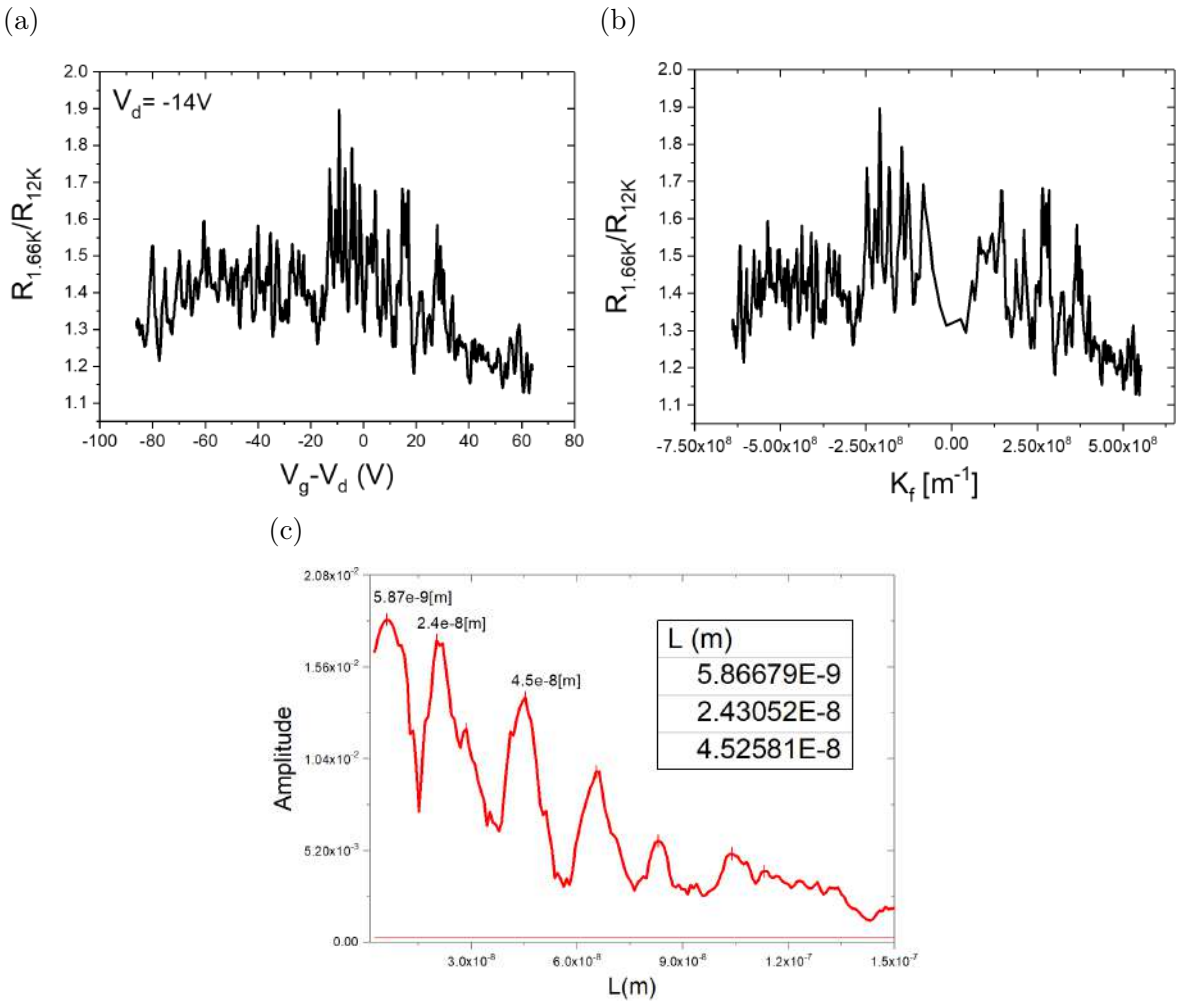

Figure 4.14: The analysis process used to detect the physical length scale related to the resistance fluctuations. (a) Normalized resistance at $T = 1.66K$, normalized to the smooth resistance measured at $T = 12K$. (b) Transformation from $R(V_g)$ representation to $R(K_F)$ representation. (c) FFT results of $R(K_F)$ curve, which extracting L.

The FFT analysis revealed fluctuations in K_F with length scales ranging from approximately $6nm$ to $45nm$, indicating the presence of an *intrinsic* length scale in our system. This result was consistent across all six smaller 2D array devices measured.

We attribute these findings to the emergent granularity of our superconducting InO. Each dot consists of smaller electronic grains, varying in distance and coupled to each other via Josephson junctions. Given the small size of our dots ($1\mu m$), only a few dominant distances exist within each dot, as identified through FFT analysis. Additionally, the short length scale of $R(V_g)$ fluctuations aligns with the superconducting pair coherence length, ξ_{pair}, which is estimated to range between $5nm$ and $30nm$ [65]. This suggests that $R(V_g)$ fluctuations are primarily influenced by the dot's intrinsic length scale— specifically its granularity and pair coherence length— rather than by its overall size or junction length. In this sense, the observed fluctuations offer a window into the microscopic structure of the grain granularity. Due to the presence of multiple dominant length scales (each associated with a specific ξ_{pair}), the fluctuations lack a clear periodicity. In contrast, conductance measurements as a function of the bias voltage

revealed well-defined oscillations, as discussed next.

4.2.2 Conductance versus V_{dc}

In the following section, we compare the differential conductance ($\frac{dI}{dV}(V_{dc})$ curves from two typical SLG/SC devices: a 1D row of 17 sequential dots (see Fig. 4.15(a)) and a small 2D array of 16×5 dots (see Fig. 4.15(b)). Both devices were fabricated as detailed in the Experimental Methods section (3.2), under a partial oxygen pressure of approximately 1×10^{-5} mbar, resulting in disordered superconducting dots with a T_c of $\sim 3.5K$. All electronic measurements were conducted in a He^3 fridge at $T = 0.33K$ under a $0T$ magnetic field.

(a) (b)

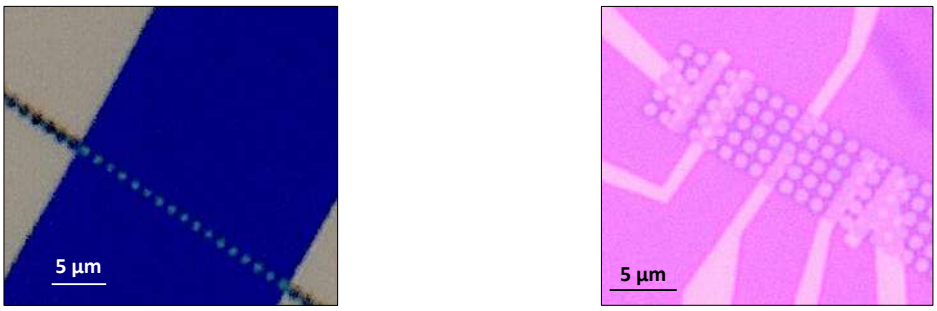

Figure 4.15: Optical microscope images of 1D (a) and 2D (b) samples of SLG/SC-dot-array configurations.

To ensure comparability, the $\frac{dI}{dV}(V_{dc})$ measurements were normalized to their $V_{dc} = 30mV$ values to account for variations in the resistance backgrounds of the different devices. The $\frac{dI}{dV}(V_{dc})$ measurements exhibit not only energy gap peaks (or dips) indicating superconductivity, but also unique oscillation patterns that intricately depend on both V_{dc} and V_g. These oscillations occurred both within and outside the density of states (DOS) gap, with distinct frequency differences between the 2D and 1D devices. The most pronounced patterns were found in the single-row (1D) devices.

The complex structure of the $\frac{dI}{dV}(V_{dc})$ curves is attributed to the interplay of three fundamental processes, concurrently operating within the system;

1. A depletion of the electronic DOS around the Fermi level due to the Altsuler-Aronov (AA) mechanism of electron-electron interactions in disordered films [66].

2. A Superconducting gap, Δ, in the graphene regions below the InO dots due to the proximity effect [40], each with an expected bias scale of $\Delta_{InO} \approx 0.7mV$ [55].

These two effects were anticipated. However, the data also revealed an unexpected third phenomenon:

3. Electronic quantum interference effects, which depend on the Fermi velocity of graphene, $V_F \approx 10^6 m/s$, and the periodic structure of superconducting-normal region interfaces.

Fig. 4.16(a) displays the conductance (G) measurement (at $V_{dc} = 0$) of a **1D** device, plotted as a function of V_g. It can be seen that G exhibits a dip near $V_g \sim 0$. A closer look reveals that this broad dip is composed of two dips- one corresponding to the DP ($V_g \approx -10V$) and the other, at $V_g = -29V$, to the SDP, indicating the presence of superconductivity in the graphene. In Fig. 4.16(b), the $\frac{dI}{dV}(V_{dc})$ curves at different V_g values are depicted, spanning the electron side, the DPs regime, and the hole side. All curves exhibit a fairly similar DOS 'background' shape, including a broad dip (in which $\frac{dI}{dV} < 1$) and a characteristic superconducting gap, Δ. However, the key finding is the presence of discernible oscillatory patterns in the $\frac{dI}{dV}$ curves at different V_g values, which vary in their patterns. The presence of these oscillations depends on the measured gate voltage and can manifest throughout the entire V_{dc} range, exclusively outside the gap, or not at all. To illustrate this more clearly, selected curves depicting oscillations at different V_{dc} regimes are individually plotted in sub-figures (c-h) of Fig. 4.16.

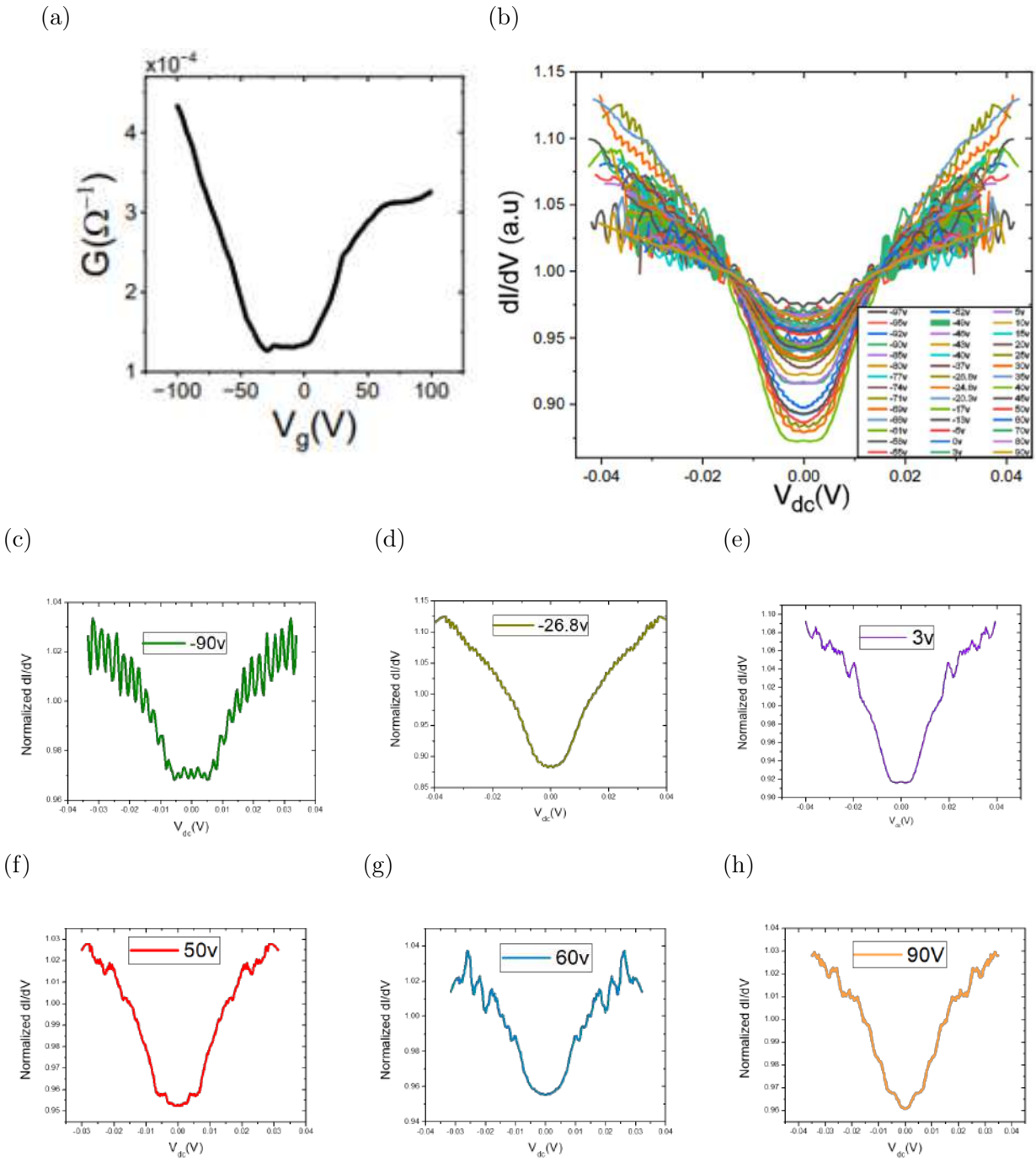

Figure 4.16: (a) Conductance versus V_g of the 1D device and (b) corresponding $\frac{dI}{dV}(V_{dc})$ measurements at different gate voltages. The measurements were taken at $T = 0.33K$ and $B = 0T$. (c-h) Selected $\frac{dI}{dV}$ vs. V_{dc} curves at different V_gs.

In Fig. 4.17 the conductance vs V_g and the $\frac{dI}{dV}(V_{dc})$ measurement of a **2D** device are presented. As can be seen in Fig. a4.17(b) this resulted in varied $\frac{dI}{dV}$ curves' shapes- including zero bias dips, peaks and "in between" types of shapes. Besides their extremum 'type', the $\frac{dI}{dV}$s differ also by their gap's width, depth, at their coherence peaks. A glimpse of the rich diversity

measured at the $\frac{dI}{dV}$s, can be seen in Fig. 4.17 (c-h), where chosen curves are shown separately.

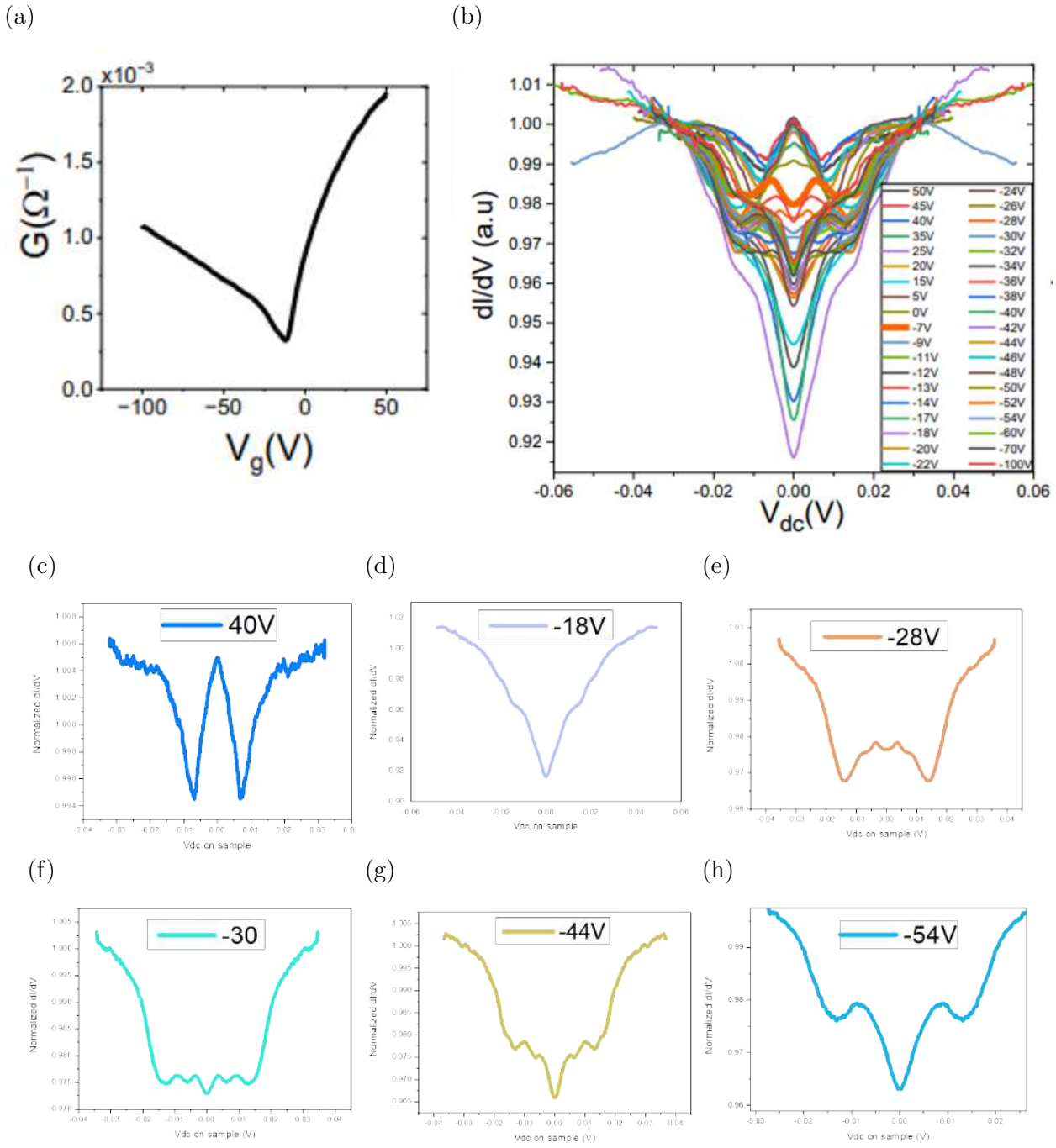

Figure 4.17: **2D device** (a) $G(V_g)$ of the device (b) $\frac{dI}{dV}$ vs V_{dc}, at varied V_gs. (c-g) Chosen $\frac{dI}{dV}$s from Fig. 4.17 (matching color code). Peaks, dips, varies gap widths and divergent curves shapes can be seen at the various gate voltages.

Various fine features are apparent in the $\frac{dI}{dV}(V_{dc})$ curves, in both the 1D and 2D devices. In the subsequent subsections, we delve into a detailed examination of the diverse oscillation patterns.

In order to analyze appropriately these results, one would like to decompose the different

physical contributions of the data. One naive way to do so would be to employ a simple Fast Fourier transform (FFT). However, the intricacies involved largely rule out a 2D Fourier transform of both V_{dc} and V_g. Even attempting a Fourier transform solely for V_{dc} at a fixed V_g where the oscillatory behavior is unmistakable (see Fig. 4.18), no distinct peak in frequency is evident. This lack of clarity in frequency peaks makes it challenging to draw meaningful conclusions from the Fourier transform analysis.

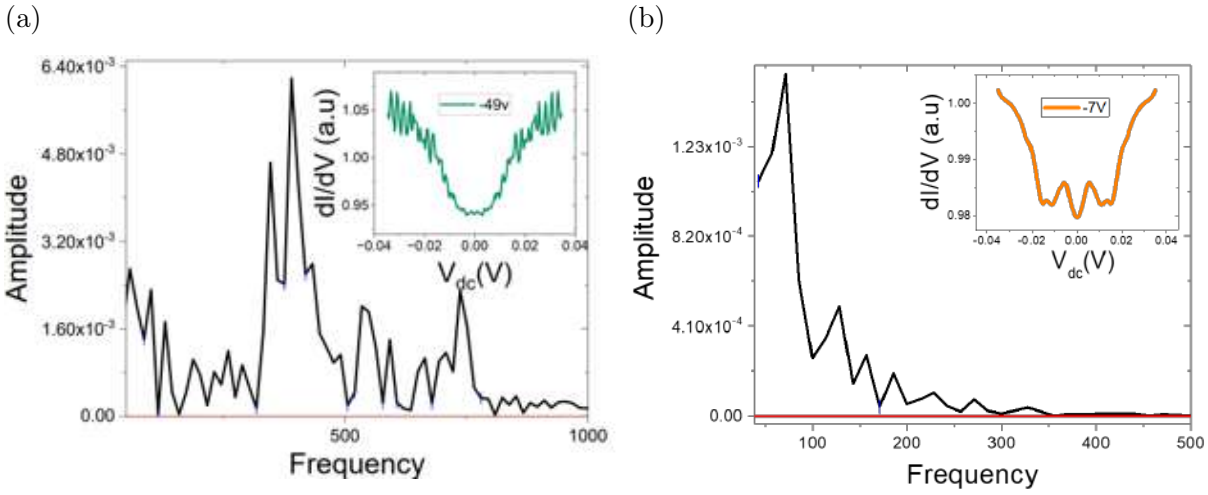

Figure 4.18: FFT analysis of the $\frac{dI}{dV}(V_{dc})$ measurement of (a) 1D sample at $V_g = -49V$, appears in the inset. Even though a clear oscillation pattern is seen in the raw data, the FFT didn't result in a distinct peak. Same in (b) for the 2D device, of $\frac{dI}{dV}(V_{dc})$ measurement at $Vg = -7V$.

In addition, such an analysis method requires separate calculations for each individual V_g value in an attempt to identify repeating patterns. Clearly, a more useful and efficient analysis tool is required. Working in collaboration with Berkovits ([67]), this led us to employ the **Singular Value Decomposition** (SVD) technique, which was found to be systematically useful in analyzing our results.

4.2.3 The SVD method

The SVD technique has a wide range of applications in various fields, including data compression [68–71] and machine learning [72, 73]. It holds significant potential for analyzing complex experimental data, particularly data arising from distinct physical mechanisms concurrently influencing the results. By adjusting a control parameter, these mechanisms can be modulated to varying degrees, eliminating the need for prior assumptions in modeling their contributions to the measurements.

In our study, we harness the power of SVD to analyze the complex $\frac{dI}{dV}$ measurements of the 1D and 2D SC dots arrays, that exhibit a pronounced dependence on both bias and gate voltages, as can be seen in Fig. 4.16(b) and 4.17(b). Oscillations in relation to the dc voltage, with seemingly distinct periods in different regions, are observed. Through SVD analysis, we aim to untangle this intricate data, gaining valuable insights into the dependence of experimental measurements on the two parameters and the underlying physics.

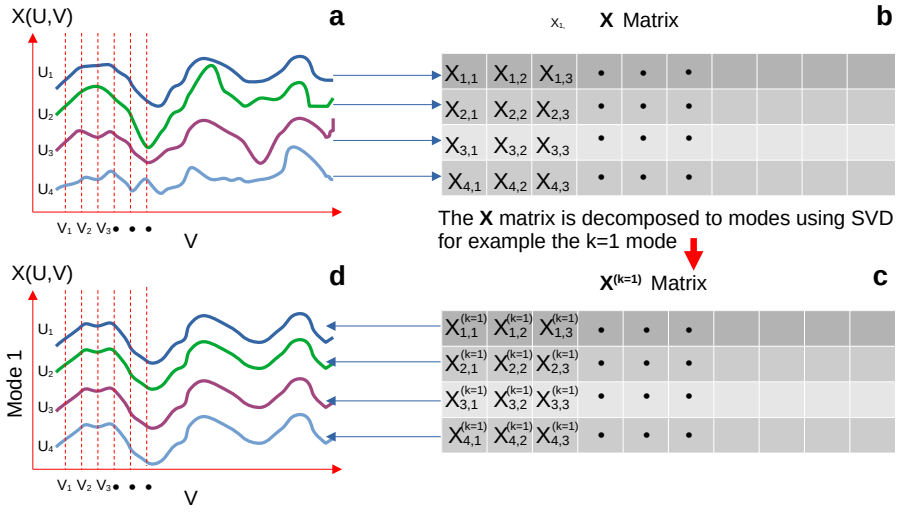

Figure 4.19: A schematic cartoon of the SVD procedure. In (a), a physical observable X, dependent on two parameters U and V, is measured. The procedure involves setting U_i ($i = 1, 2, \ldots$) while changing V, resulting in the curves for $X(U_i, V)$ illustrated in the graph. In (b), to represent the data as a matrix $\mathbf{X}$, V is discretized into V_j, and each value of $X(U_i, V_j)$ is inserted as the matrix element $X_{i,j}$. Thus, each row corresponds to the measurements for a given value of U_i. The SVD procedure is applied, yielding a series of matrices $\mathbf{X}^{(k)}$, with the original matrix expressed as a sum of modes $\mathbf{X} = \sum_k \sigma_k \mathbf{X}^{(k)}$, where σ_k is the singular value amplitude, and the modes are ordered by magnitude from the largest. In (c), the matrix for the largest mode, $k = 1$, is represented. Due to the structure of the SVD procedure (see text), each matrix element in $\mathbf{X}^{(k=1)}$ is equal to $\vec{U}_i^{(k=1)} \vec{V}_j^{(k=1)}$. Thus, each row is equivalent to the same vector $\vec{V}^{(k=1)}$ multiplied by a different constant $\vec{U}_i^{(k=1)}$. This relationship is illustrated in the plot (d), corresponding to the curves $X(U_i, V)$ for the first mode.

SVD, a linear algebra technique, allows the rewriting of any matrix with dimensions $M \times P$ as a sum of amplitudes (termed singular values) multiplied by an outer product of two vectors, where the number of terms is determined by $\min(M, P)$. The singular values, enabling the approximation of the original matrix through a sum over a reduced number of the larger terms, significantly fewer than $\min(M, P)$. Details of this process can be found in our recent paper [67].

Given that our results depend on two parameter V_{dc} and V_g, one can organize the data by performing M measurements of one parameter where for each such measurement the second parameter is measured P times (see Scheme 4.19a), into an $M \times P$ matrix. SVD proved invaluable in reducing the dimensionality of our data while preserving essential information and revealing hidden patterns, such as oscillation patterns observed in the conductivity measurements.

The initial step in applying SVD analysis involves transforming the experimental measurement $X(U, V)$, dependent on parameters V and U, into a matrix. Consequently a $M \times P$ matrix $\mathbf{X}_{ij} = X(U_i, V_j)$ can be constructed as schematically illustrated in Fig. 4.19.

In the SVD procedure, the matrix $\mathbf{X}$ is expanded as a sum of amplitudes σ_k multiplied by $M \times P$ matrices $\mathbf{X}^{(k)}$. These matrices are constructed by an outer product of two vectors $\vec{U}_i^{(k)}$ and $\vec{V}_j^{(k)}$ of sizes M and P, respectively. Explicitly, $\mathbf{X}$ is decomposed into $\mathbf{X} = \mathbf{U}\mathbf{\Sigma}\mathbf{V}^T$,

where $\mathbf{U}$ and $\mathbf{V}$ are $M \times M$ and $P \times P$ matrices, respectively, and $\mathbf{\Sigma}$ is a diagonal matrix of size $M \times P$ with a rank $r = \min(M, P)$. The r diagonal elements of $\mathbf{\Sigma}$ are the singular values (SV) amplitudes σ_k of $\mathbf{X}$. These SVs are positive and can be ordered by magnitude as $\sigma_1 \geq \sigma_2 \geq \ldots \geq \sigma_r$. As discussed, $\mathbf{X}$ can be expressed as a series of matrices $\mathbf{X}^{(k)}$, i.e., $\mathbf{X}_{ij} = \sum_{k=1}^{r} \sigma_k \mathbf{X}_{ij}^{(k)}$, where $\mathbf{X}_{ij}^{(k)} = \mathbf{U}_{ik}\mathbf{V}_{jk}^{T} = \vec{U}_i^{(k)}\vec{V}_j^{(k)}$. The sum of the first m modes provides an approximation $\tilde{\mathbf{X}} = \sum_{k=1}^{m} \sigma_k \mathbf{X}^{(k)}$ to X, representing the minimal departure between the approximate measurements, $\tilde{\mathbf{X}}$, obtained using $m(M + P + 1)$ independent variables compared to the full energy spectrum, which requires MP variables. This forms the basis for the use of SVD as a data compression method. Since, for most cases (including those discussed here), the SVs drop rapidly as a function of k, a good approximation of $\mathbf{X}$ is achieved. Indeed, examining the SVs as a function of k, typically involving a Scree plot plotting $\lambda_k = \sigma_k^2$ vs. k on a logarithmic scale, serves as the first step in analyzing the data.

The SV amplitudes, σ_k, corresponding to significant modes (typically with $k \sim O(1)$), along with the associated vectors $\vec{U}^{(k)}$ and $\vec{V}^{(k)}$ for these modes, play a crucial role in interpreting experimental data. This importance can be illustrated through an analogy with one of the most widely used experimental data analysis methods, the Fourier transform. In the case of a Fourier transform, the experimental results $X(U_i, V_j)$ can be expressed as $\sum_{k_i,k_j} f_{k_i,k_j} \sin(k_i) \sin(k_j)$. Superficially, the structure bears similarity to the SVD sum, as both involve an amplitude multiplied by two vectors or functions. In both methods, the goal is to identify amplitudes significantly larger than others to characterize the data. Furthermore, the general dependence of these amplitudes on the mode or frequency can offer insights into the overall characteristics of the system, such as the presence of $1/f$ noise.

Nonetheless, significant distinctions exist. The SVD sum involves just $r = \min(M, P)$ amplitudes, a stark contrast to the MP amplitudes present in the Fourier transform. This reduction in the number of terms in the SVD sum arises because, unlike the fixed vectors involved in the outer multiplication of the Fourier transform, the vectors in SVD are optimized to achieve the best fit with a minimal number of modes. Consequently, in contrast to the Fourier transform, valuable insights are gained not only from the amplitudes but also from the optimized vectors $\vec{U}^{(k)}$ and $\vec{V}^{(k)}$ associated with contributing modes.

With that being said, now we will elaborate on these somewhat vague ideas by implementing them using concrete experimental data.

4.2.4 SVD analysis of the data

In Fig. 4.20, a scree plot illustrates squared SV amplitudes ($\lambda_k = \sigma_k^2$) in relation to the mode number k. Notably, the largest SV amplitude ($k = 1$) is orders of magnitude greater than subsequent modes. Beyond $k = 3$, a power-law behavior emerges. Specifically, the 1D chain exhibits a power law described by $\lambda_k \sim k^{-1.3}$ (Fig.4.20(a)), while the 2D sample follows a steeper power law, $\lambda_k \sim k^{-4}$ (Fig.4.20(b)). This disparity in power laws is significant; as demonstrated in the appendix of Ref.[74], a power law of $\lambda_k \sim k^{-1}$ corresponds to $1/f$ noise. Consequently, modes $k = 3-15$ for the 1D sample appear to align with characteristics of $1/f$ noise. In contrast, the 2D

sample seems well-characterized by the initial few modes, as the contribution from subsequent modes rapidly diminishes. This observation is reinforced by noting that measurements of the 1D sample exhibit greater noise compared to those of the 2D sample (Figs.4.16(b) and 4.17(b)). This power-low behavior in lambda values was repeated in other 1D and 2D devices that were analyzed using SVD, where a matching behavior of power-law was found. Their scree plots can be found in the Appendix (D).

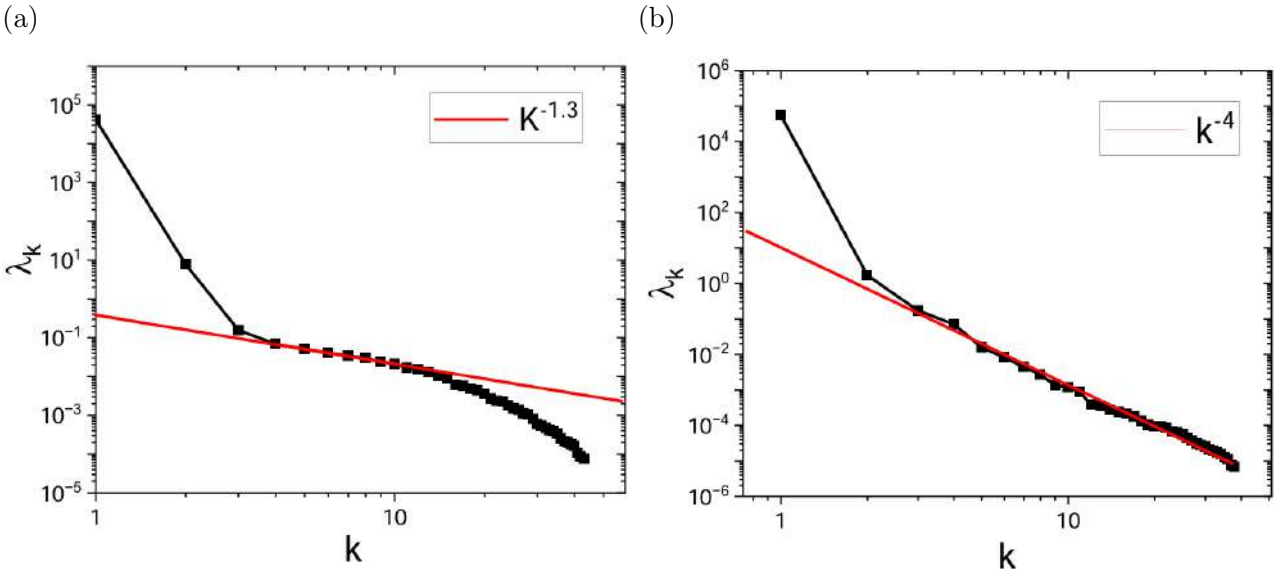

Figure 4.20: λ_k vs. k for the (a) 1D and (b) 2D samples. The first mode is orders of magnitude larger than the rest, while the second mode deviates from the power-law behavior of (a) $\lambda_k \sim k^{-1.3}$ and (b) $\lambda_k \sim k^{-4}$ observed for the larger modes.

The SVD's λ values and their power behavior provide insights into which SVD modes hold the common behavior and which offer fine corrections to the overall $\frac{dI}{dV}$ behavior. It is evident that the few-first modes (first to ∼fifth) capture the common features of the $\frac{dI}{dV}$ curves. As the mode number increases, their contribution to the universal behavior decreases following a power law. In other words, higher modes primarily represent the fine corrections to the overall $\frac{dI}{dV}$ behavior.

Now, let us delve into an examination of the contributions from the first few individual modes.

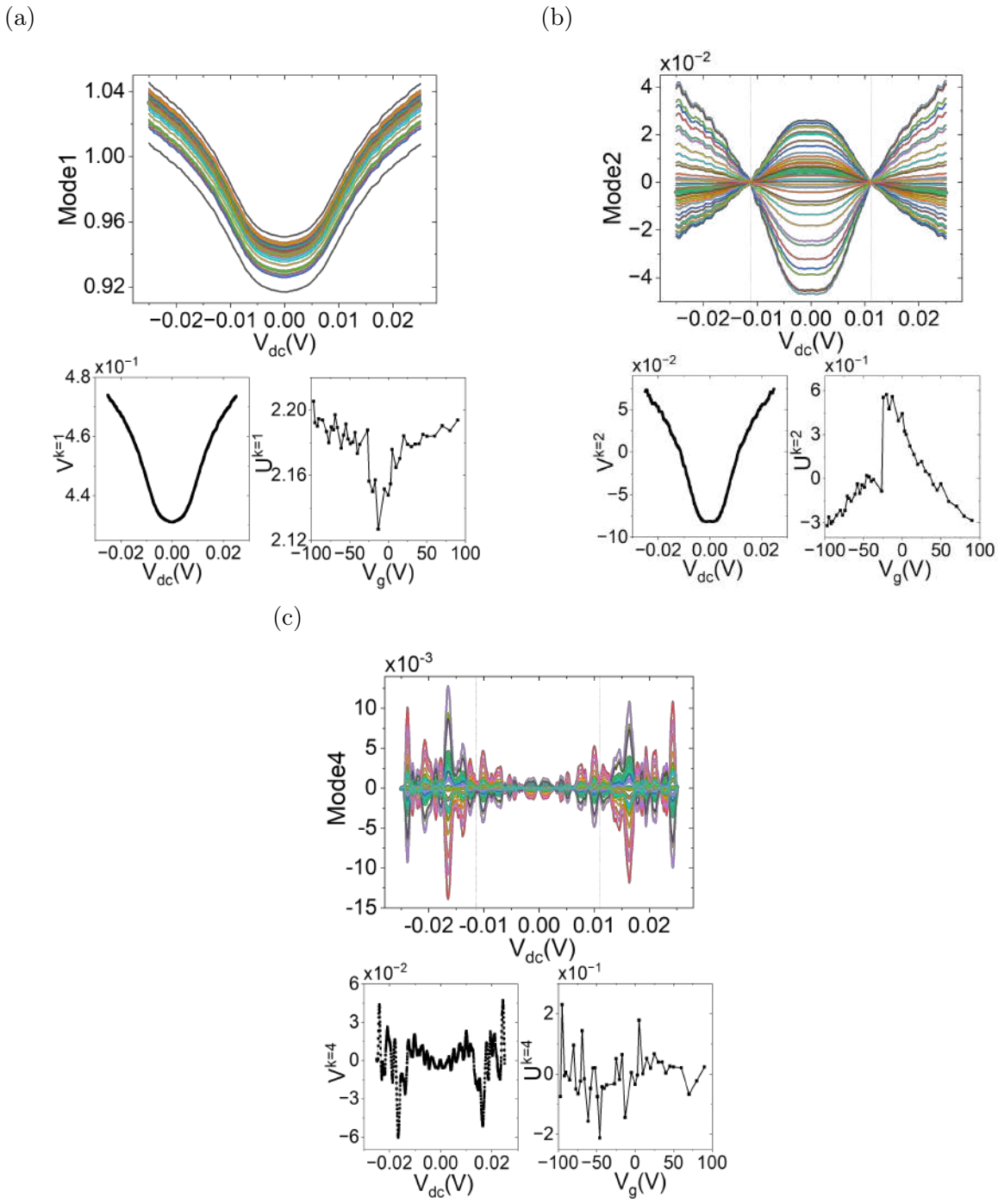

Figure 4.21: SVD analysis of a $1D$ dots device (a) the 1^{st} mode, extracting the common data background (b) 2^{nd} mode, where the superconducting gap was extracted and marked between the two red lines (c) the 4^{th} mode, where the oscillations pattern can be seen.

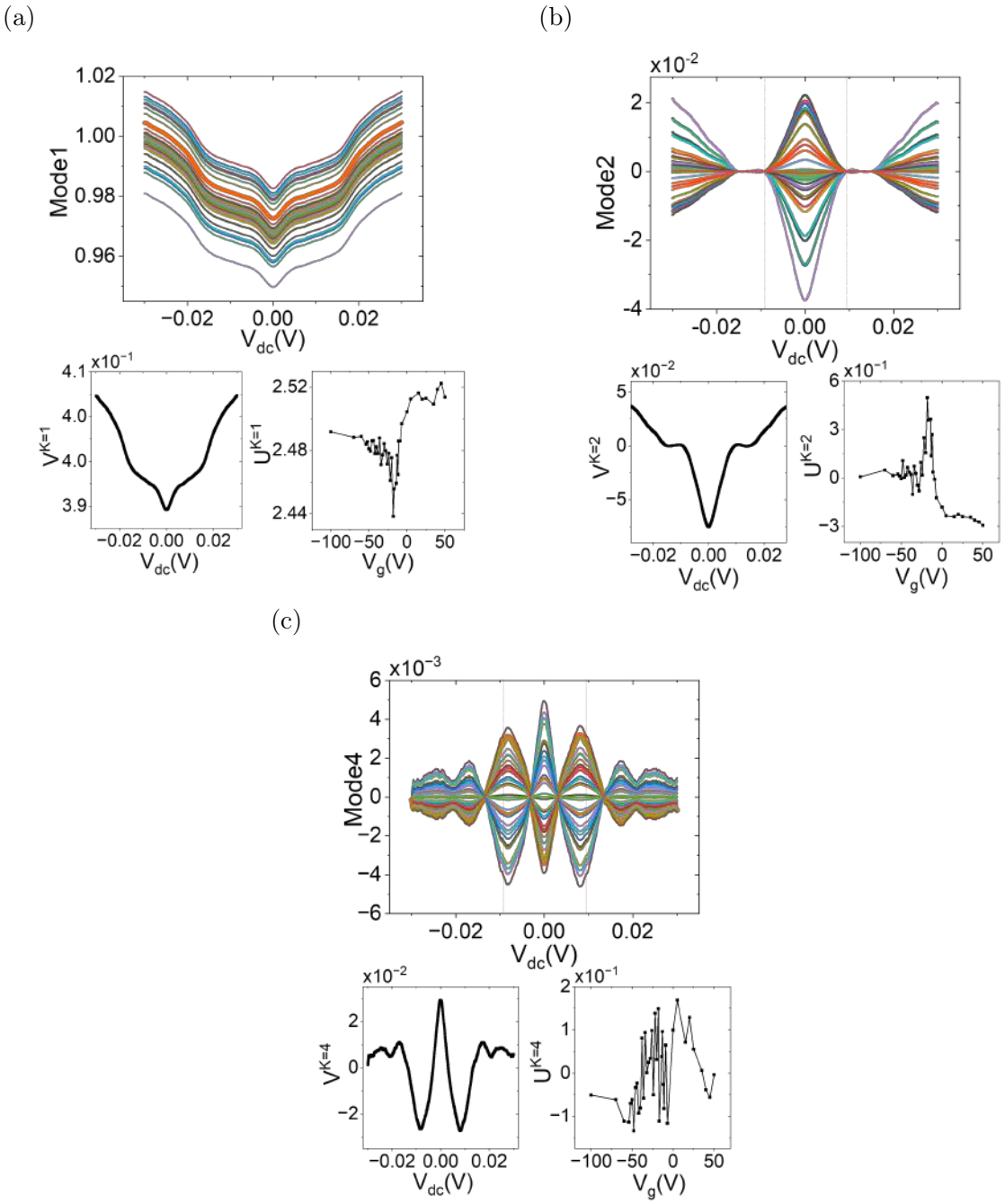

Figure 4.22: SVD analysis of a $2D$ dots device (a) the 1^{st} mode, extracting the common data background (b) 2^{nd} mode, where the superconducting gap was extracted and marked between the two red lines (c) the 4^{th} mode, where the oscillations pattern can be seen.

The contributions of the first mode ($k = 1$) to the measured data are shown in Fig. 4.21(a) for the 1D sample and Fig. 4.22(a), for the 2D sample, along with the associated vectors $\vec{V}^{(k=1)}$ and $\vec{U}^{(k=1)}$. The differential conductance, dI/dV, as a function of V_{dc} for various values of V_g is plotted, where the various values are coded with the same color code as in Figs.4.16, 4.17 respectively. As discussed, $\mathbf{X}^{(k=1)} = \sigma_1 \vec{V}^{(k=1)} \otimes \vec{U}^{(k=1)}$. The outer multiplication between these two vectors has a transparent interpretation. Specifically, the vector $\vec{V}^{(k=1)}$ captures the first mode's dependence of the differential conductance, dI/dV, on V_{dc}. Consequently, the vector $\vec{V}^{(k=1)}$ is multiplied by the term of the vector $\vec{U}^{(k=1)}$ that corresponds to the appropriate value of V_g. This relationship is visually evident in the main panels of Figs.4.21(a) and 4.22(a), where the multiplication of $\vec{V}^{(k=1)}$ by the corresponding value of $\vec{U}^{(k=1)}$ is plotted for each term of $\vec{U}^{(k=1)}$, i.e., for each value of the gate voltage V_g.

Hence, the first mode derived from the SVD provides an overall insight into the behavior of the differential conductance. For our samples, we associate this gross feature with AA depletion in disordered metals. AA depletion manifests in a logarithmic increase in the differential conductance, which is truncated at low voltage due to temperature. Indeed, in the case of the 1D sample, the first mode vector $\vec{V}^{(k=1)}$ exhibits a broad minimum around $V_{dc} = 0$, followed by a logarithmic increase (see Fig. 4.23(a)). For the 2D sample, the behavior is more intricate, and a sharp minimum at $V_{dc} = 0$ appears, revealing a more distinct structure that needs further explanation (see Fig. 4.23(b)). It's noteworthy that, unlike modes in the Fourier transform, SVD tailors its vectors to the specific measurements, as exemplified by the contrast between $\vec{V}^{(k=1)}$ for the 1D and 2D samples.

(a) (b)

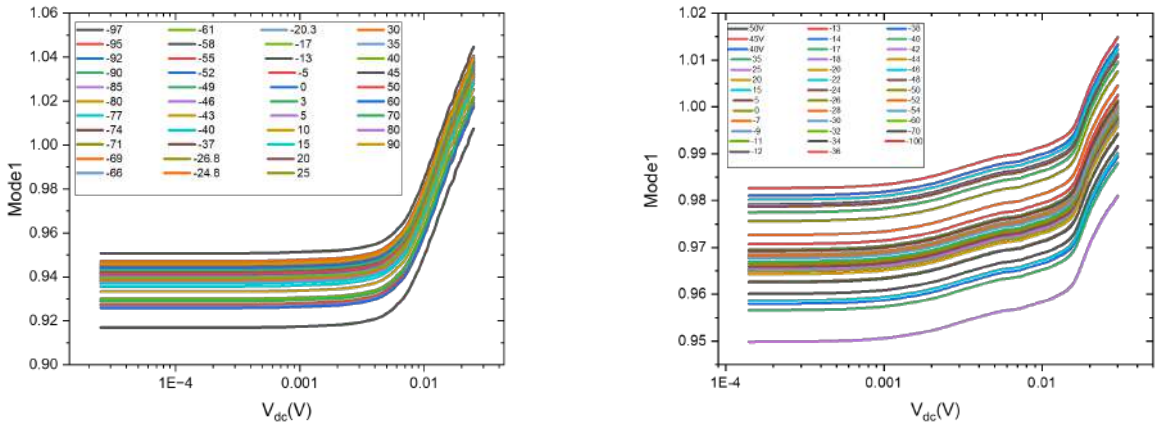

Figure 4.23: The logarithmic increase in the differential conductance reflected in the first modes, indicative of the Altschuler-Aronov (AA) effect, observed in the (a) 1D and (b) 2D samples.

Additionally, while $\vec{V}^{(k=1)}$ captures the fundamental features of the experiment for the 1D sample, it misses notable features observed in the 2D sample, such as the transformation of the minimum at $V_{dc} = 0$ into a maximum for certain values of V_g. An examination of the behavior of $\vec{U}^{(k=1)}$ as a function of V_g reveals a close correlation with the behavior of G, as shown in Figs.

4.16(a) and 4.16(a).

Next we turn to the second mode of the SVD analysis. The mode is plotted in Figs.4.21(b) and 4.22(b). A very clear feature of $\mathbf{X}^{(k=2)}$ of both samples is that distinct regions of behavior are revealed as functions of V_{dc}. All curves cross at two values of $V'_{dc} = \pm 12mV$ for the 1D sample and at $V'_{dc} = \pm 9mV$ for the 2D sample (marked between the two dashed red lines in the figure). These values of V'_{dc} correspond to the estimation of the superconducting gap in these systems, and they are unequivocally revealed by the second mode of the SVD. Considering the simpler 1D, which includes 17 junctions (dots) in series, one can expect to observe structure at $\Delta_{InO} \times 17 = 11.9mV$. Remarkably, this aligns exactly with the point where the curves of the second mode of the 1D sample intersect. For the 2D sample the shortest path across the sample is of 12 junctions, corresponding to $\Delta_{InO} \times 12 = 8.4mV$, not far from the estimation garnered from the width of the second mode.

Furthermore, the 2^{nd} mode offers valuable insights into the superconducting state present in the system across different experimental stages. Both the SC gap width, as revealed by this mode, and the *extremum type* of this mode provide significant information about the system's superconductivity. Upon analyzing the extremum amplitude of the 2^{nd} mode at $V_{dc} = 0$ for each measurement, a distinct crossover, contingent upon V_g, becomes evident. This dependence is depicted on the same graph with the $R(V_g)$ curve of the sample in Fig. 4.24, to discern underlying physical phenomena.

(a) (b)

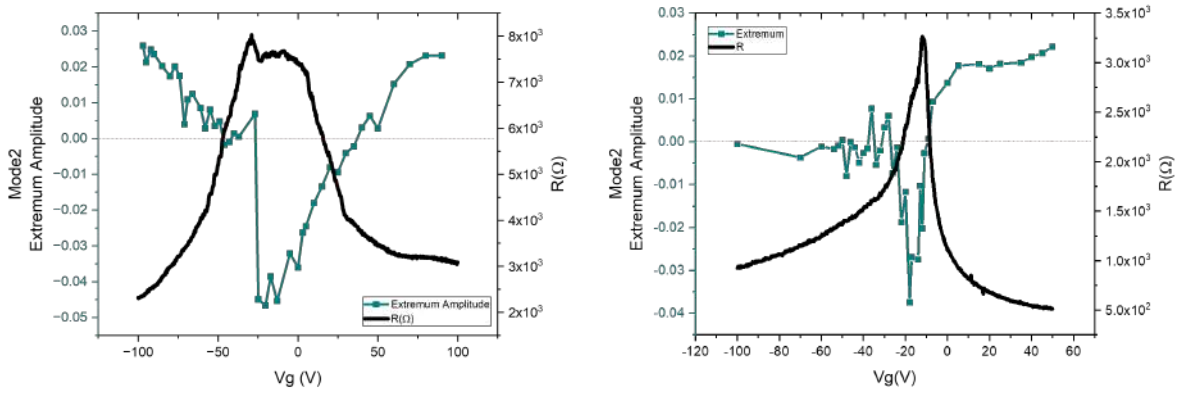

Figure 4.24: Extremum amplitudes of the $2^{nd} SVD$ mode (dotted line) plotted with the device resistance (black line) as a function of V_g. The dashed red line marks the zero baseline, above which points are considered maxima, and below which they are considered minima, of the 1D (a) and the 2D (b) devices. Interestingly, a change in extremum "type" of the 2^{nd} mode is evident at the DP regime.

It is apparent that a distinct trend emerges upon approaching the DP. As the system approaches the vicinity of the DP, a transition occurs from a peak in the 2nd mode amplitude to a dip. This transition reverses as the system progresses to higher V_g values, with the dip transforming back into a peak. Definitely, some change occurring in the vicinity of the DP, at both

1D and 2D devices. To relate this pattern to possible signs of SC in the system, let's examine the dI/dV measurements of the 2D device, presented in Fig. 4.17, where peaks and dips were identified. Taking the dI/dV measurement at $V_g = -20V$ near the DP as an example, it exhibits a peak in the raw dI/dV measurement (indicating a low barrier, Z, condition in the system). This peak corresponds to a dip in the amplitude of the 2nd mode (with respect to the mode's vectors). This suggests that the low Z condition, which is in fact related to V_g, occurs in the proximity of the DP, manifesting as a dip in the 2nd SVD mode. This agrees with the finding mentioned earlier (subsection 4.2.1) that the strongest Josephson coupling, i.e., the lowest Z, between low-n superconducting islands in SLG occurred near the CNP [39].

In the case of the 1D device, although peaks are absent in the dI/dV measurement (Fig.4.16), a similar "flip" in the 2nd mode maxima is observed near the DP (Fig.4.24(a)). It is plausible to propose that a dip in the 2nd mode amplitude could potentially serve as an indicator of low Z state in the system, even in the absence of a peak in the dI/dV measurements. Interestingly, we observed an additional phenomenon associated with the presence of a low Z state in the system. By normalizing the amplitudes of representative oscillations in the *raw* dI/dV data to their maximum (peak or dip) values at each V_g, we identified a discernible trend. As the system approaches the DP, the oscillation amplitude decreases toward zero, resulting in a flat dI/dV curve devoid of oscillations. This trend is illustrated in Fig. 4.25, where the oscillation amplitude normalized to the extremum's value at different V_gs for the 1D device is plotted alongside its corresponding $R(V_g)$ curve. The data shows that as the system nears the DP, the oscillation amplitude decreases (compare to the maxima) and tends toward zero.

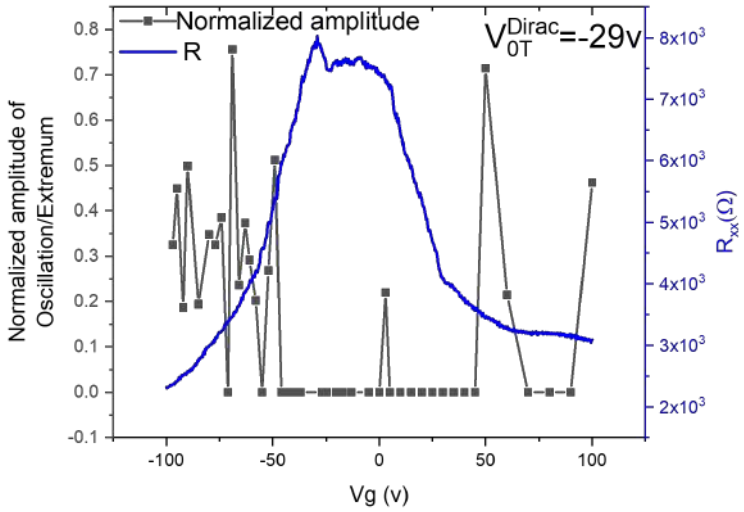

Figure 4.25: $R(V_g)$ and the dI/dVs normalized oscillations amplitude of the 1D device. A flattening of the dI/dV oscillations is evident at the DP regime.

While the source and mechanism of these oscillations are not yet understood, we note that their presence diminishes in the DP regime—characterized by a low Z state— while they are more robust outside of this regime. This decrease in oscillation amplitude in the DP regime

suggests different occurrences affecting the AR processes and their intensity. It may be related to the assertion that superconductivity is most robust in this regime, implying that the graphene barrier is at its lowest there, facilitating tunneling between the SC puddles. This contrasts with stages of the system where the barrier is stronger ($V_g^{Dirac} < |V_g|$, indicating more electron or hole carriers in the graphene inter-media). This stronger barrier may be the key to the different oscillation amplitude, likely accounts for the presence of many scattering events and varied AR processes, which manifest as oscillations in the dI/dV. However, this is only an assumption attempting to explain the observed differences.

The higher modes of the SVD analysis expose two key insights into the differential conductance, evident in the oscillations with respect to V_{dc}. First, we observed that these oscillations seem to exhibit a *different period* within the region of the superconducting gap compared to outside of it. Moreover, this phenomenon is more pronounced for specific values of V_g. As illustrated in Fig. 4.21(c) and Fig. 4.22(c), where one of the typical higher modes ($k = 4$) is presented, (other high modes, such as $k = 3, 5, 6$, show a similar, although somewhat noisier periodicity). It is apparent that the amplitude and frequency of the oscillations differ for $|V_{dc}| < V'_{dc}$ compared to $|V_{dc}| > V'_{dc}$. This suggests that distinct processes may underlie the oscillations inside and outside the gap. For the 1D sample, these frequencies are found to be $2.5mV$ for $|V_{dc}| < V'_{dc}$, inside the superconducting gap, and $1.9mV$ for $|V_{dc}| > V'_{dc}$, outside of it. In the 2D device, which includes multiple dot periodicities, the faster oscillations are averaged out as electronic interference effects are washed out, resulting in much slower oscillations. These longer oscillations are of the order of $10mV$, which fits the scale of the energy gap of the array and are observed outside the DOS energy gap.

Secondly, oscillations are observed both *inside and outside the DOS gap*, prompting further investigation into their origin. The voltage scale associated with these oscillations suggests that they might arise from electronic interference effects linked to the dot periodicity, pointing to a characteristic length scale in the system. Using the linear dispersion relation with respect to momentum, $\Delta P = \dfrac{\Delta\epsilon}{V_F}$, and the relation $\Delta P \cdot l = 2\pi\hbar$, we find $l = \dfrac{2\pi\hbar V_F}{\Delta\epsilon}$. In the 1D device, for $\Delta V = 2.5mV$ outside the DOS gap, converting to energy terms using $V = \dfrac{E}{q}$, we obtain $\Delta\epsilon = 4 \times 10^{-22}J$. Substituting into the equation yields $l \approx 6\mu m$. Since we attribute these oscillations to different AR processes between the dots, it is reasonable to divide this distance by 2 (considering both forward and backward processes), resulting in $l \approx 3\mu m$, a scale comparable to the dot size of $1\mu m$.

Had we only observed oscillations outside the DOS gap, several theoretical approaches could have been explored, such as electronic interference effects and reflection patterns based on NSN junctions- a theory discussed in the subsequent sub-section. While these calculations do not quantitatively align with our data, they would have provided a plausible direction for further investigation. However, a significant challenge arises with the oscillations observed *within* the DOS gap, which are particularly puzzling. For $\epsilon < \Delta$, an incident electronic wave should decay rapidly inside the superconductor, preventing propagation and thus the formation of oscillations. Alternatively, due to the Klein paradox, such oscillations should not exist, as the wave might

pass through with a probability of 1, also leading to an absence of oscillations. So far, we have not found a satisfactory theory or explanation for these oscillations, leaving this phenomenon unresolved.

Possible explanations might involve the unique characteristics of the BM exotic phase in our device and, or, the electronic-granular nature of our InO superconducting material. The exact origin of the oscillations within the gap remains unclear, and further experimental and theoretical research is needed to resolve this mystery.

This unknown oscillatory behavior within the DOS gap is part of a broader set of unresolved questions: Why is there a difference in the periodicity between oscillations inside and outside the DOS gap? And why does the periodicity appear smaller outside the DOS gap compared to inside it? These questions, too, remain unanswered.

While the significance of these observations is still unclear, the next subsection (4.2.5) presents a theoretical model that may shed light on some of the oscillations observed experimentally, particularly in the 2D system.

To conclude, we observed distinct oscillation patterns in the $\frac{dI}{dV}$ measurements of 1D and 2D dot arrays. The 1D dot-row exhibited faster oscillations both inside and outside the DOS gap, whereas the 2D dot-matrix showed slower oscillations, primarily outside the DOS gap. We attribute these disparities to the averaging of AR processes, as the 2D sample allows multiple trajectories for the oscillations to accumulate. Unlike the single-series dot trajectory in the 1D sample, it is less clear how the oscillations are formed and how the barrier affects them in the 2D configuration.

We utilized the strength of the SVD technique, to assist in analyzing complex physics experimental data, by successfully reducing the dimensionality while preserving crucial information. We found that the SV amplitudes and the different modes unveil valuable insights of real physics properties, by effectively separate and highlight distinct physical mechanisms that construct the results, which were otherwise difficult to isolate;

- The 1^{st} mode of the SVD provides insight into the overall common behavior, representing the AA background of the data.
- The 2^{nd} mode effectively extracts information about the superconductivity gap width and the extremum type of the $\frac{dI}{dV}$ curve, suggesting a difference occurring at the DP regime.
- The higher modes (usually third to sixth) capture the oscillation pattern of the data, which differs for energies inside and outside the SC gap.

The 1D device, where only one trajectory is available, provided insight into the physical implications of SVD analysis and the physics underlying the fundamental building blocks of Bosonic phases. We were able to extract Δ_{InO} by analyzing the region between the crossover points of the SVD 2nd mode curves and dividing it by the number of junctions. This allowed us to conclude that the region between these points represents the DOS gap of the system. Moreover, due to the singular trajectory passing through a number of junctions in series, pronounced oscillations with varying periodicities were observed, both within and outside the DOS gap, on

at scales of $2.5mV$ and $2mV$ respectively. This fits the scale for electronic interference effects due to the dot periodicity of $\approx 3\mu m$.

In contrast, the 2D device offers multiple trajectory options for current flow, making it challenging to pinpoint the exact SC gap from the SVD analysis since the precise path of the current is unknown. Additionally and most importantly, the multiple trajectories likely average out the oscillations, resulting in fewer oscillations per V_g and a larger voltage periodicity.

Furthermore, dI/dV measurements of the 1D device showed only dips, whereas the 2D device exhibited both dips and peaks. A peak indicates a strong coupling between grains, while a dip suggests a weaker coupling. This discrepancy can be attributed to the difference in the barrier strength and its 'weight' in the 1D device, where a single trajectory is accessible, compared to the 2D device with multiple trajectories. Both devices displayed a variety of dI/dV shapes, including intermediate forms between peaks and dips, whose origins are not fully understood yet.

The differences in dI/dV measurements between the 1D and 2D devices seem to arise from variations in the number of current flow trajectories, highlighting the importance of junction structure and path as critical factors influencing the experimental outcomes, particularly in relation to our understanding of the BM phase and its microscopic mechanisms. While we do not yet have a satisfactory explanation for the oscillation patterns, primarily observed in the 1D sample, it can be speculated that these patterns may be linked to fundamental mechanisms within the BM phase.

Oscillatory behavior was observed in both the $R(V_g)$ and $\frac{dI}{dV}$ measurements. We demonstrated that the periodicity of the $R(V_g)$ oscillations corresponds to an **intrinsic** length scale of a few tens of nanometers, which we propose is related to the emergent granularity of the InO and the Josephson coupling between its electronic grains. On the other hand, the periodicity of the $\frac{dI}{dV}$ oscillations suggests the presence of various AR processes between the dots. This periodicity corresponds to a larger length scale of approximately $3\mu m$, which is not fully understood but is on the same order as the dot size of $1\mu m$.

These two different length scales, originating from different regions within the superconducting system, have been shown to play significant roles in determining the system's superconducting properties [75].

4.2.5 Preliminary theoretical work

The SNS model of a Josephson junction was explored in the work of Beenakker et al. [76], particularly in cases where graphene serves as the normal region [77]. However, this model was solved for short junctions, where one of the key assumptions is that the length of the normal region (L_N) is significantly smaller than both W and ξ, where W represents the width of the SC region and ξ denotes the SC coherence length. In this model, the system is predominantly a strong superconductor, with a measurable supercurrent unit. However, this is not our case. In our scenario, we have a metallic device, with $L_N = 200nm$ (the interdot distance), $W = 1\mu m$ (the dot diameter), and $\xi_{InO} \approx 5 - 30nm$. Thus, our system does not fall within the short junction regime, nor is it fully SC with a critical current, necessitating a different model.

Theoretical efforts to model the behavior of our system have been initiated in collaboration with Prof. Shimshoni's theoretical group, where Khanna leads the effort. Calculations were performed using the SNS Josephson junction model, focusing on the long junction limit where $L_N > \xi$. However, no oscillations were observed using this model, as it does not accurately capture the nature of our system, which is characterized by predominantly normal (N) regions rather than SC ones. Therefore, a model of **NSN** "unit cell" chain was considered, with $\Delta = 0.7meV$ (that of InO), and $V_F = 10^6 m/s$ (the velocity in graphene). In this case, they found that $\frac{\hbar V_F}{\Delta} \approx 1\mu m$, which fit our system, with $L_S = 1\mu m$, our SC InO dot diameter (with $L_N = 200nm$, the inter dot distance), where L_S is the SC region length (similarly to the notation of L_N). Therefore, L_S was considered to be $O(1)$ in the units of $\frac{\hbar V_F}{\Delta}$. For numerical considerations $L_S\Delta$ was set to 3. E_F in the induced SC regions in the graphene is noted as E'_F and equals to $E'_F = E_F + U$, where U is the energy shift, arising from the difference in the electrostatic potential induced by the superconducting InO [39, 40]. This U was found to be much larger than Δ [39], leading to its arbitrary selection as $U = -50\Delta$ in the calculations.

The preliminary results shown in Fig. 4.26 present the normalized differential conductance for different E_F values versus the bias energy (ϵ) applied to the system (V_{dc} in the experiment). These results were provided through personal communication with Khanna, who conducted the full theoretical calculations, which are available upon request. In the first panel (Fig. 4.26(a)), the model's results are displayed for a wide range of E_F (V_gs). The curves exhibit broad minima around similar bias values for all E_F values. The position of this minima was found to be $\sqrt{1 + (\frac{\pi}{L_S\Delta})^2}$ (indicated by dashed lines in the figures), considering normal incident conditions. This model successfully produces oscillations with a periodicity that depends on $\frac{\pi}{L_S\Delta}$). Notably, different choices of $L_S\Delta$ (other than 3, as noted) would result in different locations of the minima and varying oscillation periodicities. However, it is observed that these oscillations are occur in energy regimes *outside* the DOS gap (when $1 < \frac{\epsilon}{\Delta}$) for all E_F values, which may correspond to our experimental results in the 2D device, where oscillations in the SVD analysis were primarily observed outside the DOS gap and at a similar order of Δ. Nonetheless, this does not fully align with the *raw* data, which showed oscillations within the DOS gap in both 1D and 2D devices, occurring at different bias voltage ranges depending on V_g.

Figs. 4.26(b) and (c) depict the same results for a narrower range of E_F values, centered around the DP and the SDP, respectively. Around the DP, oscillations *within* the DOS gap

may begin to appear for certain E_F values. As for around the SDP, the oscillations only appear outside the DOS gap; however, the curves are not as smooth as those in Fig. 4.26(a), exhibiting what seems to be a faster periodicity superimposed on the overall pattern.

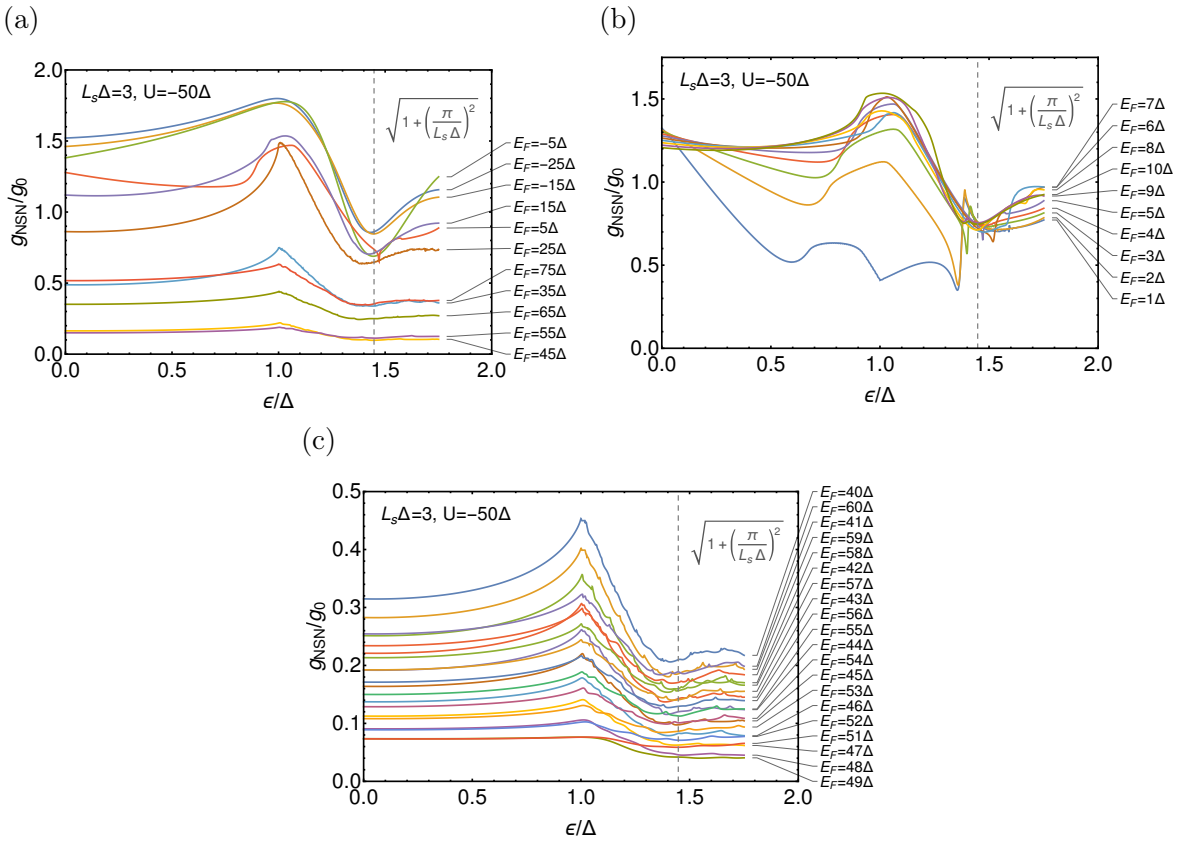

Figure 4.26: Normalized differential conductance vs bias for a NSN setup for different Fermi levels in the normal region. (a) shows the conductance over a broad range of E_F, (b) focuses on values close to the DP, and (c) on those near the SDP. The dashed curve marks the bias at which a minimum of the conductance is expected in case of normal incidence. Data taken from the full theoretical calculations by Khanna, available upon request from the author.

This model successfully reproduced oscillations *outside* the DOS gap, which is a promising start in modulating our experimental system, where oscillations appear at different V_{dc} values-both outside and inside the DOS gap. However, this is only the beginning. Ongoing simulations are underway to incorporate additional parameters such as higher V_{dc}, the system's finite size, and different incident angles, to more precisely modulate the experimental system. Further research, both experimental and theoretical, is essential to fully comprehend these oscillations in dI/dV, their driving mechanisms, and the insights they provide into Bose phases.

Chapter 5

Summary and outlook

This dissertation investigates the bosonic phases that emerge in disordered granular superconductors undergoing the superconductor-to-insulator transition (SIT) using two novel approaches. The primary aim is to contribute to the understanding of these bosonic phases during the transition. The key contributions and conclusions of this research are as follows:

The thermodynamic study of the **specific heat** of granular ultra-thin In films undergoing the SIT yielded novel findings, particularly regarding the possibility of a Bose metal (BM) phase. Intermediate thickness films exhibited a BM behavior, with $R(T)$ curves saturating at low temperatures. These films displayed a distinct C_p behavior with **two** notable features, leading to excess entropy. The main striking finding was the revelation of a sharp jump in C_p observed at intermediate thicknesses, occurring between the insulating and superconducting phases during the transition. This feature suggests complex thermodynamic behavior, including strong quantum fluctuations and additional thermodynamic states or degrees of freedom, potentially indicating a second phase transition within the material.

Additionally, a Bose insulator phase was identified in the system, evidenced by a peak in C_p in thin insulating films, confirming the persistence of superconductivity in an insulating state.

Furthermore, change in β and the slope of C_p were observed, indicating variations in the dominant heat carriers across different film thicknesses. This suggests significant changes in the underlying physics governing heat transport near the SIT, possibly due to alterations in electronic and phononic contributions.

Specific heat measurements have not previously identified this second feature in systems undergoing the SIT. We believe that this finding, along with our other results, would be essential for advancing the understanding of the SIT and other quantum phase transitions (QPTs). The nature of this feature remains unknown, as it deviates from current theories and established C_p behaviors. Further theoretical and experimental investigations are necessary to fully elucidate these phenomena. For instance, specific heat measurements on other high θ_D thin-layer superconductors undergoing the SIT could provide valuable insights.

In the second approach, we investigated the **transport** properties of engineered SC InO dot matrices on SLG, analyzing both 1D single dot rows and 2D dot matrices. Fluctuations

were observed in the $R(V_g)$ measurements, while oscillatory behavior appeared in the $\frac{dI}{dV}$ measurements. The fluctuations in $R(V_g)$ corresponded to an internal length scale of a few tens of nanometers, associated with the emergent granularity of InO and the ξ_{pair} length. The $\frac{dI}{dV}$ oscillations matched a larger length scale of few μm.

Differences in dI/dV measurements between the 1D and 2D dot arrays were observed. The 1D dot row exhibited faster oscillations compared to the slower oscillations in the 2D matrix, attributed to the averaging of AR processes in the 2D configuration, which allows multiple current paths, unlike the single path in the 1D case.

Using SVD, we gained valuable insights into physical properties by separating and highlighting distinct physical mechanisms. For the 1D device, SVD revealed a DOS gap, Δ_{InO}, by examining the region between crossover points of the SVD 2nd mode curves. Oscillations with periods of $2.5mV$ and $2mV$ were correlated with a length scale of approximately $3\mu m$, which is associated with AR between two dots. In the 2D device, multiple trajectories and averaging effects made it difficult to determine the SC gap precisely, leading to fewer and broader oscillations in dI/dV. The 1D device showed only dips in dI/dV, while the 2D device exhibited both dips and peaks, likely due to the differing number of current paths and barrier strengths.

Attributing these disparities in dI/dV measurements to variations in the number of current trajectories underscores the importance of path and junction construction in influencing experimental outcomes, particularly in understanding the BM phase and its microscopic mechanisms. While the exact nature of the oscillation patterns remains unclear, we believe they may relate to fundamental mechanisms in the Bose phases.

Further experiments on various SC materials, dot sizes, and varied inter-dot distances hold the potential to deepen our understanding of the mechanisms controlling the Bose phases and the observed oscillations. Performing these measurements on additional 1D and 2D matrices with varied dot sizes and inter-dot distances can help determine if the oscillation pattern changes as hypothesized. Repeating these experiments with different SC materials, especially in the 1D configuration, will ascertain if the observed oscillatory behavior is specific to low n SC coupled to SLG or occurs in other materials as well. Another research direction could involve achieving the BM phase in N-S dot matrix configurations and controlling their coupling through different methodologies, such as evaporating thin layers using quench condensation technique. This approach could broaden our understanding of the underlying physics and the nature of these oscillations, determining whether they are specific to the unique characteristics of SLG, low n SC, or other factors.

Overall, the findings from our investigations revealed intriguing thermodynamic signatures and insights into the electrical characteristics of the building blocks of bosonic phases. Together, both the thermodynamic and the transport measurements, highlighted the complex behaviors and phenomena of the Bosonic phases, contributing to a deeper understanding of the electrical dynamics and mechanisms within disordered granular superconductor systems. This combined perspective shed light on bosonic phases from different angles, providing a broader view that advanced our understanding of the fundamental questions surrounding these phases and paved the way for future inquiries and advancements in quantum condensed matter physics.

Bibliography

[1]S.-Y. Hsu and J. Valles Jr, "Magnetic-field-induced pair-breaking effects in granular pb films near the superconductor-to-insulator transition", Physical Review B **48**, 4164 (1993).

[2]Y.-H. Lin, J. Nelson, and A. Goldman, "Superconductivity of very thin films: the superconductor–insulator transition", Physica C: Superconductivity and its Applications **514**, Superconducting Materials: Conventional, Unconventional and Undetermined, 130–141 (2015).

[3]A. Frydman, "The superconductor insulator transition in systems of ultrasmall grains", Physica C: Superconductivity **391**, 189–195 (2003).

[4]D. Haviland, Y. Liu, and A. M. Goldman, "Onset of superconductivity in the two-dimensional limit", Physical Review Letters **62**, 2180 (1989).

[5]M. Strongin, R. Thompson, O. Kammerer, and J. Crow, "Destruction of superconductivity in disordered near-monolayer films", Physical Review B **1**, 1078 (1970).

[6]A. Frydman, O. Naaman, and R. Dynes, "Universal transport in two-dimensional granular superconductors", Physical Review B **66**, 052509 (2002).

[7]S. M. Hollen, H. Nguyen, E. Rudisaile, M. Stewart Jr, J. Shainline, J. Xu, and J. Valles Jr, "Cooper-pair insulator phase in superconducting amorphous bi films induced by nanometer-scale thickness variations", Physical Review B—Condensed Matter and Materials Physics **84**, 064528 (2011).

[8]A. Hebard and M. Paalanen, "Magnetic-field-tuned superconductor-insulator transition in two-dimensional films", Physical review letters **65**, 927 (1990).

[9]A. Yazdani and A. Kapitulnik, "Superconducting-insulating transition in two-dimensional a-moge thin films", Physical review letters **74**, 3037 (1995).

[10]N. Marković, C. Christiansen, A. Mack, W. Huber, and A. Goldman, "Superconductor-insulator transition in two dimensions", Physical Review B **60**, 4320 (1999).

[11]A. Johansson, I. Shammass, N. Stander, E. Peled, G. Sambandamurthy, and D. Shahar, "Angular dependence of the magnetic-field driven superconductor–insulator transition in thin films of amorphous indium-oxide", Solid State Communications **151**, 743–746 (2011).

[12]A. T. Bollinger, G. Dubuis, J. Yoon, D. Pavuna, J. Misewich, and I. Božović, "Superconductor–insulator transition in la2- x sr x cuo4 at the pair quantum resistance", Nature **472**, 458–460 (2011).

[13]K. A. Parendo, K. S. B. Tan, A. Bhattacharya, M. Eblen-Zayas, N. Staley, and A. Goldman, "Electrostatic tuning of the superconductor-insulator transition in two dimensions", Physical review letters **94**, 197004 (2005).

[14]A. Caviglia, S. Gariglio, N. Reyren, D. Jaccard, T. Schneider, M. Gabay, S. Thiel, G. Hammerl, J. Mannhart, and J.-M. Triscone, "Electric field control of the laalo3/srtio3 interface ground state", Nature **456**, 624–627 (2008).

[15]O. Crauste, F. Couedo, L. Bergé, C. Marrache, and L. Dumoulin, "Superconductor-insulator transition in amorphous nbxsi1- x thin films. comparison between thickness, density of state and microscopic disorder.", in Journal of physics: conference series, Vol. 400, 2 (IOP Publishing, 2012), p. 022012.

[16]M. P. Fisher, G. Grinstein, and S. Girvin, "Presence of quantum diffusion in two dimensions: universal resistance at the superconductor-insulator transition", Physical review letters **64**, 587 (1990).

[17]N. Trivedi, Y. L. Loh, K. Bouadim, and M. Randeria, "Emergent granularity and pseudogap near the superconductor-insulator transition", in Journal of physics: conference series, Vol. 376, 1 (IOP Publishing, 2012), p. 012001.

[18]D. Kowal and Z. Ovadyahu, "Disorder induced granularity in an amorphous superconductor", Solid state communications **90**, 783–786 (1994).

[19]D. Sherman, G. Kopnov, D. Shahar, and A. Frydman, "Measurement of a superconducting energy gap in a homogeneously amorphous insulator", Physical review letters **108**, 177006 (2012).

[20]D. Sherman, B. Gorshunov, S. Poran, N. Trivedi, E. Farber, M. Dressel, and A. Frydman, "Effect of coulomb interactions on the disorder-driven superconductor-insulator transition", Physical Review B **89**, 035149 (2014).

[21]K. Bouadim, Y. L. Loh, M. Randeria, and N. Trivedi, "Single-and two-particle energy gaps across the disorder-driven superconductor–insulator transition", Nature Physics **7**, 884–889 (2011).

[22]H. Jaeger, D. Haviland, B. Orr, and A. Goldman, "Onset of superconductivity in ultrathin granular metal films", Physical Review B **40**, 182 (1989).

[23]A. Kapitulnik, S. A. Kivelson, and B. Spivak, "Colloquium: anomalous metals: failed superconductors", Reviews of Modern Physics **91**, 011002 (2019).

[24]B. Spivak, P. Oreto, and S. Kivelson, "Theory of quantum metal to superconductor transitions in highly conducting systems", Physical Review B—Condensed Matter and Materials Physics **77**, 214523 (2008).

[25]I. Tamir, A. Benyamini, E. Telford, F. Gorniaczyk, A. Doron, T. Levinson, D. Wang, F. Gay, B. Sacépé, J. Hone, et al., "Extreme sensitivity of the superconducting state in thin films", arXiv preprint arXiv:1804.04648 (2018).

[26]E. Abrahams, P. W. Anderson, D. C. Licciardello, and T. V. Ramakrishnan, "Scaling theory of localization: absence of quantum diffusion in two dimensions", Phys. Rev. Lett. **42**, 673–676 (1979).

[27]P. Phillips and D. Dalidovich, "The elusive bose metal", Science **302**, 243–247 (2003).

[28]M. V. Feigel'man, A. I. Larkin, and M. A. Skvortsov, "Quantum superconductor–metal transition in a proximity array", Physics-Uspekhi **44**, 99 (2001).

[29]B. Spivak, A. Zyuzin, and M. Hruska, "Quantum superconductor-metal transition", Phys. Rev. B **64**, 132502 (2001).

[30]E. Shimshoni, A. Auerbach, and A. Kapitulnik, "Transport through quantum melts", Phys. Rev. Lett. **80**, 3352–3355 (1998).

[31]A. Kapitulnik, N. Mason, S. A. Kivelson, and S. Chakravarty, "Effects of dissipation on quantum phase transitions", Physical Review B **63**, 125322 (2001).

[32]D. Dalidovich and P. Phillips, "Phase glass is a bose metal: a new conducting state in two dimensions", Physical review letters **89**, 027001 (2002).

[33]P. Debye, "Theory of specific heats", An. Physik **39**, 784–839 (1912).

[34]A. M. Boring and J. L. Smith, "Plutonium condensed-matter physics", Los Alamos Science **26**, 90 (2000).

[35]S. Poran, T. Nguyen-Duc, A. Auerbach, N. Dupuis, A. Frydman, and O. Bourgeois, "Quantum criticality at the superconductor-insulator transition revealed by specific heat measurements", Nature communications **8**, 14464 (2017).

[36]A. Allain, Z. Han, and V. Bouchiat, "Electrical control of the superconducting-to-insulating transition in graphene–metal hybrids", Nature materials **11**, 590–594 (2012).

[37]Z. Han, A. Allain, H. Arjmandi-Tash, K. Tikhonov, M. Feigel'Man, B. Sacépé, and V. Bouchiat, "Collapse of superconductivity in a hybrid tin–graphene josephson junction array", Nature Physics **10**, 380–386 (2014).

[38]C. Bøttcher, F. Nichele, M. Kjaergaard, H. Suominen, J. Shabani, C. Palmstrøm, and C. Marcus, "Superconducting, insulating and anomalous metallic regimes in a gated two-dimensional semiconductor–superconductor array", Nature Physics **14**, 1138–1144 (2018).

[39]G. N. Daptary, E. Walach, E. Shimshoni, and A. Frydman, "Superconducting dirac point in proximetized graphene", arXiv preprint arXiv:2009.14603 (2020).

[40]G. N. Daptary, U. Khanna, E. Walach, A. Roy, E. Shimshoni, and A. Frydman, "Enhancement of superconductivity upon reduction of carrier density in proximitized graphene", Physical Review B **105**, L100507 (2022).

[41]A. Andreev et al., "Thermal conductivity of the intermediate state of superconductors ii", Sov. Phys. JETP **20**, 1490 (1965).

[42]G. Blonder, m. M. Tinkham, and T. Klapwijk, "Transition from metallic to tunneling regimes in superconducting microconstrictions: excess current, charge imbalance, and supercurrent conversion", Physical Review B **25**, 4515 (1982).

[43]M. I. Katsnelson, K. S. Novoselov, and A. K. Geim, "Chiral tunnelling and the klein paradox in graphene", Nature physics **2**, 620–625 (2006).

[44]N. Stander, B. Huard, and D. Goldhaber-Gordon, "Evidence for klein tunneling in graphene p-n junctions", Physical review letters **102**, 026807 (2009).

[45]C. Beenakker, "Specular andreev reflection in graphene", Physical review letters **97**, 067007 (2006).

[46]D. K. Efetov and K. B. Efetov, "Crossover from retro to specular andreev reflections in bilayer graphene", Physical Review B **94**, 075403 (2016).

[47]D. K. Efetov, L. Wang, C. Handschin, K. Efetov, J. Shuang, R. Cava, T. Taniguchi, K. Watanabe, J. Hone, C. Dean, et al., "Specular interband andreev reflections at van der waals interfaces between graphene and nbse 2", Nature Physics **12**, 328–332 (2016).

[48]S. Poran, M. Molina-Ruiz, A. Gérardin, A. Frydman, and O. Bourgeois, "Specific heat measurement set-up for quench condensed thin superconducting films", Review of Scientific Instruments **85** (2014).

[49]P. F. Sullivan and G. Seidel, "Steady-state, ac-temperature calorimetry", Physical Review **173**, 679 (1968).

[50]L. Steele, G. Iannacchione, and D. Finotello, "Ac calorimetry technique. aplications to liquid helium films and liquid crystals", Revista Mexicana de Física **39**, 588–601 (1992).

[51]O. Bourgeois, "Heat transfer in low temperature micro- and nanosystems", in *Thermal nanosystems and nanomaterials*, edited by S. Volz (Springer Berlin Heidelberg, Berlin, Heidelberg, 2009), pp. 537–567.

[52]M. Wall, "The raman spectroscopy of graphene and the determination of layer thickness", Thermo Sci **5**, 1–5 (2011).

[53]Z. Ovadyahu, "Some finite temperature aspects of the anderson transition", Journal of Physics C: Solid State Physics **19**, 5187 (1986).

[54]N. A. Lewellyn, I. M. Percher, J. Nelson, J. Garcia-Barriocanal, I. Volotsenko, A. Frydman, T. Vojta, and A. M. Goldman, "Quantum superconductor-metal transitions in the presence of quenched disorder", Journal of Superconductivity and Novel Magnetism **33**, 183–190 (2020).

[55]D. Sherman, G. Kopnov, D. Shahar, and A. Frydman, "Measurement of a superconducting energy gap in a homogeneously amorphous insulator", Physical review letters **108**, 177006 (2012).

[56]A. Roy, E. Shimshoni, and A. Frydman, "Quantum criticality at the superconductor-insulator transition probed by the nernst effect", Physical review letters **121**, 047003 (2018).

[57]T. Nguyen, A. Frydman, and O. Bourgeois, "Specific heat signature of the berezinskii-kosterlitz-thouless transition in ultrathin superconducting films", arXiv preprint arXiv:1908.00729 (2019).

[58]M. Tinkham, *Introduction to superconductivity*, Vol. 1 (Courier Corporation, 2004).

[59]C. Bryant and P. Keesom, "Low-temperature specific heat of indium and tin", Physical Review **123**, 491 (1961).

[60]H. G. E. Hentschel, V. Ilyin, I. Procaccia, and N. Schupper, "Theory of specific heat in glass-forming systems", Physical Review E **78**, 10.1103/physreve.78.061504 (2008).

[61]W. P. Ke Hai-Bo Zhao Zuo-Feng and W. Wei-Hua, "Specific heat in a typical metallic glass former", Chinese Physics Letters **29**, 046402 (2012).

[62]J.-L. Garden, A. Tavakoli, T. Nguyen-Duc, A. Frydman, M. Laarraj, J. Richard, and O. Bourgeois, "Very Sensitive Nanocalorimetry of Small Mass Systems and Glassy Materials", in *Nanomaterials for Security*, edited by S. K. Janez Bonča (Springer, 2016), pp. 35–44.

[63]B. Sacépé, J. Seidemann, M. Ovadia, I. Tamir, D. Shahar, C. Chapelier, C. Strunk, and B. A. Piot, "High-field termination of a cooper-pair insulator", Phys. Rev. B **91**, 220508 (2015).

[64]B. Al'Tshuler, A. Aronov, and B. Spivak, "The aaronov-bohm effect in disordered conductors", Jetp Lett **33**, 94 (1981).

[65]A. Johansson, G. Sambandamurthy, D. Shahar, N. Jacobson, and R. Tenne, "Nanowire acting as a superconducting quantum interference device", Phys. Rev. Lett. **95**, 116805 (2005).

[66]B. L. Altshuler and A. G. Aronov, "Electron–electron interaction in disordered conductors", in *Modern problems in condensed matter sciences*, Vol. 10 (Elsevier, 1985), pp. 1–153.

[67]J. F. Stein, A. Frydman, and R. Berkovits, "Unraveling complexity: Singular value decomposition in complex experimental data analysis", SciPost Phys. Core **7**, 061 (2024).

[68]M. L. Fowler, M. Chen, J. A. Johnson, and Z. Zhou, "Data compression using svd and fisher information for radar emitter location", Signal processing **90**, 2190–2202 (2010).

[69]N. Benjamin Erichson, S. L. Brunton, and J. Nathan Kutz, "Compressed singular value decomposition for image and video processing", in Proceedings of the ieee international conference on computer vision workshops (2017), pp. 1880–1888.

[70]R. D. Badger and M. Kim, "Singular value decomposition for compression of large-scale radio frequency signals", in 2021 29th european signal processing conference (eusipco) (IEEE, 2021), pp. 1591–1595.

[71]S. Xu, J. Zhang, L. Bo, H. Li, H. Zhang, Z. Zhong, and D. Yuan, "Singular vector sparse reconstruction for image compression", Computers & Electrical Engineering **91**, 107069 (2021).

[72]Y. Wang and L. Zhu, "Research and implementation of svd in machine learning", in 2017 ieee/acis 16th international conference on computer and information science (icis) (IEEE, 2017), pp. 471–475.

[73]P. Díaz-Morales, A. Corrochano, M. López-Martín, and S. Le Clainche, "Deep learning combined with singular value decomposition to reconstruct databases in fluid dynamics", Expert Systems with Applications **238**, 121924 (2024).

[74]R. Berkovits, "Super-poissonian behavior of the rosenzweig-porter model in the nonergodic extended regime", Physical Review B **102**, 165140 (2020).

[75]A. Kremen, H. Khan, Y. Loh, T. Baturina, N. Trivedi, A. Frydman, and B. Kalisky, "Imaging quantum fluctuations near criticality", Nature physics **14**, 1205–1210 (2018).

[76]C. W. J. Beenakker, "Three "universal" mesoscopic josephson effects", in Transport phenomena in mesoscopic systems, edited by H. Fukuyama and T. Ando (1992), pp. 235–253.

[77]M. Titov and C. W. Beenakker, "Josephson effect in ballistic graphene", Physical Review B—Condensed Matter and Materials Physics **74**, 041401 (2006).

[78]P. Townsend and J. Sutton, "Investigation by electron tunneling of the superconducting energy gaps in nb, ta, sn, and pb", Phys. Rev. **128**, 591–595 (1962).

Appendix A

Specific heat measurements of ultra-thin layers of silver

In an effort to isolate the contribution of superconductivity and gain further insights, we chose to investigate a normal metal, silver (Ag), undergoing an insulator-to-metal transition (MIT). This complementary study provided additional context and comparative baseline data to enhance our understanding of the thermodynamic behavior of granular disordered systems. Silver was chosen due to its high θ_D value of $\theta_D^{Ag} = 227.3K$, significantly higher than that of previously studied $Pb(88K)$ and than that of $In(129K)$. This ensures a minimized phononic contribution, thereby enabling the observation of electronic behavior within the system.

11 steps of quench-condensed Ag films were studied, using the same techniques and measurement protocol as those employed in the In experiment (following the protocol outlined in Chapter3.1.3).

To explore potential variations in heat transfer across different morphologies within the same system, the first layer underwent two measurements: initially in its amorphous phase, attained by depositing it on an antimony adhesion layer and maintaining the system under $20K$. Subsequently, it was measured as a crystalline layer, acquired by heating the system to room temperature (and then re-cool it).

By utilizing equation 1.1, we can gain insight into the predominant heat carriers of C_p through analysis of the slope exhibited in the $\log(C_p)$ versus $\log(T)$ curve. A slope of 1 would suggest dominance by electrons, while a slope of 3 would indicate dominance by phonons. This analysis of the first layer is depicted in Fig. A.1. Noticeably, the slope changed from 3 in the amorphous phase to approximately 1 in the crystalline phase. This observation suggests that phonons govern heat transfer in disordered, i.e. amorphous, state of a system while electrons emerge as the dominant carriers in the ordered, i.e. crystalline, state of a system. This outcome is rather unexpected, as electron dominance at low temperatures is theoretically predicted regardless of the system's morphology. The emergence of this finding within a material with a high θ_D underscores the importance of selecting such materials when studying the amorphous state to enable the detection of electronic heat carriers' behaviors in disordered systems. If phonons govern heat transfer in the amorphous state of high θ_D materials, it would be even more challenging to

observe electronic effects in low θ_D materials. Therefore, choosing high θ_D materials is crucial for studying electronic behaviors, as it provides the best chance of detecting them.

An additional surprising finding is the observed change in the absolute value of the C_p signal between the two morphologies. After crystallization, the absolute value of C_p is higher, indicating that the crystalline morphology can retain more heat than the amorphous one. This phenomenon requires further explanation, as one might logically expect a system dominated by phonons, which possess three degrees of freedom, to exhibit a larger C_p value compared to one dominated by electrons, which have only one degree of freedom.

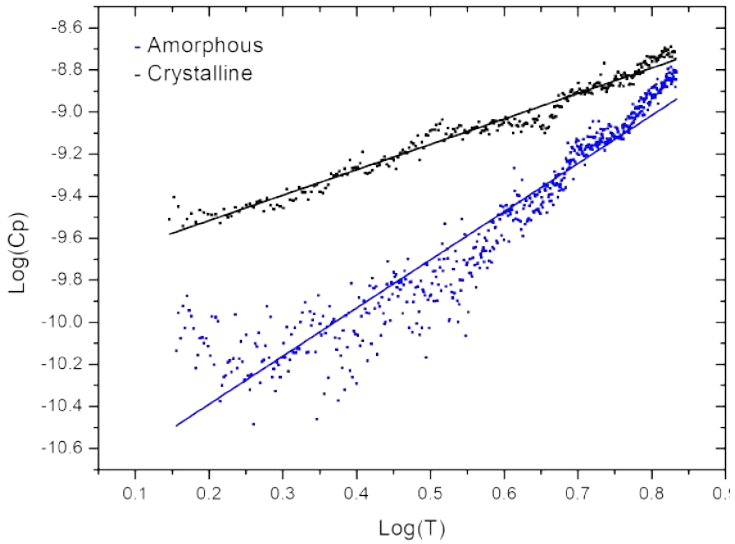

Figure A.1: Log(C_p) vs Log(T) of the 1^{st} nano-thick-Ag layer before (blue) and after (black) crystallization. Solid lines represent the matching slopes. The slope changed from 3 to ≈ 1, indicating the shift in the ruling heat carriers.

This measurement revealed a shift in the dominance heat carriers as the morphology of the system changed, emphasizing the important role of phonons in heat transport within disordered systems. This underscores the importance of investigating disordered materials with low Debye temperatures to observe electronic behaviors in such systems.

Sequential evaporations were performed onto the crystalline 1st layer (growing as crystallized layers), while the system temperature maintained under $25K$. Both $R(T)$ and C_p measurements were taken for each step. The system exhibited an Insulator-to-Metal transition (MIT) as a function of thickness. As the layer thickness increased, the resistance decreased. Eventually, the sample transformed from being a strong insulator with $R \approx 10^8\Omega$ to a normal metal with a resistance of a few tens of ohms at the final step. This transition is illustrated in Fig. A.2(a), where $logR$ vs $1/T^{0.5}$ curves for the various steps are plotted. This representation highlights the Mott behavior of the system. The corresponding C_p measurements are presented in Fig. A.2(b), using the same color code.

In a similar manner to the In experiment, we analyzed the reduced C_p to elucidate the prevalence of heat carriers. The $\frac{C_p}{T}$ vs T^2 curves are depicted in Fig. A.3.

Chosen steps are depicted in Fig. A.3(b), where their raw data is presented with linear

(a) (b)

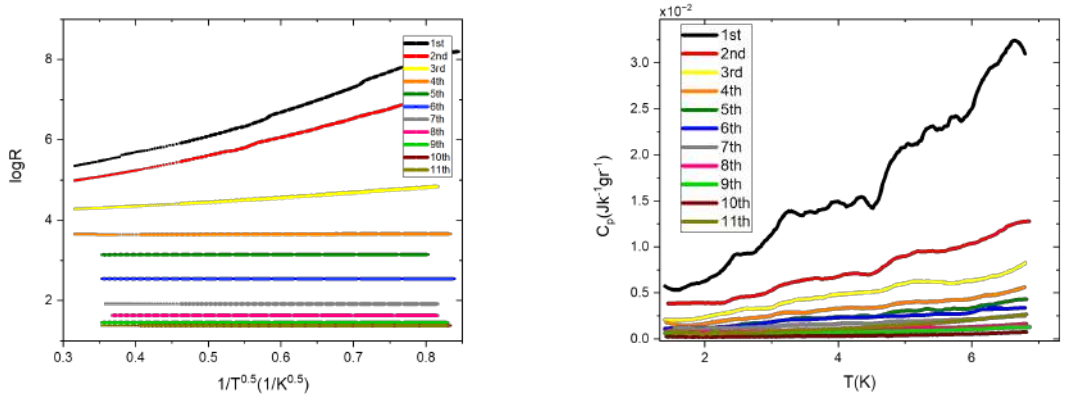

Figure A.2: Measurements of 11 sequential depositions of Ag thin layers (a) $logR$ vs $1/T^{0.5}$ plot illustrates the phase transition of the system. Initially, the system exhibits strong insulating behavior (black to yellow curves). Subsequently, it transitions to a normal metal with saturated resistance, beginning from the 4th deposition step. (b) C_p vs T measurements for the same Ag layers, using the same color code.

(a) (b)

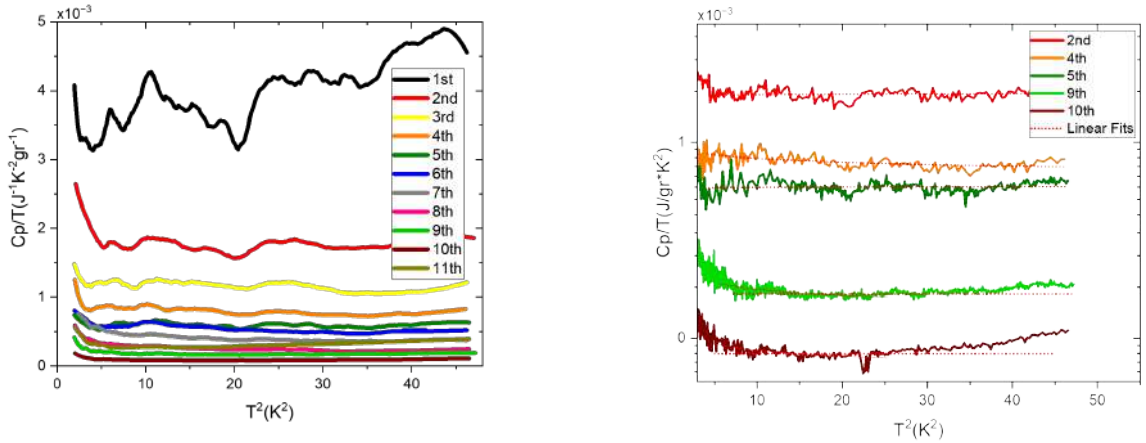

Figure A.3: The reduced C_p, $\dfrac{C_p}{T}$ vs T^2 of (a) the 11 Ag layers (b) chosen steps (log scale). In the final, thickest, films, higher slope is emerging from a certain T. The red dashed line is a linear fit for each curves.

fits (dashed red lines). The curves exhibit a nearly flat trend, with slopes hovering around 1, suggesting electronic heat transport dominance. Thinner films (layers 1-8) maintain this flat profile across the entire temperature range. However, as the layers thicken (layers 9-11), a discernible increase in slope is observed beyond a specific temperature threshold.

This rise in slope may be marking a transition from the electronic dominance observed in crystalline phases back to the phononic-dominated behavior seen for amorphous structures, signify a return of the system to an amorphous state as the layer become thicker. Interestingly, the

temperature at which the slope deviates from 1 decreases as the film thickness increases. While only three distinct slopes demonstrating this recovery were measured, further investigations on thicker layers may reveal a complete return to the initial slope of 3, resembling that observed in the amorphous phase of the film (see Fig. A.1). This slope behavior, initially indicating electronic dominance in C_p, appears to evolve as the layer thickens, possibly reflecting changes in the system's morphology.

The successful measurement of electronic behavior re-insure the decision to use silver with its high θ_D. Additionally, no second jump, excess entropy or reductions in β value were measured. As silver is a conventional metal this indicates that these unique behaviors are indeed linked to the QPT and the quantum fluctuations occurring in the vicinity of the transition.

The thickness and mass of each layer were calculated and are presented in Table.A.1.

Layer number	Mass (gr)	Thickness (nm)
1	5.983E-8	1.11256
2	1.55921E-7	2.8994
3	2.65609E-7	4.9391
4	3.90708E-7	7.26537
5	5.43909E-7	10.1142
6	7.82323E-7	14.54759
7	1.29269E-6	24.03808
8	2.25632E-6	41.95707
9	4.57972E-6	85.16156
10	9.16941E-6	170.50855
11	1.82391E-5	339.16284

Table A.1: Table of the mass and thickness at the varied steps.

Appendix B

Hysteresis

As we scanned the $R(V_g)$ of SC dots/SLG devices, the measurement revealed the existence of hysteresis in $R(V_g)$ when V_g was swept in the "up" versus "down" directions. As depicted in Fig. B.1, the hysteresis was affected by both temperature and magnetic fields. The hysteretic behavior is suppressed with increasing temperature (Fig.B.1(b,c)) and enhanced with increasing magnetic fields (Fig.B.1(d)).

The closure of the hysteresis at higher temperatures implies a relation to the existence of SC in the graphene. As superconductivity is destroyed, the hysteresis closes. However, the hysteresis widens (longer distance between the DP peaks) with higher magnetic fields, which requires further explanation.

It is worth noting that the observed hysteresis is more prominent in 2D devices based on CVD-grown SLG compared to devices based on exfoliated graphene. This difference may be attributed to the polycrystalline nature and higher impurity content of CVD-grown graphene. However, a full understanding of the appearance of hysteresis has not yet been achieved.

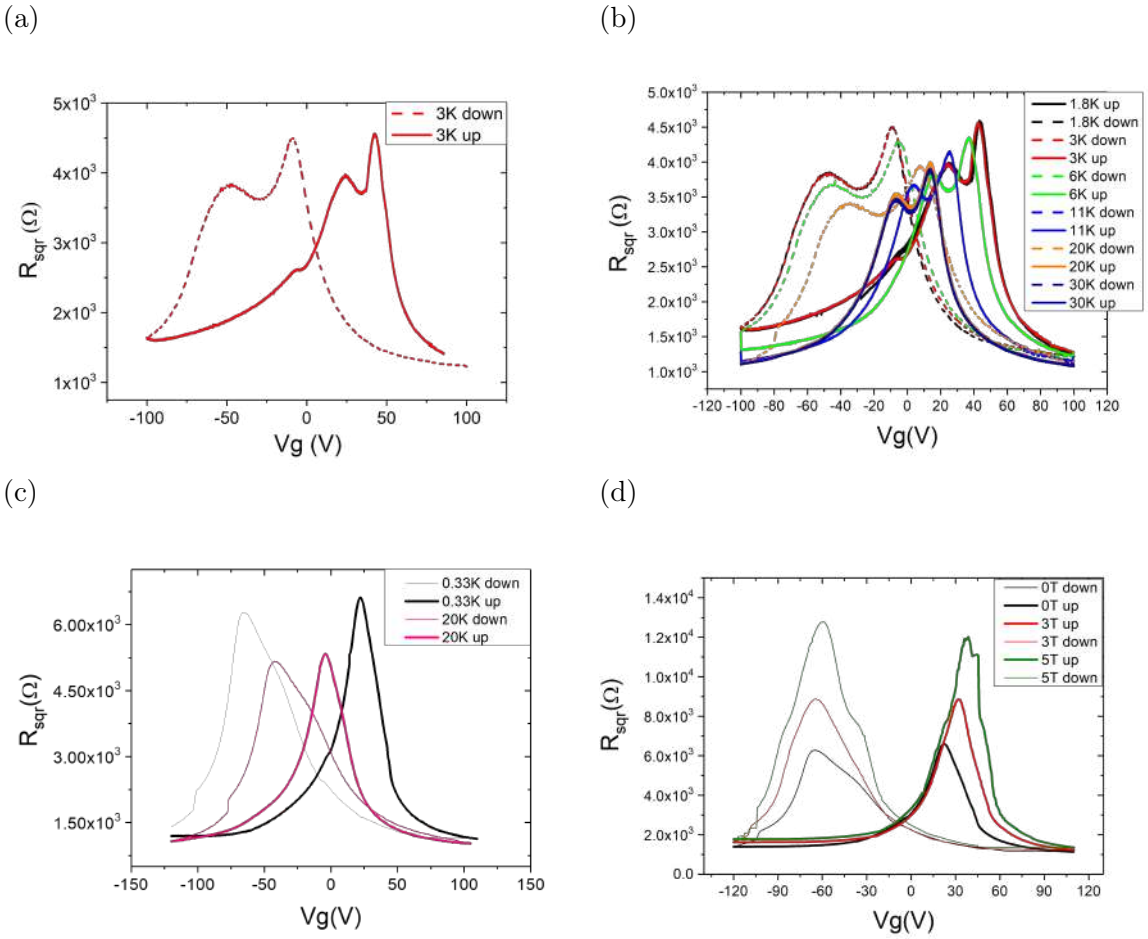

Figure B.1: Hysteresis in $R(V_g)$ of two InO dot array devices observed at different temperatures and under varying magnetic fields. (a) Set of $R_{sqr}(V_g)$ as swept in the "up" direction (solid line) and in the "down" direction (dashed line) at $B = 0T$ and $T = 3K$ (b) Several hysteresis sets of the same device at different temperatures (c) $R(V_g)$ of the second device as swept "up" (thicker line) and "down" (thinner line) at $B = 0T$, at $T = 0.33K$ (black) and $T = 20K$ (pink) (d) $R(V_g)$ sets of the same device under different magnetic fields. At higher temperatures, the hysteresis is closed, whereas under magnetic field it widens.

Appendix C

Higher temperatures and Magnetic field effects on $R(V_g)$ measurements

C.0.1 Effects on the SDP

The effects of temperature and magnetic field on the SDP are noteworthy. The SDP observed in the $R(V_g)$ sustains with temperature, as shown in Fig. B.1(b). It is observed even at temperatures much higher than T_C, such as $30K$, which is well above $T_c^{InO} = 3.5K$. The existence of SC at higher temperatures than T_c has been discussed previously [39] and is observed in our findings as well.

Next, we discuss the effect of applied magnetic field on the SDP. While the SDP was explicitly observed in some devices (usually in relatively 'big' matrices with numerous number of junctions, as in Fig. B.1(a)), in others, smaller matrices, we either couldn't reach it (due to too high $|V_g|$) or it appeared as a broad "knee" in the resistance measurement. In these cases, this "knee" appeared to evolve into a peak or split into a pronounced peak under a magnetic field. This behavior is evident in Fig. B.1(d) and in a few additional examples, where applying magnetic field resulted in the transformation of this "knee" into a more pronounced and well-defined peak, as shown in Fig. C.1.

Taking the device depicted in Fig. B.1(a,b) as an example to demonstrate the effect of the magnetic field, in addition to the distinct "triangular shape" of the $R(V_g)$ curve, at $B = 0$, there is no appearance of a second DP in the $R(V_g)$ curve. Instead, a distinct "knee" is observed around $V_g = -30V$ (Fig.B.1(a)). As the magnetic field increased, this knee evolved into a prominent peak (Fig.B.1(b)). Furthermore, as discussed in the main body of the thesis (Sec.4.2.1), resistance fluctuations are observed and seem to be most prominent near the DP. In cases where the $R(V_g)$ curve appears smooth, fluctuations are only seen in the DP regime. These fluctuations become more pronounced as the magnetic field increases.

Certainly, this development/"splitting" of the knee under magnetic field can be related to the quantum Hall effect (QHE) in graphene.

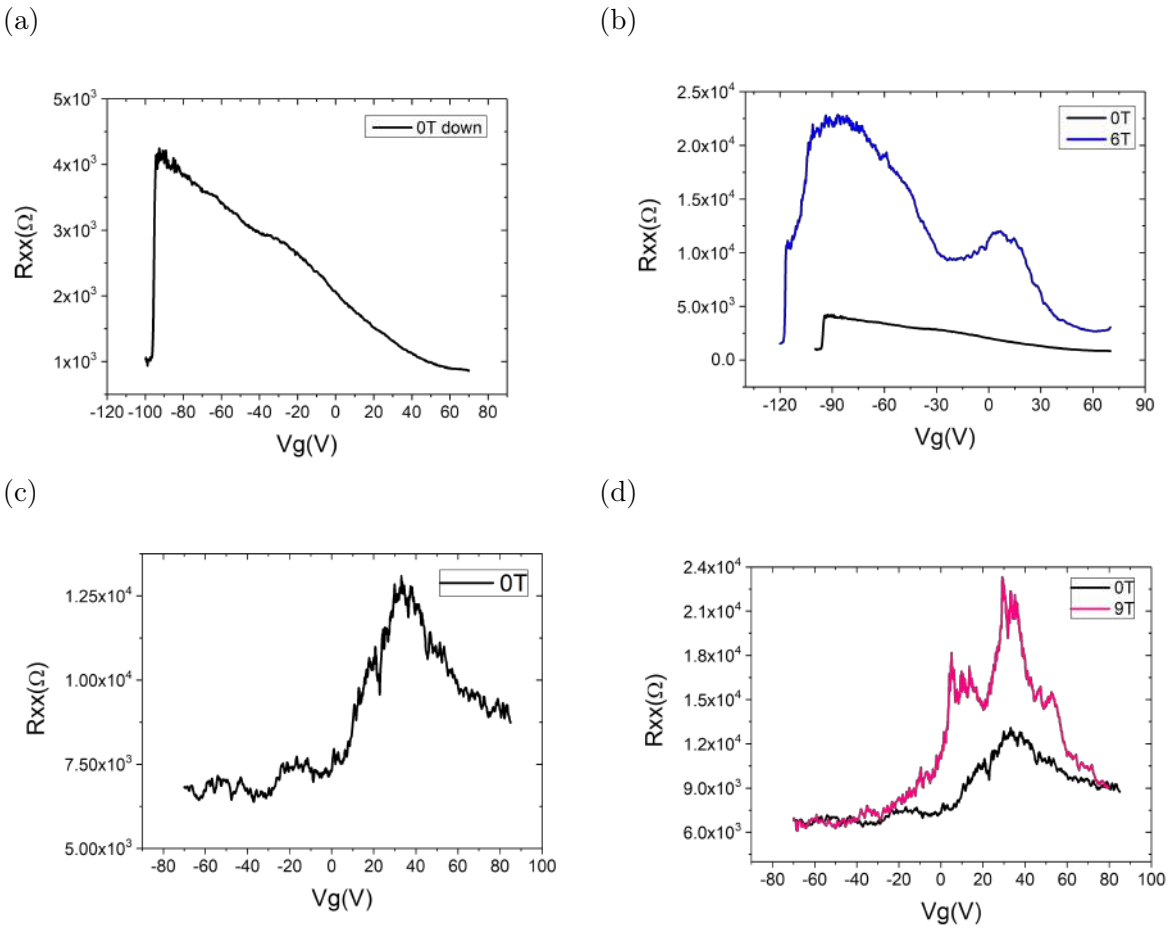

Figure C.1: Different devices exhibiting a "knee" at $R(V_g)$ under $B = 0T$ that evolves under applied magnetic field.

C.0.2 QHE and filling factors

The QHE in graphene is characterized by the observation of discrete steps in conductivity when a magnetic field is applied. These steps correspond to changes in the number of occupied Landau levels, which are filled according to the filling factor (ν). ν represents the ratio of the number of electrons to the number of magnetic flux quanta passing through the graphene sheet. The QHE has been clearly observed mainly in devices made of exfoliated flakes. By varying the electron density, V_g, the number of occupied Landau levels changes, leading to alterations in conductivity.

In Fig. C.2, $R(V_g)$ curves showing a knee at $B = 0T$ and its evolution under different magnetic fields, of two distinct exfoliated-flake devices, are presented. The dot matrices in both presented devices were fabricated at an O_2 pressure of 8×10^{-6}, resulting in SC dots. In these devices, the QHE was nicely measured, manifesting in fine features in the $R(V_g)$.

These changes in conductivity are directly related to the filling factors. The relation between resistance and filling factor, of the same device presented in Fig. C.2(b), is shown in Fig. C.3.

The observation of the QHE can attest to the cleanliness and quality of the device.

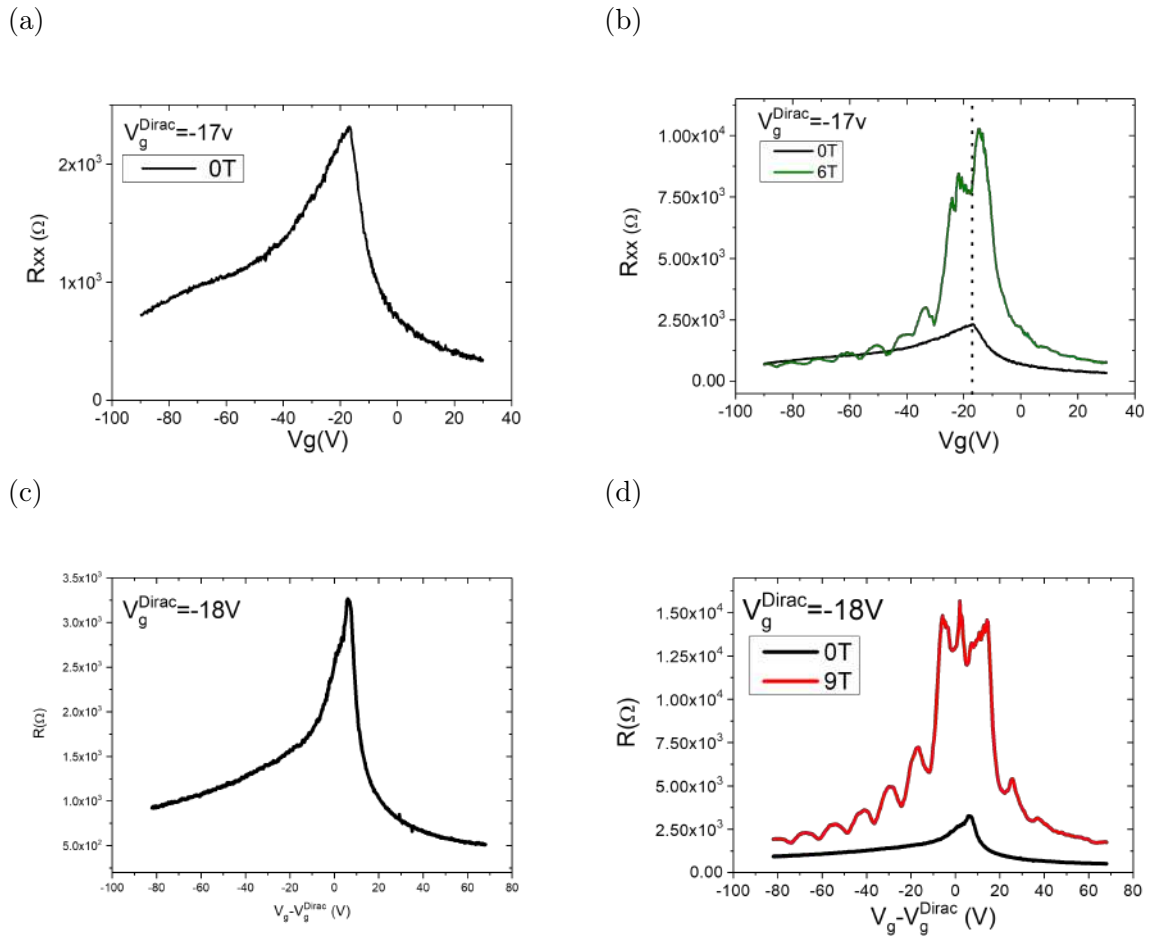

Figure C.2: $R(V_g)$ of a 2D dots matrix fabricated on top of exfoliated graphene, measured under different magnetic fields. In both devices, at $B = 0T$ (a,c), a single peak, the DP, was observed with a knee to its left side. As B was applied, the QHE was observed. (b) Device measured at $B = 0T, 6T$ at base temperature of $0.33K$ and (d) measurements of a different device under $B = 0T, 9T$ at $1.66K$

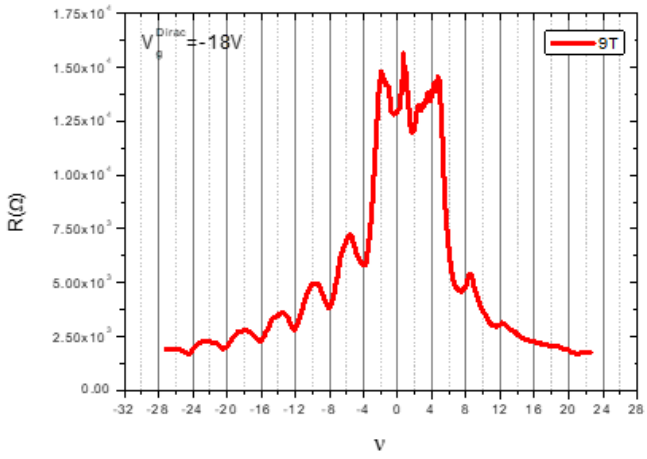

Figure C.3: $R(\nu)$, at $B = 9T$ of a 2D dots matrix exfoliated-graphene based device. The steps in resistance match the filling factor integers $0, -4, -8, -12, -16$..

Appendix D

Extended SVD analysis

In this chapter, we provide further SVD analysis of 1D and 2D SLG/SC dot devices, further confirming the consistency of the results. This includes a 1D device of **Tin** (Sn) dots, which was not previously discussed in the main body of the thesis. These additional results reinforce key findings and demonstrate the robustness of the SVD approach. While the main body of the thesis focuses on data at zero magnetic field, this appendix includes measurements and SVD analysis under a 6T magnetic field.

Figure D.1 shows dI/dV measurements at base temperature and at $B = 0$ for two additional **1D** samples: (a) a **Tin** (Sn) device and (b) an InO device. Both show fast oscillations in dI/dV as a function of V_g and V_{dc}. In contrast, (c) presents the dI/dV measurements of a 2D InO dot matrix device, where slower, larger periodic oscillations are observed.

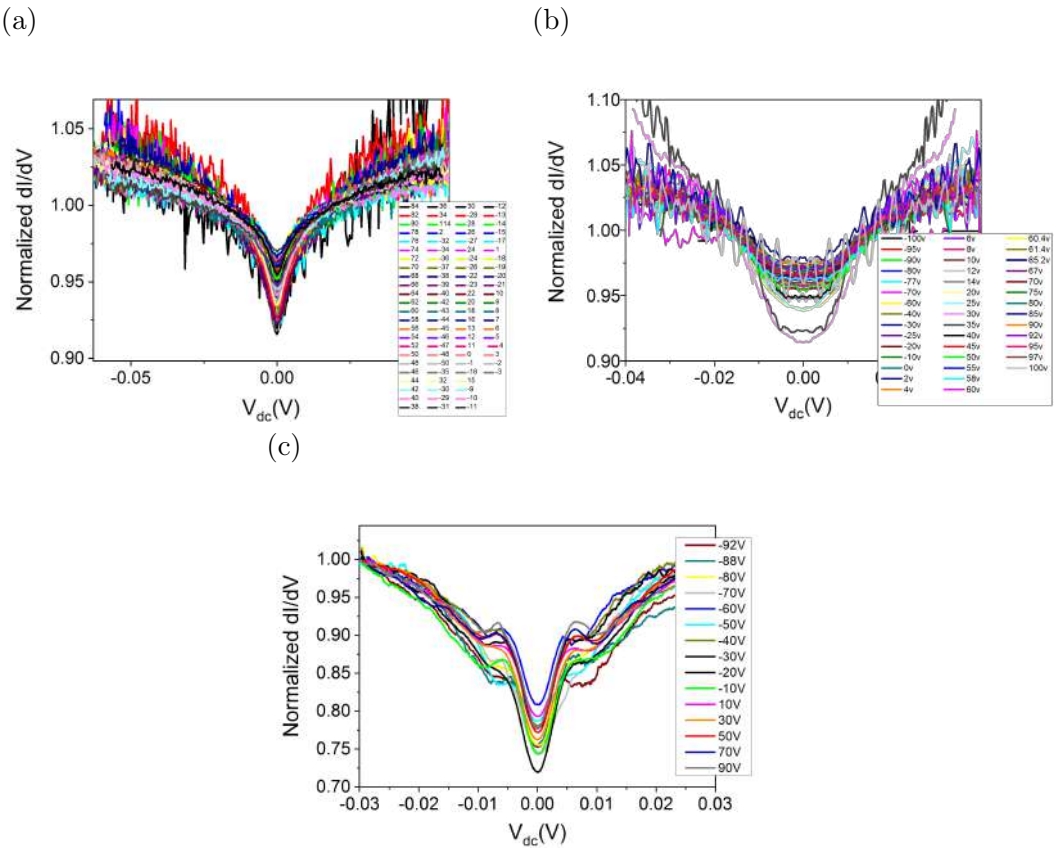

Figure D.1: dI/dV measurements of SLG/dots devices. (a-b) two 1D devices, consists of 17 dots row of (a) Sn and (b) InO. (c) 2D InO dots device. Clear oscillation pattern is seen at the different devices, with faster oscillations at the 1D devices compare to the oscillations in the 2D device.

SVD analysis was performed, and the findings are as follows:

The λ values for the 1D Sn device and 2D InO device are shown in Fig. D.2(a) and (b), respectively. The power-law exponent k for the 1D Sn device is -1.2, closely matching the -1.3 found for the 1D InO device, as discussed in the main body of the thesis. The 2D device has a power-law exponent of -4, consistent with the value obtained for the 2D device analyzed in the main body of the thesis. This agreement suggests that the scaling behavior remains consistent across different device geometries, regardless of material. The similar λ values suggest comparable noise characteristics between different materials, influenced by geometry. Notably, the data from the 1D system shows noisier (more oscillatory) behavior, aligning with the understanding that as the number of trajectories increases, faster oscillations are averaged out, as discussed in the main body of the thesis.

.

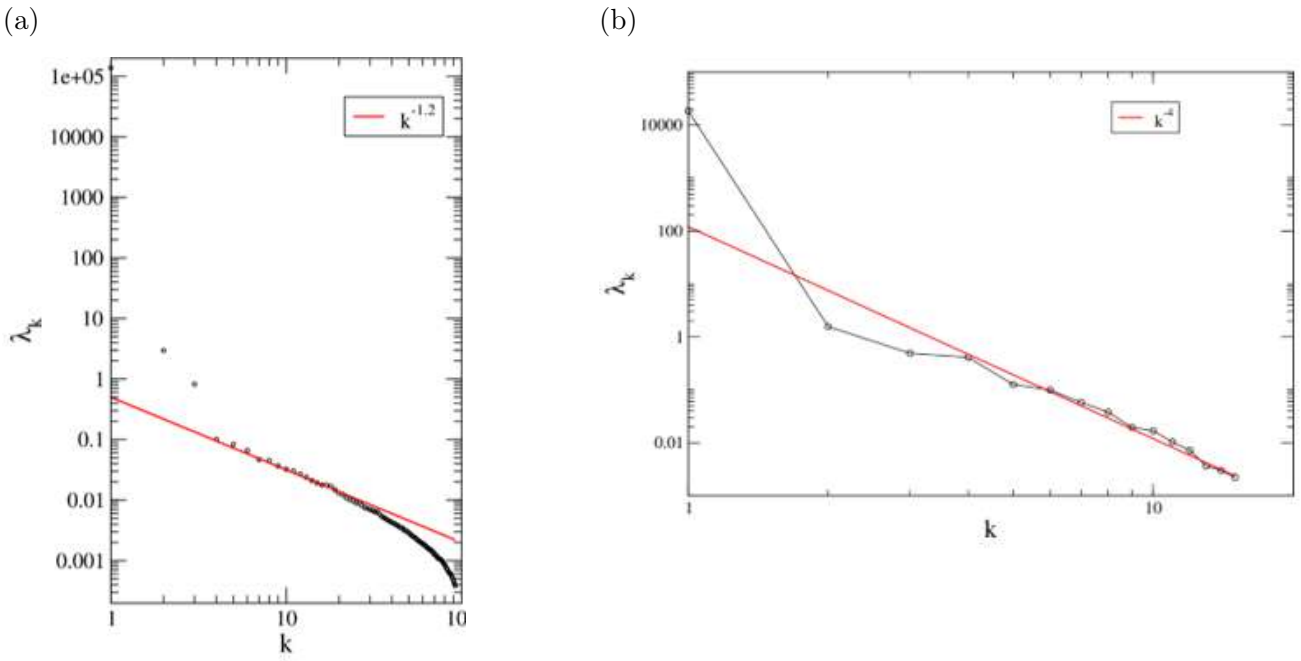

Figure D.2: λ values of 1D Sn device, exhibiting $k = -1.2$ power low behavior, and of 2D InO device with $k = -4$ power-low behavior.

Next, we turn to examine the first two SVD modes, presented in Fig. D.3 for the 1D Sn device, Fig. D.4 for the 1D InO device, and Fig. D.5 for the additional 2D InO device.

The **first mode** captures the logarithmic characteristics of the AA background. For the 1D devices, this logarithmic AA background can be seen in Fig. D.3(a) and Fig. D.4(a). In the 2D device (Fig. D.5(a)), fine features are observed. These results are consistent with those in the main body of the thesis.

The **second mode** reveals a crossing between two points, from which Δ can be inferred for the 1D devices (known current trajectory). For the Sn device, we calculate Δ_{Sn} by dividing the regime between the two crossing points at Fig. D.3(b) by the 17 junctions. We find $\Delta_{Sn} \approx 1.08mV$, which is remarkably close to the real Δ_{Sn} value measured, of $\approx 1meV$ [78]. Similarly, $\Delta_{InO} \approx 0.71mV$ is extracted from Fig. D.4(b), consistent with the known Δ_{InO} value of our InO samples. It can be easily observed with the naked eye that $\Delta_{Sn} > \Delta_{InO}$ when comparing the second mode SVD analysis figures of the two devices, which is an interesting point to note.

Additionally, the *amplitudes* of the second mode vary around the DP, as seen in Figs.D.3 and D.4 panels (c). A minimum, where the second mode is smaller than 1 (local minima in the Sn case and absolute in the InO case), appears in a specific V_g regime, in the vicinity of the DP. This change in the extremum "type" of the 2nd mode amplitude is evident and consistent across our measurements, as demonstrated in the main body of the thesis. For the 2D device presented here, the DP is at too high V_g for us to cross during measurement. Consequently, this effect is less clear in this case, and the corresponding figure for the 2D device is not included.

Higher modes exhibit oscillatory behavior. Overall, this extended SVD analysis confirms the findings from the main body of the thesis, showing consistent behavior across different devices and materials. It underscores the power of SVD analysis in extracting important physical

information that would otherwise be difficult to detect.

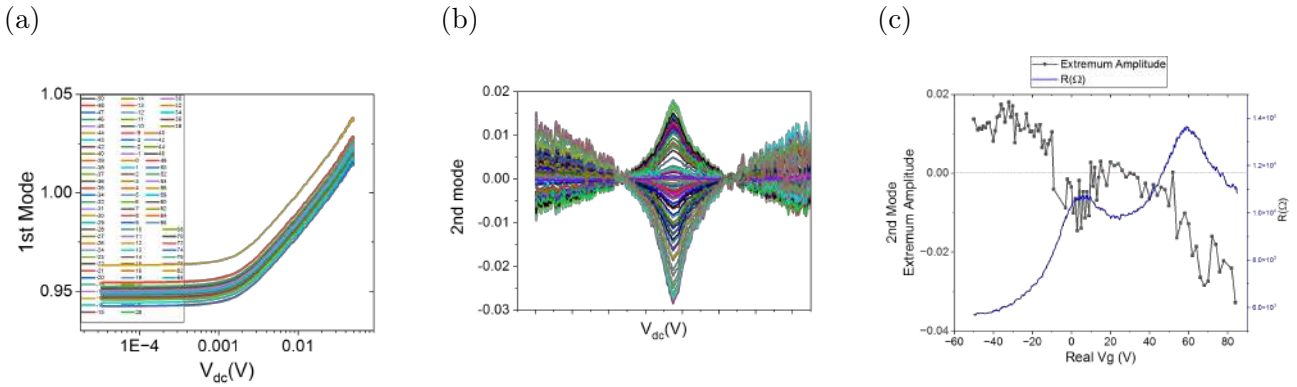

Figure D.3: SVD analysis of Sn 1D device.

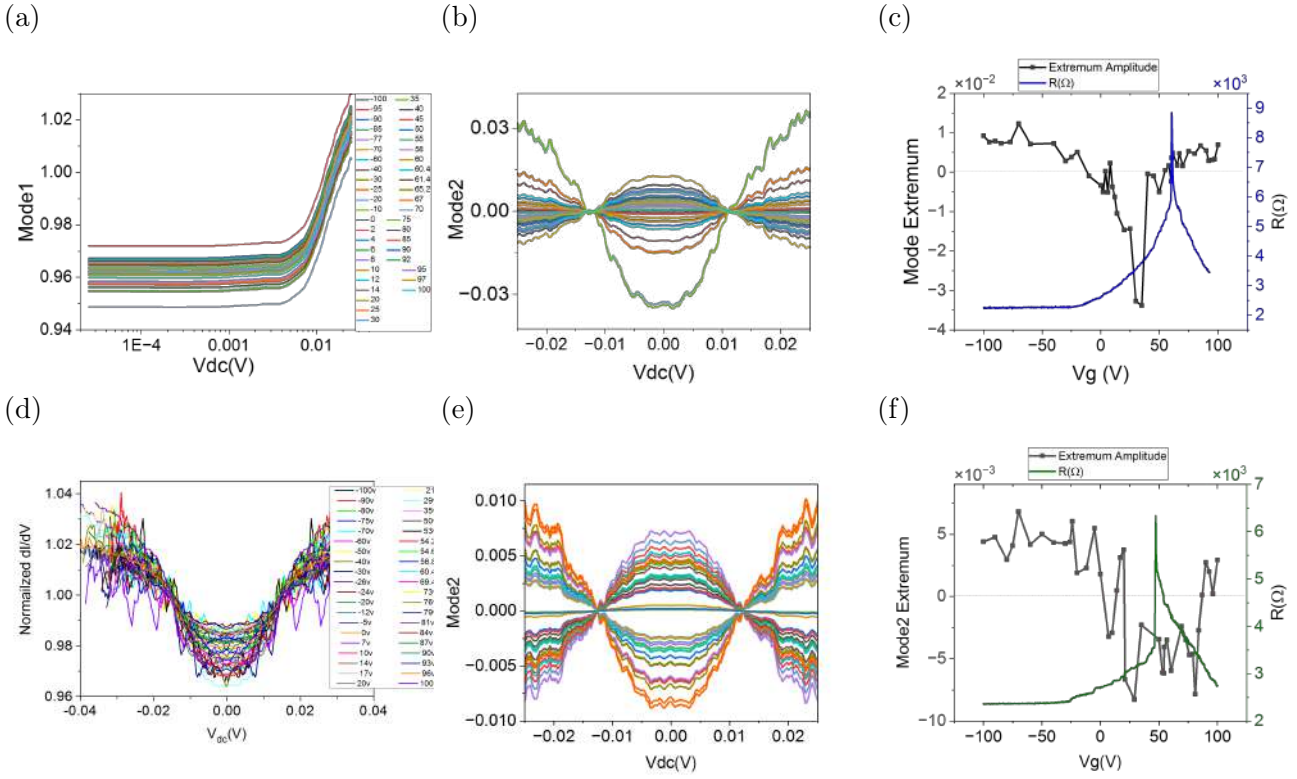

Figure D.4: .

SVD analysis of InO 1D device data. **Top Row (0T)**: (a) First SVD mode, (b) 2nd SVD mode, (c) amplitude of the 2nd mode (black dotted line) with the device resistance (blue curve) vs. V_g. This SVD analysis is consistent with the 1D device discussed in the main body of the thesis. **Bottom Row (6T):** (d) Raw dI/dV data of the device at $6T$, (e) 2nd SVD mode and (f) same as (c), just under field.

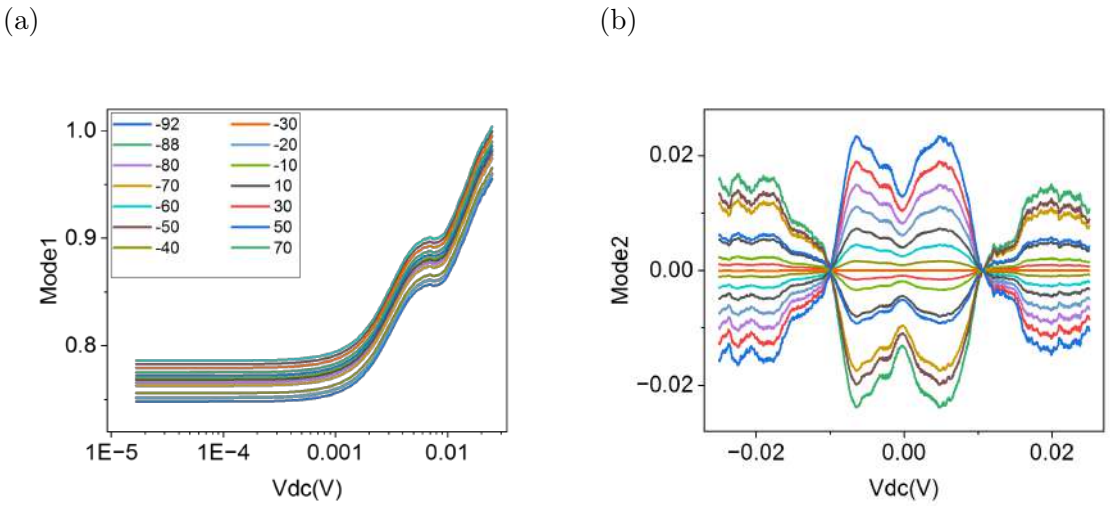

Figure D.5: SVD analysis of InO 2D device. Its analysis shows similarity to the 2D device discussed at the main body of the thesis.

Now, we turn to examine the SVD analysis of the results under magnetic field.
For the additional 1D InO device (raw data in Fig. D.1(b)), the results at 6T are shown in Fig. D.4(d-f). In Fig. D.4(d), the raw dI/dV data is presented. The $6T$ data exhibits larger fluctuation amplitudes compared to the 0T data (see raw data without magnetic field in Fig. D.1(b)). However, qualitatively, it remains similar— showing a dip at all V_g values, with fast fluctuations superimposed on an overall structure.

A difference, visible in the U vectors from the SVD analysis, is that under a 6T field, the AA background broadens and its absolute value decreases. The U values for the first and second modes at 0T (black curve) and 6T (red curve) are shown in Fig. D.6. Here, we observe the broadening of the AA background ($U1$) and a slight broadening of $U2$, both with lower absolute values compared to 0T. This broadening and reduction in the AA background under a magnetic field is consistent across other devices as well.

The SVD analysis at 6T (Fig. D.4(c-f)) yields results that are qualitatively similar to those at 0T; The 2nd mode at 0T and 6T (Figs. D.4(b,e)) shows overall similarities. However, the second mode at 6T is more fluctuating, effectively capturing the nature of the raw data. When extracting Δ from the 2nd mode analysis at 6T, we find that it remains the same as at 0T. This suggests that Δ does not change between 0T and 6T.

Figures D.4(d,f) further illustrate the same behavior. We observes a broadening of the DP regime in the $R(V_g)$ measurements under 6T, and correspondingly, a broadening of the region where a minimum occurs in the second mode amplitude analysis. Despite these changes, the overall behavior remains consistent.

(a) (b)

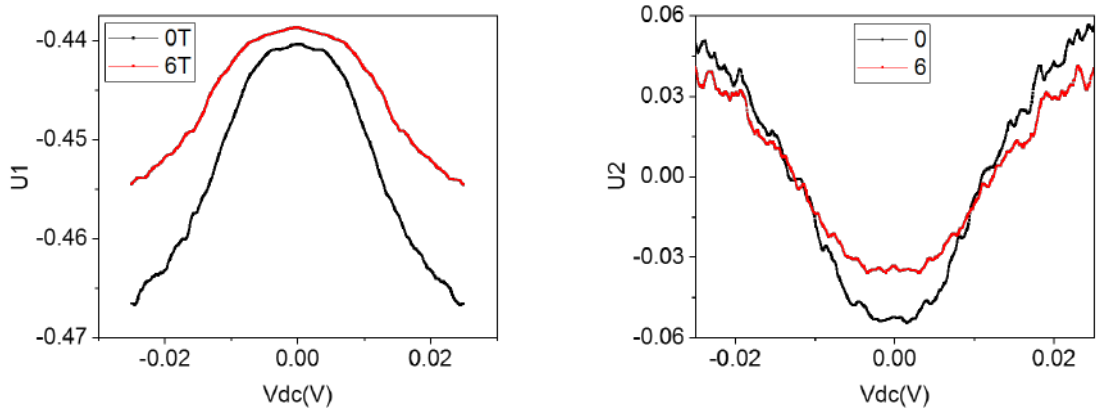

Figure D.6: SVD $U1$ (a) and $U2$ (b) vectors of the 1D InO device at 0T (black) and under 6T (red). Showing a broadening under field and smaller absolute values.

תקציר

מעבר הפאזה בין מוליך-על-למבודד (SIT), בו מערכות עוברות מפאזה בו הן מוליכות-על לפאזה בו הן מבודדות, בעקבות שינוי פרמטרים שונים שאינם הטמפרטורה, הוא תופעה קוונטית מרכזית בפיזיקה של חומר מעובה. בלב מעבר פאזה קוונטי זה נמצאות אוסילציות קוונטיות, המעניקות הצצה לאזור קוונטי קריטי שבו המערכת במצב ייחודי – מחד היא לא במצב של מוליכות-על מלאה אך מנגד היא גם לא במצב בו היא מבודדת במלואה. למרות מחקרים מקיפים שנערכו, היבטים יסודיים כגון הופעתן וטבען של פאזות בוזוניות אקזוטיות במהלך הSIT, נותרו נושא לדיון ער שבתוכו מגוון שאלות פתוחות אותן מחקר זה מבקש להאיר באור חדש.

מטרת מחקר זה היא העמקת ההבנה של המנגנונים העומדים בבסיס הפאזות הבוזוניות במערכות מוליכי-על גרנולריים לא מסודרים. זאת, באמצעות שתי שיטות חדשניות: (1) מדידות תרמודינמיות, תוך שימוש בטכניקת מדידה רגישה במיוחד לחקר קיבול החום הסגולי של שכבות דקות של אינדיום (In). מדידה זו נעשית תוך כדי שהשכבות עוברות את הSIT, מתוך מטרה לחקור את ההיתכנות של פאזה מתכתית בוזונית (BM). חלק זה של המחקר נעשה בשיתוף פעולה עם מעבדתו של ד"ר אוליבייה בורז'ואה ממכון המחקר Neel, CNRS שבגרנובל, צרפת, ובשימוש בחדרים הנקיים ובמכשירי המדידה במכון המחקר. (2) מדידות תובלה, הבוחנות את יחידות הבסיס של פאזות אלו - צמתי מוליך-על-מתכת (NS)- במטריצות נקודות על-מוליכות של אינדיום-אוקסיד אמורפי (InO) על גבי גרפן (SLG). במחקר זה נבחנו הן דגמי שורה בודדת של נקודות (1D) והן מערכי מטריצות של נקודות (2D) על מנת לנתח את תכונותיהן החשמליות באמצעות מדידות התנגדות והולכה דיפרנציאלית. כל פרק בעבודת המחקר מאורגן סביב שתי השיטות הללו.

ממצאי המחקר כוללים חתימות תרמודינמיות חדשות בקיבול החום הסגולי של שכבות In בעוביי הביניים, כאשר מדידות ההתנגדות כתלות בטמפרטורה הציגו התנהגות BM, המשתקפת בהתנגדות רוויה בטמפרטורות נמוכות. בשכבות ביניים אלו, במדידות קיבול החום הסגולי נצפתה סטייה מהתנהגות מוכרת: המדידה הראתה עלייה משנית חדה, שנשארת יחסית שטוחה וקבועה בטמפרטורות גבוהות יותר, במקום לחזור לאות המצב הנורמלי. זוהי הפעם הראשונה שתכונה כזו נמדדה בקיבול חום סגולי של שכבות מוליכות-על. כתוצאה מעלייה חדה זו נגזרו אנומליות באנטרופיה בשלבי ביניים אלו. בנוסף, הסטייה התבטאה בשינוי בנושאי החום הדומיננטיים, המצביע על מאפיין ייחודי השייך לשכבות הביניים הללו.

מדידות התובלה סיפקו אינפורמציה חדשה על התנהגות צמתי NS, עם דפוסי אוסילציות ייחודיים שנמדדו הן במדידות ההתנגדות כתלות במיתוח הגרפן, והן במדידות ההולכה כאשר המתח הישיר שונה, במיתוחי גרפן שונים. אוסילציות אלו

בהולכה הופיעו בתוך ומחוץ לאנרגיית הפער האסור (דלתא) של מוליך-העל, כאשר האוסילציות המהירות ביותר נצפו בדגמי ה1D. עיקר מאמצי הניתוח שלנו התמקדו בדפוסי אוסילציות הולכה אלו, תוך שימוש, לראשונה, בטכניקת SVD לניתוח נתונים ניסיוניים מורכבים. טבען של אוסילציות אלו עדיין לא מובן במלואו ,וייתכן שהן תוצאה של פאזת הBM בה נמדדו.

למרות שעדיין אין הסבר מלא לתופעות, תצפיות ניסוי חדשות אלו מאירות באור חדש את הדינמיקה המורכבת שמניעה את הSIT ואת המורכבויות של הפאזות הבוזוניות. תוצאות המחקר שלנו סוללות את הדרך לשאלות מחקר עתידיות ולהתקדמות בפיזיקה של חומר מעובה, ומקרבות אותנו להבנה מקיפה יותר של הפאזות הקוונטיות המרתקות הללו.

תוכן עניינים

עבודת מחקר זו נעשתה בהנחייתו של פרופ׳ אביעד פרידמן מהמחלקה לפיזיקה,
אוניברסיטת בר-אילן.

פאזות בוזוניות במעבר על מוליך מבודד במערכות גרנולריות

חיבור לשם קבלת התואר "דוקטור לפילוסופיה"

מאת:

יהודית פראדיל שטיין

המחלקה לפיזיקה

הוגש לסנט של אוניברסיטת בר אילן

רמת גן תשרי, התשפ"ד